The Effect of Pressure, Bending and Annealing Temperature on the Mechanical and Optoelectronic Properties of Perovskite Solar Cells

Abstract

The increasing needs for clean and sustainable energy stimulate the growing interest in photovoltaic (PV) technology using organic-inorganic hybrid perovskite materials. However, perovskite solar cells (PSCs) are faced with stability problem due to the presence of cracks or defects within the perovskite absorber and along the interfaces of the multilayered PSC structures. It is therefore important to improve on our understanding of their degradation pathways and mechanical stabilities. In this thesis, the effects of pressure, bending and processing annealing temperature on the mechanical and optoelectronic properties of perovskite solar cells are studied.

First, the effects of pressure on photoconversion efficiencies of perovskite solar cells (PSCs) are studied using a combined experimental and analytical/computational technique. The results show that crystallization, absorbance, and the power conversion efficiencies of PSCs can be significantly improved by the application of pressure. This leads to the closing-up of voids and the corresponding increase in the interfacial surface contact lengths, which increase with increasing pressure. The observed improvement in the power conversion efficiencies (9.84 to 13.67%) was observed with increased pressure between 0 and 7 MPa, attributed largely to the effects of increased surface contact and the compaction and infiltration of the TiO_2 layers with perovskite during the application of pressure. At higher pressure values (> 7 Mpa), the damage due to sink of the perovskite layers into the mesoporous layers results in reductions in the photoconversion efficiencies of PSCs.

The understanding of the variations in the mechanical properties of organic-inorganic hybrid perovskites structures that are processed at different annealing conditions is then studied for ultimate device performance and robustness. We show that the temperature at which perovskite film is annealed affects the mechanical properties of the devices fabricated. The size dependence

of hardness is due to the increase in the density of geometrically necessary dislocations (GNDs) with decreasing indentation size. The indentation size effects are characterized between the micron- and nanoscales by a bi-linear strain gradient plasticity (SGP) framework with source-limited and established dislocation substructures. The measured microstructural length scales decrease with increasing annealing temperature to 130^{O}C, after which it began to increase, causing films annealed beyond 130^{O}C to have reduced strengths because the larger microstructural length scales correspond to larger dislocation spacings and weaker dislocation interactions. Perovskite solar devices annealed at temperatures above 130^{O}C have poor performance. The results show that perovskite solar cell devices annealed at 130^{O}C exhibit optimal performance and attractive combinations of mechanical properties.

Finally, the underlying failure mechanisms associated with flexible perovskite solar cells (FPSCs) are elucidated for deformation and cracking under monotonic and cyclic bending. The mechanical robustness of the inverted flexible PSCs is increased with increasing fraction of polyethylene oxide (PEO) in the double-cation perovskite precursor, which promotes the grain size and passivates the defects of the film. The associated changes in the optical transmittance of the perovskite-PEO absorber and the PCEs of the multilayered FPSCs structures are elucidated under monotonic and cyclic bending. The failure mechanisms of the perovskite films for different radii of bending were observed using a scanning electron microscope before computing the interfacial fracture energies in the multilayer devices using finite element simulations. The failure mechanisms are then used to explain the degradation of the optoelectronic properties of flexible perovskite solar cells.

Keywords: Pressure Effects, Annealing Temperature, Bending, Mechanical Properties, Perovskite Solar Cells and Optoelectronic properties.

Table of Contents

List of Tables

List of Figures

Chapter 1
BACKGROUND AND INTRODUCTION

1.0. Background and Introduction

1.1. Background

Energy supply and demand determine the course of global development in all areas of human endeavors. Sufficient clean-energy supplies relate to global stability, economic prosperity, and quality of life. One of our most important challenges for the next half-century is the quest for energy sources to meet the growing global demand. Now, the world uses energy at a rate of about 4.1 x 10^{20} joules/year, equivalent to 13 terawatts (TW) of power consumed continuously (US Department of Energy, 2012). Even with aggressive conservation and energy efficiency measures, the world's population estimate to rise to 9 billion by 2050, and together with rapid technological development and worldwide economic growth, the energy demand estimates to be more than double (to 30TW) by 2050 and more than triple (to 46 TW) by the end of the century ((DOE), n.d.). Reserves of fossil fuels that currently power society will not meet that demand for longer-term purposes as continued use has adverse side effects, including pollution threatening human health and climate change-related greenhouse gases. Therefore, sustainable, and environmentally friendly energy sources are needed. Renewable energy sources can be the solution (Institute for Energy Economics and Financial Economics, 2019), although the cost of exploiting the energy from these sources is still a little too high.

Renewable energy is energy from a naturally regenerating source such as wind, sunlight, tides, waves, geothermal, (Ellabban et al., 2014) etc. The capacity for different types of renewable energy sources has increased rapidly over the years. Although wind and hydro energy resources have

dominated during the early years, other renewable energy sources, in particular Solar PV, are growing rapidly in terms of capacity. Solar energy comes as electromagnetic rays from the sun to the earth. Solar energy is one of the leading renewable power sources and has already shown considerable potential for a prime energy source in the future. The potential power extractable from solar energy is approximately 2300 TW/year, which means an efficient solar energy extraction is sufficient to fulfill every human energy requirement. However, there is a reluctance to utilize solar photovoltaics (PV) as a primary energy source because its unit cost is high compared to other renewable energy. The main reason behind the high costs of Solar PV is low extraction and power conversion efficiency. The amount of power extracted from a solar panel for a given solar intensity depends on the power conversion efficiency and the area of the panel. The efficiencies in the conversion of solar panels are still not very high, comparatively costly. Cloudy days and smaller daytime can reduce the power extracted from a given panel. However, for Solar PV, it is a good indication that unit cost has decreased over the years exponentially (IEEFA, 2010). A decline of 74% in total installed costs was observed between 2010 and 2018 (Figure 1.1). Lower solar PV module prices and ongoing reductions in balance -of-system costs remain the main drivers of reductions in the cost of electricity from PV. Solar PV installation costs would decline dramatically from now to 2050 globally, the total installation cost of solar PV projects would continue to decline dramatically in the next three decades, averaging in the range of USD 340 to USD 834/kW by 2030 and 165 to 481/kW by 2050, compared to the average of USD 1210/kW in 2018 (IRENA (2019) & aspects (A Global Energy Transformation: paper), 2019).

Edmund Becquerel was the first to convert light into electricity in 1839 (Szabó, 2017). Photovoltaics (PV) started when a crystalline silicon-based solar cell with a power conversion efficiency (PCE) of 4.5 % originated in Bell lab, USA (Chapin et al., 1954). Since then, researchers

have been exploring a low-cost device structure and new materials that display the PV effect. Second-generation solar cells based on III-V device structure, GaAs, CdTe, InP, and CIGs solar cells were introduced in the field of solar photovoltaics. The Dye-sensitized solar cells, the third generation came about in the early 1990s, and in the 2000s, organic photovoltaic cells were

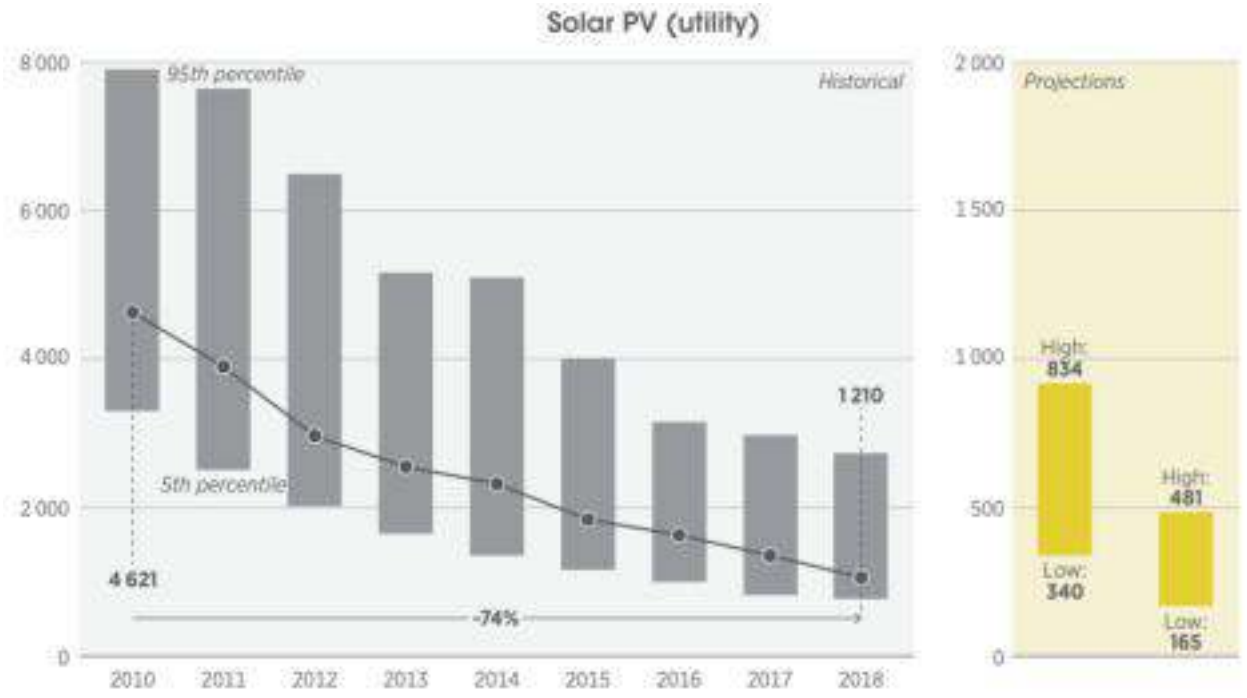

Figure 1.1. Projected rapid decline in total installed cost of solar PV from now to 2050

introduced. With increasing interest in the development of nanomaterials, research efforts are towards developing solar materials that are inexpensive and processed at a low cost. Currently, crystalline silicon solar cells dominate the market, but considerations such as the need for an expensive production method and expensive raw materials are pushing researchers to develop a new PV technology that combines high efficiency with cheap manufacturing costs. Perovskite materials because of their excellent photovoltaic performance, low-cost raw material, and demand for simple manufacturing conditions are gaining huge research interest (Zhou et al., 2018). Perovskite solar cells (PSCs) do not require any complicated processing conditions; instead, they

may be made in laboratories utilizing wet chemistry and low-cost processes like spin coating, dip coating, screen printing, and dual source evaporation, among others. A flexible substrate can also be used to grow perovskite materials. The rapid increase in power conversion efficiency (PCE) from 3% to 25.2% (28% in tandem architecture) in the last ten years (*Best Research-Cell Efficiency Chart | Enhanced Reader*, n.d.; Kojima et al., 2009) demonstrates PSCs' enormous capability, whereas other technologies took nearly 30 years to reach this milestone. Perovskite can be used as both an absorber and a charge transport layer in a solar cell (Mei et al., 2014).

Perovskite materials are promising materials for future generation PV technology because of their distinctive properties, such as high electron mobility (800 cm^2/Vs) (Valverde-Chávez et al., 2015), high carrier diffusion length (exceeding 1 μm) (Miyata et al., 2015), ambipolar charge transport behavior (*Interview with Greatcell Solar Materials' GM Yanek Hebting*, 2019), high absorption coefficient (greater than 10^5 cm^{-1}) due to *s-p* antibonding coupling, Wannier type exciton, low exciton binding energy (less than 10 meV) (Miyata et al., 2015), high photoluminescence (PL) quantum efficiency (as high as 70%), high carrier lifetime (exceeding 300 ns), optimum band gap, low surface recombination velocity, tunable bandgap, great structural defect tolerance, and genial grain boundary effect. Despite its many advantages, PSCs' commercialization is hampered by poor device stability and a short lifetime.

Crystal growth control, halide mixing, hetero-elemental combination (Mali et al., 2015), and other methods have been utilized to optimize their chemical compositions and increase crystallinity. In addition, numerous processing procedures have been devised to increase their characteristics and device performance, such as one-step and sequential solution deposition (Jeng et al., 2013), vapor-assisted solution processing (Q. Chen et al., 2014), and solvent engineering (Jeon et al., 2014). Although these chemical and processing methods have shown tremendous promise in improving

the performance of this class of functional materials, some difficulties remain, and novel materials design/optimization approaches are urgently needed. Fabrication temperature has proven to be crucial in modifying the structures and properties of these perovskites (Zheng et al., 2015). Pressure, like temperature, is a state parameter that gives an additional dimension for efficiently tuning material properties by altering interatomic distances (Zhang et al., 2020).

Thin-film PV technologies were developed for applications requiring low weight and low cost. In recent years, the growing interest in flexible and wearable electronics has sparked a surge in research into flexible and stretchable solar cells. Integrating these flexible solar cells onto portable products, walls, and windows would revolutionize existing energy production, reduce pollution, and vastly expand energy harvesting situations. Advancing flexible solar cells into stretchable ones will further deepen the compatibility with presently promising portable and wearable electronics.

A Wearable and deformable PV absorber should generate a high PCE and possess excellent tolerance over bending and stretching. Perovskite has these outstanding properties, which makes it suitable for flexible and stretchable solar cells. The application and lifetime of flexible power sources strongly depend on their mechanical deformation tolerance and the electrical property retention under deformation (Mao et al., 2017). Flexible power sources should withstand high strain caused by external mechanical deformation like bending, compressing, stretching, folding, and twisting while retaining their electrochemical performance stability and structural integrity. Hence, the mechanical reliability assessment and electrical property analysis of flexible devices need attention for future applications. The main mechanical deformation characteristic of flexible solar devices is their tolerance in bending into a specific curvature. Thus far, to evaluate the quality and failure modes of flexible devices, bending characterization criteria and mechanical methods have been developed to determine the quality and failure mechanisms of the devices. Detailed

analysis on bending mechanics combining experimental and theoretical results provide not only reliable test methods to describe the bending state but also guidance for configuration design of devices against mechanical failure.

Perovskite solar cells' performance has been improved using a variety of approaches (Cho et al., 2017; Zhao et al., 2016). These include processing conditions (Y. H. Kim et al., 2015), modification, and optimization of layered structures (Tan et al., 2014). Pressure has improved the performance of organic electronic devices (solar cells and light-emitting devices) in previous research (Asare et al., 2016; Du et al., 2014). The application of pressure on perovskite layers (both hydrostatic and non-hydrostatic) affects their molecular packing and structure (Capitani et al., 2016; Oyelade et al., n.d.). Increased pressure on perovskite materials induces crystallization due to a reduction of the bonding length (Lü et al., 2017) which can lead to amorphization at higher pressures (Oyelade et al., n.d.; Swainson et al., 2007). Consequently, pressure-induced crystallization improves structural, electrical, and optical properties of multilayered perovskite structures (G. Liu et al., 2017). Amorphization also is caused by atom rearrangement (Postorino & Malavasi, 2017; Swainson et al., 2007). Oyelade et. al. have shown that remotely applied pressures on perovskite solar cells can increase the power conversion efficiency, reduce interfacial defects, and induce higher stress at defect sites, which can cause induced crystallization.

Unlike rigid inorganic solar cells, these PSCs' production temperatures (annealing temperatures) are so low that the constituent materials can be flexible (Lee et al., 2019; Li et al., 2017; Park et al., 2015). The combination of mechanical flexibility and high PCE has stirred up a lot of interest in the field of study. A variety of highly flexible materials are used as the electrodes and electron-and hole-transport layers, the inimitable perovskite material components have organic-inorganic crystalline structures that can be brittle, and the brittleness level must be understood before

perovskite materials can be widely used. The structure, morphology, crystallinity, and photoelectric properties of perovskite films are all affected by the annealing temperature (L.-C. Chen et al., n.d.; Dualeh et al., 2014; M. Kim et al., 2017; Peng et al., 2016). The annealing process is also critical in the formation of perovskite film and consequently on the power conversion efficiency of the assembled devices (Wehrenfennig et al., 2014). Understanding the differences in the mechanical characteristics of perovskite structures processed under different annealing temperatures is crucial for device performance and reliability.

Additive engineering is used to passivate defects in perovskite to reduce the nonrelative recombination loss and enhance the PCE of the PSCs (J.-Q. Chen et al., 2019; Lei Guo, 2019). For the perovskite fabrication, various additives such as urea and polymer were developed and incorporated into the precursor solution. Rubidium cation (Rb) can be used to create a perovskite structure with outstanding photoelectric characteristics by incorporating it into a "cation cascade." Zhou and coworkers effectively introduced sodium fluoride into a perovskite absorber to improve PSC efficiency and stability by strengthening chemical bonding (Wu et al., 2015). The mentioned strategy aims at improving the film morphology and decreasing defects of the perovskite in flexible PSCs to improve their performance.

The mechanical robustness of inverted flexible PSCs was increased by introducing a small amount of novel additive polymer, polyoxyethylene (PEO) to the double-cation perovskite precursor, to promote the grain size and passivate the defects of the film. The PEO additive improved the quality of the perovskite film on the PET/ITO substrates. Specifically, both the grain size and crystallinity were significantly enhanced. We use a combined experimental and theoretical approach to study the failure and fatigue behavior of flexible perovskite solar cells.

1.2 Unresolved issues

The perovskite-based photovoltaic is a promising candidate for future energy technologies. But despite the number of advantages, PSCs remain within laboratories. PSC technology can progress to the industrial stage and begin the commercialization process if some significant concerns are addressed. The following are current obstacles in the commercialization of PSCs, as well as potential solutions to these issues:

1. Scale up

There are numerous reports on module production; however, not all these reports have included scalable methods for module manufacture. The development of large-area processing utilizing industry-compatible technologies and the fabrication of perovskite PV modules with many serially interconnected sub-cells transfer from laboratory to industrial manufacturing. The control and understanding of the nucleation and crystal growth mechanisms are critical in scaling up perovskites manufacture (Hu et al., 2020; C. Liu et al., 2020). Controlling crystal development will enable the production of high-quality perovskite films, which is the most critical aspect of the scalable method. Temperature, solvent composition, the surface qualities of the substrates, and, most importantly, post-deposition treatment can all influence it. The ability to create large-area perovskite films opens doors for PSC technologies to scale up and become more industrialized.

2. Stability

Another impediment to the commercialization of perovskite PV technology is the long-term stability of PSCs. Environmental variables such as water (or moisture), oxygen, heat, and UV light (Schileo & Grancini, 2020), as well as ion migration mechanisms (Domanski et al., 2017), induce PSC degradation. Therefore, knowing the degradation mechanisms in perovskite-based devices is

the only way to attain long-term stability. The addition of alkali cations such as cesium and rubidium to PSC improves its stability substantially (Domanski et al., 2017; Saliba et al., 2016). 2D perovskites demonstrate high stability against environmental factors because of the densely packed structure and hydrophobic nature of the used cation (Grancini et al., 2017). SAM deposited on the perovskite layer increased environmental stability (Wolff et al., 2020), and the inorganic transport layers are the most promising materials for stable PSCs (Coll et al., 2019).

3. Stability and scale

Layer homogeneity across a large area influences the stability of big-area devices. The stability of large-area modules depends on the fabrication of consistent pinhole-free and crack-free layers (J. Kim et al., 2017). For high-stability perovskite modules, research should focus on identifying intrinsically stable device stacks, understanding, and eliminating degradation processes at the cell and module levels, and developing an encapsulation strategy that will allow for high extrinsic stability and a long module lifetime.

4. Lead toxicity

Lead is a popular substance used in perovskite-based solar cells that are highly efficient (Pb). The environmental impact of lead-based PSCs is a source of challenge for their commercialization. Pb has been replaced or reduced in the ABX3 perovskite structure with less hazardous elements e.g., Ge, Sn, and Bi [50, 51 Debbi]. With a bandgap of roughly 1.3eV, Sn exhibits good optoelectronic characteristics. Sn_2^+ oxidizes to Sn_4^+, causing p-type doping of the material. Despite significant advances, the efficiency of Pb-free PSCs still lags considerably below that of traditional Pb-based systems. With appropriate encapsulation methods and recycling processes, the hazardousness of lead in the environment can be reduced.

To build mechanically robust and stable perovskite solar cells for deformable applications, an understanding of the underlying physics linking the structure of perovskite solar cells to their characteristics and mechanical stability is required.

1.3 Scope of the Thesis

The goal of this research is to find solutions to some of the above unresolved issues to enable the design of mechanically robust and stable perovskite solar cells for deformable and stretchable applications. An understanding of the underlying physics linking the structure of perovskite solar cells to their characteristics and mechanical stability is required. In this thesis a combined analytical, computational, and experimental method is used to study the effects of pressure on the photoconversion efficiencies of perovskite solar cells. Analytical model was used to predict the effects of pressure on interfacial contact in the multilayered structures of PSCs. A range of pressure values were applied to the devices to improve their interfacial surface contacts. The implications of the results are discussed for the fabrication of efficient PSCs. The effect of annealing temperature on the mechanical properties of hybrid organic-inorganic perovskite (HOIPs) was explored using a combined experimental and theoretical approach. A mechanism-based strain gradient (MSG) theory was used to explain the indentation size effects (ISE) in films at different annealing temperatures. The implications of the results are then discussed in the design of mechanically robust and stable perovskite solar cells (PSCs). And finally, the failure mechanisms in flexible perovskite solar cells are studied under monotonic and cyclic bending using experiments and simulations to gain insight to the interfacial cracking that can occur in the bi-layers and the multi-layers of the perovskite solar cells. The effects of monotonic and cyclic loading on the optical transmittance, power conversion efficiencies and fatigue lifetimes were studied. The implications

of the results were discussed for potential applications in flexible and stretchable power sources for electronic structures and devices.

Following the introduction and background in chapter 1, the detailed literature reviews on prior work are presented in chapter. Prior work discussed includes types of solar cells, operation principles of solar cells, perovskite solar cells, flexible perovskite solar cells, pressure effects on multilayered solar cell structures, annealing effects on the mechanical properties of PSCs, the fundamentals of fracture mechanics in electronic systems and the bending mechanics.

Chapter 3 presents the results of the effects of pressure on photoconversion efficiencies of perovskite solar cells (PSCs) using a combined experimental and analytical/computational study. First, an analytic model was used to predict the effects of pressure on the interfacial contact in the multilayered structures of PSCs. The PSCs were fabricated and a pressure range of 0-10 MPa was applied to improve the interfacial surface contacts. The result shows that crystallization, absorbance, and the power conversion efficiencies of PSCs can be significantly improved by the application of pressure. This results in the closing-up of voids and the corresponding increase in the interfacial surface contact lengths, which increases with increasing pressure. The observed improvement in the power conversion efficiencies was observed with increased pressure between 0 and 7 MPa, attributed largely to the effects of increased surface contact and the compaction and infiltration of the TiO_2 layers with perovskite during the application of pressure. At higher pressure values (> 7 Mpa), the damage due to sink of the perovskite layers into the mesoporous layers results in reductions in the photoconversion efficiencies of PSCs.

Chapter 4 presents the effects of annealing temperature on the mechanical properties of hybrid organic-inorganic perovskite (HOIPs). The mechanical properties (hardness and Young's modulus), microstructural, and surface topography of the HOIPs film at different annealing

temperatures ranging from 80 to 170^{o}C was examined. A mechanism-based strain gradient (MSG) theory was used to explain the indentation size effects (ISE) in films at different annealing temperatures. The intrinsic film yield strengths and hardness values (deduced from the MSG theory) are then shown to exhibit a Hall–Petch dependence on the inverse square root of the average grain size. The implications of the results were discussed for the design of mechanically robust perovskite solar cells (PSCs).

Chapter 5 presents the effects of PEO on failure mechanisms of flexible perovskite solar cells under monotonic and cyclic bending. The failure mechanisms for different radii were observed using a scanning electron microscope before the interfacial fracture energies in the multilayer devices are computed using finite element simulations. The failure mechanisms are then used to explain the degradation of the optical transmittance and current-voltage characteristics of flexible perovskite solar cells.

Finally, salient conclusions arising from this work are summarized in Chapter 6. Suggestions for future work are also presented.

1.4 References

Department of Energy (DOE), U. S. D. of E. (n.d.). *Clean Energy Solutions Center | Quadrennial Technology Review: An Assessment of Energy Technologies and Research Opportunities*. Retrieved January 3, 2022, from https://cleanenergysolutions.org/resources/quadrennial-technology-review-assessment-energy-technologies-research-opportunities

Asare, J., Adeniji, S. A., Oyewole, O. K., Agyei-Tuffour, B., Du, J., Arthur, E., Fashina, A. A., Zebaze Kana, M. G., & Soboyejo, W. O. (2016). Cold welding of organic light emitting diode:

Interfacial and contact models. *AIP Advances*, *6*(6), 065125. https://doi.org/10.1063/1.4955141

Best Research-Cell Efficiency Chart | Enhanced Reader. (n.d.). Retrieved October 1, 2021, from moz-extension://59238ff8-d379-460e-a75f-f63264ca7971/enhanced-reader.html?openApp&pdf=https%3A%2F%2Fwww.nrel.gov%2Fpv%2Fassets%2Fpdfs%2Fbest-research-cell-efficiencies.20190802.pdf

Capitani, F., Marini, C., Caramazza, S., Postorino, P., Garbarino, G., Hanfland, M., Pisanu, A., Quadrelli, P., & Malavasi, L. (2016). High-pressure behavior of methylammonium lead iodide (MAPbI3) hybrid perovskite. *Journal of Applied Physics*, *119*(18), 185901. https://doi.org/10.1063/1.4948577

Chapin, D. M., Fuller, C. S., & Pearson, G. L. (1954). A new silicon p-n junction photocell for converting solar radiation into electrical power [3]. In *Journal of Applied Physics* (Vol. 25, Issue 5, pp. 676–677). American Institute of PhysicsAIP. https://doi.org/10.1063/1.1721711 Chen, J.-Q., Huang, Q.-S., Qi, R.-Z., Feng, Y.-F., Feng, J.-T., Zhang, Z., Li, W.-B., & Wang, Z.-S. (2019). Effects of sputtering power and annealing temperature on surface roughness of gold films for high-reflectivity synchrotron radiation mirrors. *Nuclear Science and Techniques 2019 30:7*, *30*(7), 1–6. https://doi.org/10.1007/S41365-019-0635-X

Chen, L.-C., Wu, J.-R., Tseng, Z.-L., Chen, C.-C., Chang, S. H., Huang, J.-K., Lee, K.-L., & Cheng, H.-M. (n.d.). *materials Annealing Effect on (FAPbI 3) 1−x (MAPbBr 3) x Perovskite Films in Inverted-Type Perovskite Solar Cells*. https://doi.org/10.3390/ma9090747

Chen, Q., Zhou, H., Hong, Z., Luo, S., Duan, H. S., Wang, H. H., Liu, Y., Li, G., & Yang, Y. (2014). Planar heterojunction perovskite solar cells via vapor-assisted solution process. *Journal of the American Chemical Society*, *136*(2), 622–625. https://doi.org/10.1021/JA411509G/SUPPL_FILE/JA411509G_SI_001.PDF

Cho, K. T., Paek, S., Grancini, G., Roldán-Carmona, C., Gao, P., Lee, Y., & Nazeeruddin, M. K. (2017). Highly efficient perovskite solar cells with a compositionally engineered perovskite/hole transporting material interface. *Energy & Environmental Science*, *10*(2), 621–627. https://doi.org/10.1039/C6EE03182J

Coll, M., Fontcuberta, J., Althammer, M., Bibes, M., Boschker, H., Calleja, A., Cheng, G., Cuoco, M., Dittmann, R., Dkhil, B., El Baggari, I., Fanciulli, M., Fina, I., Fortunato, E., Frontera, C., Fujita, S., Garcia, V., Goennenwein, S. T. B., Granqvist, C. G., … Granozio, F. M. (2019). Towards Oxide Electronics: a Roadmap. *Applied Surface Science*, *482*, 1–93. https://doi.org/10.1016/J.APSUSC.2019.03.312

Domanski, K., Roose, B., Matsui, T., Saliba, M., Turren-Cruz, S. H., Correa-Baena, J. P., Carmona, C. R., Richardson, G., Foster, J. M., De Angelis, F., Ball, J. M., Petrozza, A., Mine, N., Nazeeruddin, M. K., Tress, W., Grätzel, M., Steiner, U., Hagfeldt, A., & Abate, A. (2017). Migration of cations induces reversible performance losses over day/night cycling in perovskite solar cells. *Energy & Environmental Science*, *10*(2), 604–613. https://doi.org/10.1039/C6EE03352K

Du, J., Anye, V. C., Vodah, E. O., Tong, T., & Kana, M. G. Z. (2014). *layer materials Pressure-assisted fabrication of organic light emitting diodes with MoO 3 hole-injection layer materials*. *233703*. https://doi.org/10.1063/1.4881780

Dualeh, A., Tétreault, N., Moehl, T., Gao, P., Nazeeruddin, M. K., & Grätzel, M. (2014). Effect of Annealing Temperature on Film Morphology of Organic–Inorganic Hybrid Pervoskite Solid-State Solar Cells. *Advanced Functional Materials*, *24*(21), 3250–3258. https://doi.org/10.1002/ADFM.201304022

Ellabban, O., Abu-Rub, H., & Blaabjerg, F. (2014). Renewable energy resources: Current status, future prospects and their enabling technology. In *Renewable and Sustainable Energy Reviews* (Vol. 39, pp. 748–764). Elsevier Ltd. https://doi.org/10.1016/j.rser.2014.07.113

Grancini, G., Roldán-Carmona, C., Zimmermann, I., Mosconi, E., Lee, X., Martineau, D., Narbey, S., Oswald, F., De Angelis, F., Graetzel, M., & Nazeeruddin, M. K. (2017). One-Year stable perovskite solar cells by 2D/3D interface engineering. *Nature Communications 2017 8:1*, *8*(1), 1–8. https://doi.org/10.1038/ncomms15684

Hu, H., Singh, M., Wan, X., Tang, J., Chu, C. W., & Li, G. (2020). Nucleation and crystal growth control for scalable solution-processed organic–inorganic hybrid perovskite solar cells. *Journal of Materials Chemistry A*, *8*(4), 1578–1603. https://doi.org/10.1039/C9TA11245F

Institute for Energy Economics and Financial Economics (IEEFA), 2019. *IEA: Renewable generation capacity expected to climb by 1,200GW in next five years - Institute for Energy Economics & Financial Analysis*. Retrieved January 3, 2022, from https://ieefa.org/iea-renewable-generation-capacity-expected-to-climb-by-1200gw-in-next-five-years/

IEEFA, 2019. (2010). US Energy Information Administration. *International Energy Outlook*.

Interview with Greatcell Solar Materials' GM Yanek Hebting. (2019). https://www.perovskite-info.com/interview-greatcell-solar-materials-gm-yanek-hebting

International Renewable Energy Agency (IRENA) (2019), F. of S. P. D., & aspects (A Global Energy Transformation: paper), I. R. E. A. (2019). FUTURE OF SOLAR PHOTOVOLTAIC Deployment, investment, technology, grid integration and socio-economic aspects. In International Renewable Energy Agency (Ed.), *International Renewable Energy Agency* (pp. 1–73). IRENA.

Jeng, J. Y., Chiang, Y. F., Lee, M. H., Peng, S. R., Guo, T. F., Chen, P., & Wen, T. C. (2013). CH3NH3PbI3 Perovskite/Fullerene Planar-Heterojunction Hybrid Solar Cells. *Advanced Materials*, *25*(27), 3727–3732. https://doi.org/10.1002/ADMA.201301327

Jeon, N. J., Noh, J. H., Kim, Y. C., Yang, W. S., Ryu, S., & Seok, S. Il. (2014). Solvent engineering for high-performance inorganic–organic hybrid perovskite solar cells. *Nature Materials 2014 13:9*, *13*(9), 897–903. https://doi.org/10.1038/nmat4014

Kim, J., Yun, J. S., Cho, Y., Lee, D. S., Wilkinson, B., Soufiani, A. M., Deng, X., Zheng, J., Shi, A., Lim, S., Chen, S., Hameiri, Z., Zhang, M., Lau, C. F. J., Huang, S., Green, M. A., & Ho-Baillie, A. W. Y. (2017). Overcoming the Challenges of Large-Area High-Efficiency Perovskite Solar Cells. *ACS Energy Letters*, *2*(9), 1978–1984. https://doi.org/10.1021/ACSENERGYLETT.7B00573/SUPPL_FILE/NZ7B00573_SI_002.AVI

Kim, M., Kim, G. H., Oh, K. S., Jo, Y., Yoon, H., Kim, K. H., Lee, H., Kim, J. Y., & Kim, D. S. (2017). High-Temperature-Short-Time Annealing Process for High-Performance Large-Area Perovskite Solar Cells. *ACS Nano*, *11*(6), 6057–6064. https://doi.org/10.1021/ACSNANO.7B02015/SUPPL_FILE/NN7B02015_SI_001.PDF

Kim, Y. H., Cho, H., Heo, J. H., Kim, T. S., Myoung, N. S., Lee, C. L., Im, S. H., & Lee, T. W.

(2015). Multicolored organic/inorganic hybrid perovskite light-emitting diodes. *Advanced Materials (Deerfield Beach, Fla.)*, *27*(7), 1248–1254. https://doi.org/10.1002/ADMA.201403751

Kojima, A., Teshima, K., Shirai, Y., & Miyasaka, T. (2009). *Organometal Halide Perovskites as Visible-Light Sensitizers for Photovoltaic*. 6050–6051.

Lee, G., Kim, M. C., Choi, Y. W., Ahn, N., Jang, J., Yoon, J., Kim, S. M., Lee, J. G., Kang, D., Jung, H. S., & Choi, M. (2019). Ultra-flexible perovskite solar cells with crumpling durability: toward a wearable power source. *Energy & Environmental Science*, *12*(10), 3182– 3191. https://doi.org/10.1039/C9EE01944H

Lei Guo, Gang Tang, Jiawang Hong (2019). Mechanical Properties of Formamidinium Halide Perovskites FABX$_{3}$ (FA=CH(NH$_{2})_{2}$; B=Pb, Sn; X=Br, I) by First-Principles Calculations. *Chinese Physics Letters*, *36*(5), 056201. https://doi.org/10.1088/0256-307X/36/5/056201

Li, D., Jen, A. K., Zhang, H., Cheng, J., Li, D., Lin, F., Mao, J., Liang, C., Jen, A. K., Grätzel, M., & Choy, W. C. H. (2017). *Toward All Room-Temperature , Solution- Processed , High-Performance Planar Perovskite Solar Cells : A . Toward All Room-Temperature , Solution-Processed , High-Performance Planar Perovskite Solar Cells : A New Scheme of Pyridine-Promoted Perovskite For*. *January*. https://doi.org/10.1002/adma.201604695

Liu, C., Cheng, Y. B., & Ge, Z. (2020). Understanding of perovskite crystal growth and film formation in scalable deposition processes. *Chemical Society Reviews*, *49*(6), 1653–1687. https://doi.org/10.1039/C9CS00711C

Liu, G., Kong, L., Gong, J., Yang, W., Mao, H. K., Hu, Q., Liu, Z., Schaller, R. D., Zhang, D., &

Xu, T. (2017). Pressure-Induced Bandgap Optimization in Lead-Based Perovskites with Prolonged Carrier Lifetime and Ambient Retainability. *Advanced Functional Materials*, *27*(3), 1604208. https://doi.org/10.1002/ADFM.201604208

Lü, X., Yang, W., Jia, Q., & Xu, H. (2017). Pressure-induced dramatic changes in organic–inorganic halide perovskites. *Chemical Science*, *8*(10), 6764–6776. https://doi.org/10.1039/C7SC01845B

Mali, S. S., Shim, C. S., & Hong, C. K. (2015). Highly stable and efficient solid-state solar cells based on methylammonium lead bromide (CH3NH3PbBr3) perovskite quantum dots. *NPG Asia Materials 2015 7:8*, *7*(8), e208–e208. https://doi.org/10.1038/am.2015.86

Mao, L., Meng, Q., Ahmad, A., & Wei, Z. (2017). Mechanical analyses and structural design requirements for flexible energy storage devices. *Advanced Energy Materials*, *7*(23). https://doi.org/10.1002/AENM.201700535

Miyata, A., Mitioglu, A., Plochocka, P., Portugall, O., Tse-Wei Wang, J., Stranks, S. D., Snaith, H. J., & Nicholas, R. J. (2015). Direct measurement of the exciton binding energy and effective masses for charge carriers in organic–inorganic tri-halide perovskites. *NATURE PHYSICS* |, *11*. https://doi.org/10.1038/NPHYS3357

Oyelade, O. V, Oyewole, O. K., Adeniji, S. A., Ichwani, R., Sanni, D. M., & Soboyejo, W. O. (n.d.). *pressure-Assisted fabrication of perovskite Solar cells*. https://doi.org/10.1038/s41598-020-64090-5

Park, M., Kim, H. J., Jeong, I., Lee, J., Lee, H., Son, H. J., Kim, D.-E., & Ko, M. J. (2015). Mechanically Recoverable and Highly Efficient Perovskite Solar Cells: Investigation of Intrinsic Flexibility of Organic–Inorganic Perovskite. *Advanced Energy Materials*, *5*(22),

1501406. https://doi.org/10.1002/AENM.201501406

Peng, W., Anand, B., Liu, L., Sampat, S., Bearden, B. E., Malko, A. V., & Chabal, Y. J. (2016). Influence of growth temperature on bulk and surface defects in hybrid lead halide perovskite films. *Nanoscale*, *8*(3), 1627–1634. https://doi.org/10.1039/C5NR06222E

Postorino, P., & Malavasi, L. (2017). Pressure-Induced Effects in Organic–Inorganic Hybrid Perovskites. *Journal of Physical Chemistry Letters*, *8*(12), 2613–2622. https://doi.org/10.1021/ACS.JPCLETT.7B00347

Saliba, M., Matsui, T., Seo, J. Y., Domanski, K., Correa-Baena, J. P., Nazeeruddin, M. K., Zakeeruddin, S. M., Tress, W., Abate, A., Hagfeldt, A., & Grätzel, M. (2016). Cesium-containing triple cation perovskite solar cells: improved stability, reproducibility and high efficiency. *Energy & Environmental Science*, *9*(6), 1989–1997. https://doi.org/10.1039/C5EE03874J

Schileo, G., & Grancini, G. (2020). Halide perovskites: current issues and new strategies to push material and device stability. *JPhys Energy*, *2*(2). https://doi.org/10.1088/2515-7655/AB6CC4

Swainson, I. P., Tucker, M. G., Wilson, D. J., Winkler, B., & Milman, V. (2007). Pressure response of an organic-inorganic perovskite: Methylammonium lead bromide. *Chemistry of Materials*, *19*(10), 2401–2405. https://doi.org/10.1021/CM0621601

Szabó, L. (2017, July 10). The history of using solar energy. *Proceedings - 2017 International Conference on Modern Power Systems, MPS 2017*. https://doi.org/10.1109/MPS.2017.7974451

Tan, Z. K., Moghaddam, R. S., Lai, M. L., Docampo, P., Higler, R., Deschler, F., Price, M., Sadhanala, A., Pazos, L. M., Credgington, D., Hanusch, F., Bein, T., Snaith, H. J., & Friend, R. H. (2014). Bright light-emitting diodes based on organometal halide perovskite. *Https://Eprints.Ncl.Ac.Uk*, *9*(9), 687–692. https://doi.org/10.1038/NNANO.2014.149

US Department of Energy. (2012). *Basic Research Needs for Solar Energy Utilization*. *66*, 37–39.

Valverde-Chávez, D. A., Ponseca, C. S., Stoumpos, C. C., Yartsev, A., Kanatzidis, M. G., Sundström, V., & Cooke, D. G. (2015). Intrinsic femtosecond charge generation dynamics in single crystal CH3NH3PbI3. *Energy and Environmental Science*, *8*(12), 3700–3707. https://doi.org/10.1039/c5ee02503f

Wehrenfennig, C., Eperon, G. E., Johnston, M. B., Snaith, H. J., Herz, L. M., Wehrenfennig, C., Eperon, G. E., Johnston, M. B., Snaith, H. J., & Herz, L. M. (2014). High Charge Carrier Mobilities and Lifetimes in Organolead Trihalide Perovskites. *Adv. Mater*, *26*, 1584–1589. https://doi.org/10.1002/adma.201305172

Wolff, C. M., Canil, L., Rehermann, C., Ngoc Linh, N., Zu, F., Ralaiarisoa, M., Caprioglio, P., Fiedler, L., Stolterfoht, M., Kogikoski, S., Bald, I., Koch, N., Unger, E. L., Dittrich, T., Abate, A., & Neher, D. (2020). Perfluorinated Self-Assembled Monolayers Enhance the Stability and Efficiency of Inverted Perovskite Solar Cells. *ACS Nano*, *14*(2), 1445–1456. https://doi.org/10.1021/ACSNANO.9B03268/SUPPL_FILE/NN9B03268_SI_001.PDF

Wu, C.-G., Chiang, C.-H., Tseng, Z.-L., Nazeeruddin, M. K., Hagfeldt, A., & Grätzel, M. (2015). High efficiency stable inverted perovskite solar cells without current hysteresis. *Energy & Environmental Science*, *8*(9), 2725–2733. https://doi.org/10.1039/C5EE00645G

Zhang, L., Wang, K., Lin, Y., & Zou, B. (2020). Pressure Effects on the Electronic and Optical

Properties in Low-Dimensional Metal Halide Perovskites. *The Journal of Physical Chemistry Letters*, *11*(12), 4693–4701. https://doi.org/10.1021/ACS.JPCLETT.0C01014

Zhao, Q., Li, G. R., Song, J., Zhao, Y., Qiang, Y., & Gao, X. P. (2016). Improving the photovoltaic performance of perovskite solar cells with acetate. *Scientific Reports 2016 6:1*, *6*(1), 1–10. https://doi.org/10.1038/srep38670

Zheng, F., Saldana-Greco, D., Liu, S., & Rappe, A. M. (2015). Material Innovation in Advancing Organometal Halide Perovskite Functionality. *Journal of Physical Chemistry Letters*, *6*(23), 4862–4872. https://doi.org/10.1021/ACS.JPCLETT.5B01830

Zhou, D., Zhou, T., Tian, Y., Zhu, X., & Tu, Y. (2018). Perovskite-Based Solar Cells: Materials, Methods, and Future Perspectives. *Journal of Nanomaterials*, *2018*. https://doi.org/10.1155/2018/8148072

Chapter 2

BASIC THEORY AND LITERATURE REVIEW

2.0 Introduction

This chapter reviews the physics of solar cells and the perovskite solar cells. The effects of pressure on the efficiency and annealing temperature on the mechanical properties of the perovskite solar cells are discussed along with the fundamentals of bending mechanics and fracture mechanics in flexible/stretchable electronics systems.

2.1 Physics of Solar Cells

Solar cells are semiconductor materials that absorb photons and convert them to electricity based on the photovoltaic effect. The semiconductor material separates the absorbed photons into free charge carriers that travel in a specified direction to generate photocurrent and power an external load. The PN junction is the semiconductor material used for this photovoltaic energy conversion. Figure 2.1 shows a schematic of the cross section of a solar cell. The solar cell consists of a metallic grid front electrode, sometimes an anti-reflective coating, a PN junction diode and the metallic electrode as the bottom contact.

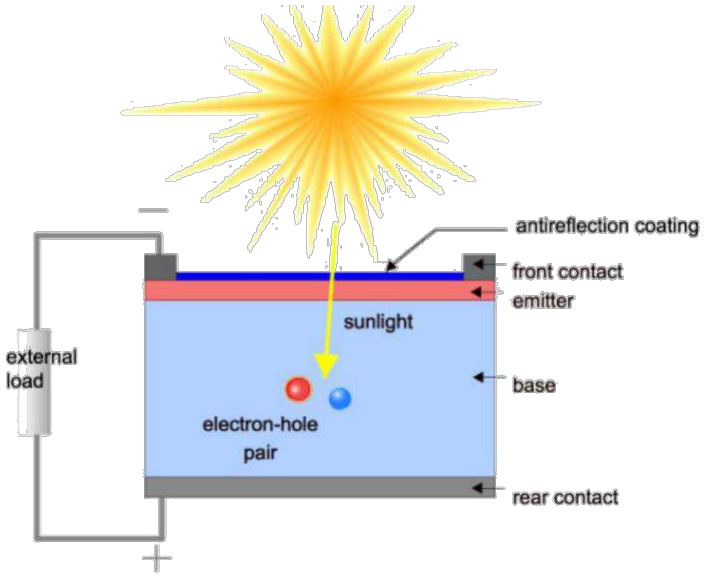

Figure 2.1. The cross section of solar cell

Electromagnetic radiations like sunlight are composed of particles called photons that carry a specific amount of energy determined by the spectral properties of their source. The photon energy E is given as:

$$= h \quad (2.1)$$

Photons behave like waves and the energy of photon in terms of wavelength is written as

$$= \frac{h}{} \quad (2.2)$$

where h is Plank's constant, is the frequency of light, is the speed of light and is the wavelength of the photons.

When photons arrive with enough energy to knock one of the electrons loose, the negatively charged particle will gravitate toward the p-type material, resulting in an electron-hole pair. An electric field exists because of the gradient between the n-type

and p-type materials; the electric field causes charges to flow in a specific direction, resulting in current flow. Only photons with enough energy to form an electron-hole pair, i.e., photons with energy more than the bandgap, will contribute to the energy conversion process. As a result, the spectral composition of sunlight is a critical factor in the development of efficient solar cells.

The charge carriers created during illumination are separated by the electric field created by the PN junction of the semiconductor. The electric current, I, then flows through the external circuit. A solar cell can have the exponential characteristic like a typical diode if the energy of photons is greater than the bandgap. The current-voltage characteristic of the ideal solar cell is described using the Schockley diode equation as follows (Rodrigues et al., 2011)

$$= \quad -(\quad / \quad -1) \tag{2.3}$$

where = output current, = saturation current, $_0$ = diode reverse bias, = electron charge (1.602176 x 10^{-19}C), V = terminal voltage of the solar cell, m = diode ideality factor, K = Boltzmann's constant (1.380650 x 10^{-23} J/K), and T = temperature of the cell.

The maximum output power of solar cells is characterized by three parameters namely: the short circuit current (I_{sc}), open circuit voltage (V_{oc}) and the diode ideality factor (m). The I_{sc} is the highest current that can be generated by the solar cell, and is given by (Rodrigues et al., 2011)

$$= = (\quad = 0) \tag{2.5}$$

The V_{oc} is the highest value of voltage that can be obtained at the cell terminals when the current is zero. It is given by

$$= \_\_\_\_\_ (1 + \_\_\_\_ \_\_) \quad (h \quad = 0) \tag{2.6}$$

The power output can then be computed as

$$= [\quad - (\quad / \quad - 1)] \tag{2.7}$$

2.2 Perovskite Solar Cells

In this section, the background of perovskite solar cells will be discussed. The efforts made so far on the processing conditions that have been used to improve the power conversion efficiencies of perovskite solar cells will also be employed.

Recently, organic-inorganic hybrid perovskites have gained recognition due to advantages such as high electron and hole mobility (10 – 60 $cm^2V^{-1}s^{-1}$), bandgap tunability, long carrier diffusion length (~ 1 μm), and low exciton binding energy (30 – 50 meV) (Song et al., 2016). Besides these advantages, perovskite solar cells (PSCs) can be made from low-cost processes and materials and be manufactured on roll-to-roll flexible substrates (Green et al., 2020; M, 2014).

The immense potential of PSCs is evident in their efficiency that has increased from 3.8 % to 25.2 % (28% in tandem architecture) in less than a decade, and it is still increasing while other technologies took nearly 30 years to witness this milestone (*Best Research-Cell Efficiency Chart | Enhanced Reader*, 2020). Figure 2.2 depicts the advancement of PSCs over the years (Roy et al., 2020). PSCs have developed quickly as compared to silicon solar cells. PSCs can be synthesized in laboratories using wet chemistry and low-cost processes like spin coating, dip coating, screen printing, dual-source evaporation techniques, and so on.

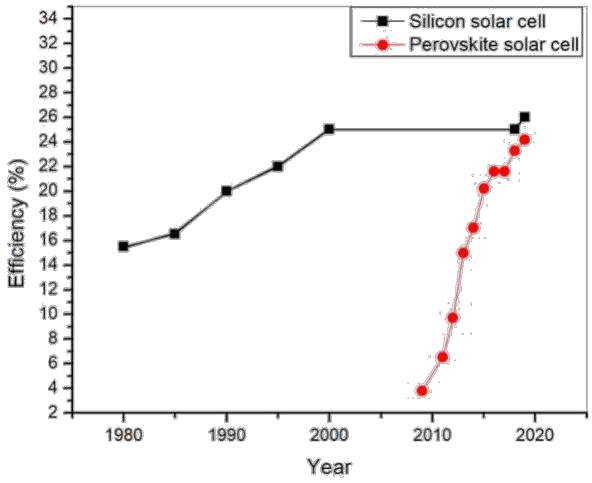

Figure 2.2. Recorded power conversion efficiency of the PSCs in progressive years (Roy et al., 2020)

Calcium titanium oxide is the main component of perovskite ($CaTiO_3$). Gustav Rose discovered it in the Ural Mountains of Russia in 1939. Count Lev Alekseevich Perovski (1972–1856), a Russian mineralogist, continued the investigation, and the material was named Perovskite after him (Miyata et al., 2015). Mitzi and colleagues studied the optoelectronic characteristics of organic-inorganic perovskites in the 1990s. They reported that the material demonstrated high exciton properties and suggested that it can be used in LEDs, transistors, and solar cells (DB et al., 1995). Kojima and coworkers were the first to observe PV generation in this material. They were the first to use perovskite as a liquid sensitizer in a DSSC design in solar cells in 2009.

The crystal structure of Perovskite materials is like that of Calcium Titanate ($CaTiO_3$), and the typical formula is ABX_3 (where X is generally Oxygen, Nitrogen, Carbon, or Halogen). There are two types of halide perovskites: alkali halide perovskites and organic-inorganic halide perovskites. The alkali halide perovskite comprises monovalent alkali cation (A) as Cs^+, Rb^+, K^+, Na^+ and Li^+, divalent cation (B) as (Pb^{2+}, Sn^{2+}, Ge^{2+}) and halogen anions (X) as Cl^-, Br^-, I^-, F^-. Organic-inorganic halide-based perovskite has organic monovalent cation (A) as $CH_3NH_3^+$, $CH_3CH_2NH_3^+$,

$NH_2CHNH_2^+$ (H.-S. Kim et al., 2014). A typical unit cell structure of a basic perovskite compound is shown in Figure 2.3. The halide-based perovskite has attractive electrical, optical, and magnetic properties that enables users to apply them in the field of solar cells (Sarukura et al., 2007).

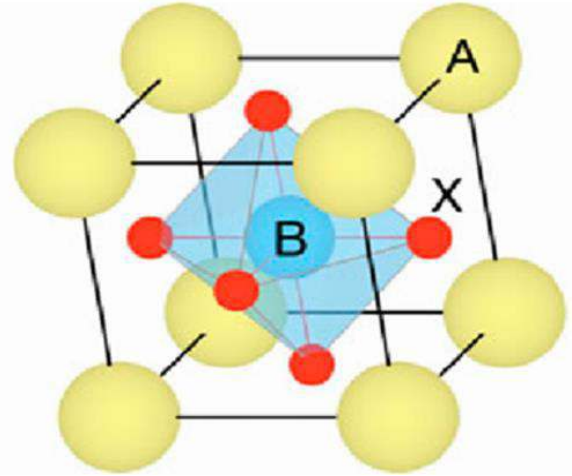

Figure 2.3. A generic perovskite crystal structure of the form ABX_3 (Jain et al., 2013)

The perovskite formation tendency can be depicted by using Goldschmidt tolerance factor (t) which is given by

$$= \frac{}{\sqrt{2}(\quad)} \qquad (2.8)$$

$$\mu = \frac{}{} \qquad (2.9)$$

where R_A, R_B, and R_x represent ionic radii of A, B cation and X anion respectively. For a perovskite crystal structure that is stable, the tolerance factor is between 0.88 and 1.1. Perovskite is commonly assumed to be stable if 't' is within the stated range, although it has also been observed that perovskite is not stable even when 't' is in the 0.8–0.9 range (C. Li et al., 2008).

An additional consideration for perovskite formation is the octahedral factor (μ) given by equation (2.9). It determines the distortion and stability of perovskite structure. The perovskite is stabilized for an octahedral factor ranging from 0.45 to 0.89 (Travis et al., 2016).

Methylammonium lead trihalide ($MAPbI_3$, where X is the halide: Cl, Br, or I) is the most common absorber material used in PSC. The unit cell parameters increase from 5.68 to 5.92 to 6.27 Å as the size of the halide atom increases from Cl to Br to I. However, because of its spherical shape and bigger size, Methylammonium (MA) causes network distortion, resulting in phase transition with a drop in temperature.

For $T < 160$ K, the orthorhombic structure, for $162.2\ K < T < 327.4$ K tetragonal structure, and for $T > 32.4$ K cubic structure is observed (C. Li et al., 2008). Methylammonium lead halide has a bandgap of 1.5–2.3 eV on average. $MAPbI_3$ is a direct bandgap material with a bandgap of approximately 1.55 eV, whereas $MAPbBr_3$ has a significantly broader bandgap of 2.3 eV with absorption beginning around 800 nm. $FAPbI_3$ (where FA is Formamidinium) has a narrower bandgap of 1.48 eV, indicating more current extraction when used as the absorber but this material has shown to be less stable. Depending on the type of halogen atom employed, the structural properties of methylammonium lead halide vary. The lattice constant gets reduced by utilizing smaller Br instead of I, resulting in a more stable cubic phase. This fact is also evident by examining the crystal structures of $MAPbI_3$ and $MAPbBr_3$, which crystallize in tetragonal and cubic forms, respectively (Heo et al., 2013).

The components of the PSCs are (i) a metal-based cathode (ii) hole transport layer (HTL) (iii) absorber layer (iv) electron transport layer (ETL) (v) transparent conductive oxide (TCO). The transport layers are crucial in determining the PSC's performance. HTL collects holes from the absorber layer and transports them to the cathode, blocking the electrons. Materials used as a hole

transport material (HTMs) must have a highest occupied molecular orbital (HOMO) slightly higher than the perovskite absorber's layer. Some examples of HTMs are Spiro-OMeTAD, NiO, CuO, CuI, Cu_2O, PTAA, etc. ETL collects electrons from the absorber layer and transports them to the anode, where they prevent holes. The HOMO and LUMO (lowest unoccupied molecular orbital) levels of material must be greater than the perovskite absorber layer for it to be an electron transport material (ETM). In the UV–Vis range, the ETMs must have a high transmittance so that all photons pass through and are absorbed to their maximum potential by the absorber layer. Some examples of ETMs are TiO_2, SnO_2, SiO_2, ZnO, etc. Transport layers must have these properties: thermal stability, non-toxicity, and resistance to external degrading forces ((Asare et al., 2021; Mahmood et al., 2017).

The device architecture is paramount in determining perovskite solar cells' overall performance. Depending on which transport (electron/hole) material is present on the outside portion of the cell encountered by incident light initially, PSCs can be classified as regular (n-i-p) or inverted (p-i-n). These two types of structures can be grouped into mesoscopic and planar structures. Figure 2.4 shows the typical structures of PSCs.

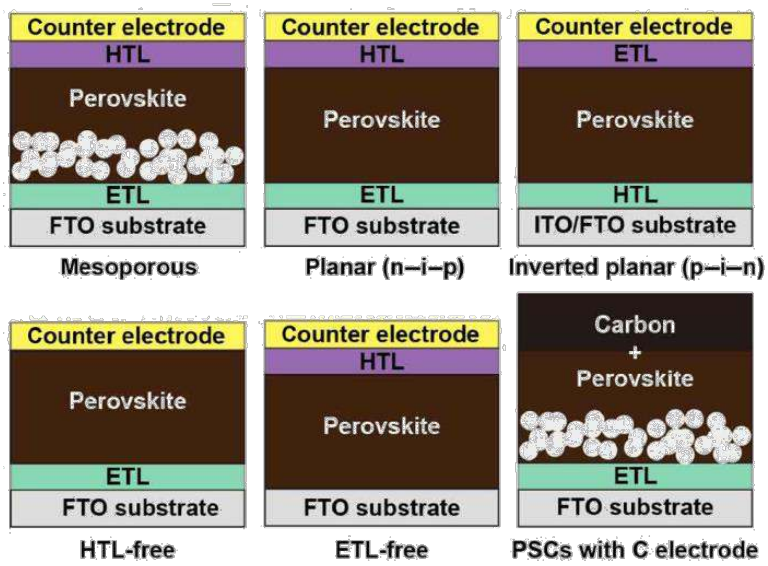

Figure 2.4. Typical structures of PSCs (Da & Zheng, 2017)

2.3. Perovskite material

The perovskite material used for light harvesting contains a monovalent cation, a divalent cation, and a halide ion. The light-harvesting perovskite material contains a monovalent cation, a divalent cation, and a halide ion. Mixed cation, mixed halide, and mixed halide–mixed cation perovskites are gaining popularity as alternatives to the classic $MAPbI_3$ perovskite. Furthermore, researchers are looking for alternatives to Pb to prevent lead's inherent toxicity.

2.3.1 Monovalent cation exchange/mixing

The performance of PSCs can be improved by modifying monovalent cations. Due to its inadequate bandgap and concerns with long-term stability, researchers are looking for new functional materials to replace methylammonium (MA) in $MAPbI_3$ (J. W. Lee et al., 2014). The ideal band gap for a single-junction solar cell is between 1.1 and 1.4 eV, whereas $MAPbI_3$ has band gaps of 1.50 to 1.61 eV (Zhu et al., 2016). The efficiency of PSC can be improved by employing perovskites with a lower bandgap than $MAPbI_3$. A modification of the monovalent cation in lead

halide-based perovskite may result in a change in the Pb-I bond length and angle, leading to a change in the overall band structure (W. S. Yang et al., 2015). By replacing the MA ion with a slightly larger organic formamidinium (FA) ion, a cubic structure with a larger lattice is formed, resulting in a slight decrease in the band gap from 1.59 eV for $MAPbI_3$ to 1.45–1.52 eV for $FAPbI_3$, which is closer to the optimal band gap of a single junction solar cell and thus allows for more light harvesting (Aharon et al., 2014). Hanusch et al. demonstrated that $FAPbI_3$ is thermally more stable than both $MAPbI_3$ and $MAPbBr_3$, supporting the hypothesis that a bigger cation at the A site in the ABX_3 structure could further stabilize the perovskite structure (Mei et al., 2014). However, $FAPbI_3$ can crystallize into either the photoinactive non-perovskite hexagonal-phase (yellow phase) or the photoactive perovskite -phase (black phase) (Jeon et al., 2015), both of which are vulnerable to solvent contamination and humidity, causing stability difficulties.

For further enhancement, monovalent cations can be exchanged with inorganic materials if they stay within the tolerance factor range. Although $CsPbI_3$ has high thermal stability, it lacks an ideal band gap (1.73 eV) for single-junction photovoltaics and is unstable in the cubic (or pseudo-cubic)-phase at room temperature (Correa-Baena et al., 2017).

For greater efficiency and long-term structural and thermal stability, perovskites containing mixed cations/mixed halide ions were used. The mixing of a tiny fraction of MA with FA (double cation perovskites) results in improved photoactive black phase crystallization and consequently thermal and structural stability than pure MA or FA perovskites (J.-W. Lee et al., 2015).

Perovskites with organic-inorganic double cations were also studied. Choi et al. reported that adding 10% Cs to the $MAPbI_3$ perovskite structure increased device efficiency by 40% by improving light absorption and morphology. It also increased the energy difference between the perovskite valence band and the lowest unoccupied molecular orbital (LUMO) level of PCBM (C.

Liu et al., 2016). Lee et al. discovered that $FA_{0.9}Cs_{0.1}PbI_3$ had a significantly better photo and moisture stability than pure $FAPbI_3$. The triple-cation (Cs/MA/FA)-based perovskite solar cells have a higher reproducibility and thermal stability than the MA/FA double-cation perovskites (Correa-Baena et al., 2017). The addition of Cs to the MA/FA cation combination aids to dissipate the photo-inactive hexagonal - δ phase of $FAPbI_3$ and the cubic PbI_2 completely.

2.3.2. Halide substitution/mixing

The optoelectronic properties of perovskites can be tuned by replacing or combining halogen ions. The iodine in the structure of the lead halide perovskite ($MAPbI_3$) can be replaced with chlorine or bromine, and larger single crystals have been grown from all three lead halide perovskites: $MAPbCl_3$, $MAPbBr_3$, and $MAPbI_3$ (Figure 2.5). Liu et al. discovered a substantial change in absorbance characteristics when halide substitution occurs between Cl, Br, and I. The bandgap energy of halide decreases as the ionic size of the halide increases; for example, the bandgap energy of the Cl, Br, and I perovskite is 2.97, 2.24, and 1.53 eV, respectively, for a single crystal (Suarez et al., 2014). Further, because the PL peak values are less than the absorption onsets, they can be used in solar cells.

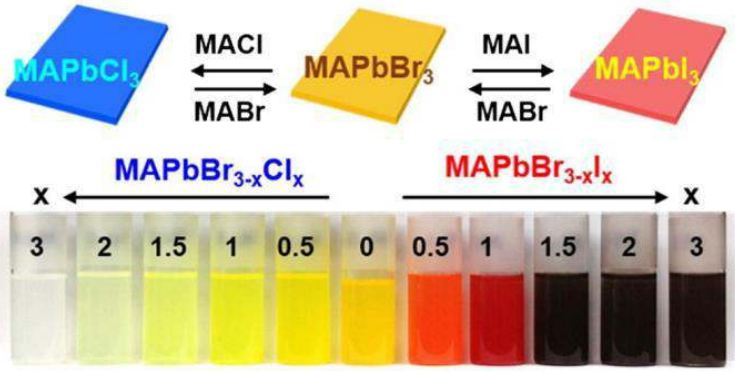

Figure 2.5. Photograph of halide substitution/mixing in the perovskite structure (Suarez et al., 2014)

Both $MAPbI_3$ and $MAPbBr_3$ are suitable for single bandgap absorbers and tandem applications, whereas MAPbCl3 is better for light-emitting devices (J.-W. Lee et al., 2015). $MAPb(I_{1-x}Cl_x)_3$ demonstrated a stability advantage over $MAPbI_3$ during air processing (M. M. Lee et al., 2012). $MAPb(I_{1-x}Cl_x)_3$ also has longer electron-hole diffusion lengths than $MAPbI_3$, while $MAPb(I_{1-x}Br_x)_3$ and $MAPb(Br_{1-x}Cl_x)_3$ showed increased carrier mobility and lower carrier recombination rates (Jacobsson et al., 2016). Mixed (I, Cl) perovskite is difficult to synthesize below 625 K, but mixed (Br, Cl) and (I, Br) perovskite are easy to synthesize at room temperature (Noel et al., 2014). As a result, the I/Br-halide combination appears to offer better overall performance.

2.3.3 Divalent metal cation exchange/mixing

Even though the efficiency of lead-based perovskites has progressively improved over the last few years, lead toxicity continues to stymie commercialization attempts and remains an unsolved negative. Sn, Ge, Cu, Sb, Bi, and Sr are elements that have been studied extensively as prospective lead substitutes (L. Li et al., 2017). Sn-based perovskites ($MASnI_3$) have been found to have up to a 6% efficiency (Krishnamoorthy et al., 2015). But Sn-based perovskites are prone to self-doping effects and structural instabilities, such as the ability to oxidize from Sn^{2+} to Sn^{4+}. As a result, perovskites based on Sn deteriorate faster when exposed to ambient air. Due to their low toxicity and improved performance, Pb-Sn binary perovskites have recently gained a lot of attention. Attempts made to regulate the chemical composition of Pb and Sn and optimize the production process (W et al., 2016) yielded a PCE of 15.08 % with good reproducibility (Qian et al., 2016). Another possibility for a divalent metal cation in a perovskite structure is germanium (Ge). Ge was

shown to be a good candidate element for substituting Pb in computational screening based on density-functional-theory (DFT) simulations (Conings et al., 2014).

2.4. Preparation methods of the Perovskite Light-Absorbing Layer

The light-absorbing layer of perovskite solar cells is synthesized using one of three methods: solution, vapor deposition, or vapor-assisted solution. The solution approach is straightforward and cost-effective, but synthesized crystals produce more internal defects, and the hole transport layer is in direct contact with the electron transport layer, lowering the device's filling factor and open-circuit voltage. The solution synthesis methods can be divided into one-and two-step methods according to the number of deposition steps (Barnett et al., 2016; Burschka et al., 2013; Liang et al., 1998; You et al., 2014).

The vapor-deposition process produces perovskite films with a high surface density and fewer defects, which improves the fill factor and open-circuit voltage. However, this process requires a high-vacuum environment and consumes a lot of energy (C.-W. Chen et al., 2014; Forgács et al., 2017; Green et al., 2014; M. Liu et al., 2013). The vapor-assisted solution approach combines the benefits of both the solution and evaporation methods (Q. Chen et al., 2014). Perovskites with fewer internal defects can be produced at a lower vacuum. The various deposition methods for the perovskite layer are shown in Figure 2.6.

2.5. Flexible Perovskite Solar Cells

Flexible thin-film solar cells have a wide range of possible uses, including portable electronic chargers, bendable display systems, and wearable electronic fabrics because of their lightweight, bendability, and ease of shape changeability (Kaltenbrunner et al., 2015; Lipomi & Bao, 2011). The low-temperature processing (below 150 °C), all-solid-state nature of the thin films, and high

efficiency of perovskite solar cells make them appealing as flexible solar cells. Flexible perovskite solar cells are still in their infancy, so there is plenty of possibility for advancement. Two types of configurations, n-i-p, and p-i-n junctions, incorporating electron transport materials (ETM)/perovskite/HTM and HTM/perovskite/ETM architectures, have been used to make flexible perovskite solar cells. Most flexible perovskite solar cells on ITO-coated poly(ethylene terephthalate) (PET) substrates have adopted p-i-n structures (or inverted planar structures) composed of PEDOT:PSS/perovskite/PCBM architectures (Figure 2.7 (a)), because conventional processes for the fabrication of ETM, such as a TiO_2 compact layer, require a high temperature (over 400 °C) (Docampo et al., 2013; Roldán-Carmona et al., 2014; Y. Yang et al., 2014). These materials can be deposited at low temperatures (below 150 °C), making them ideal for fabricating flexible solar cells on PET substrates.

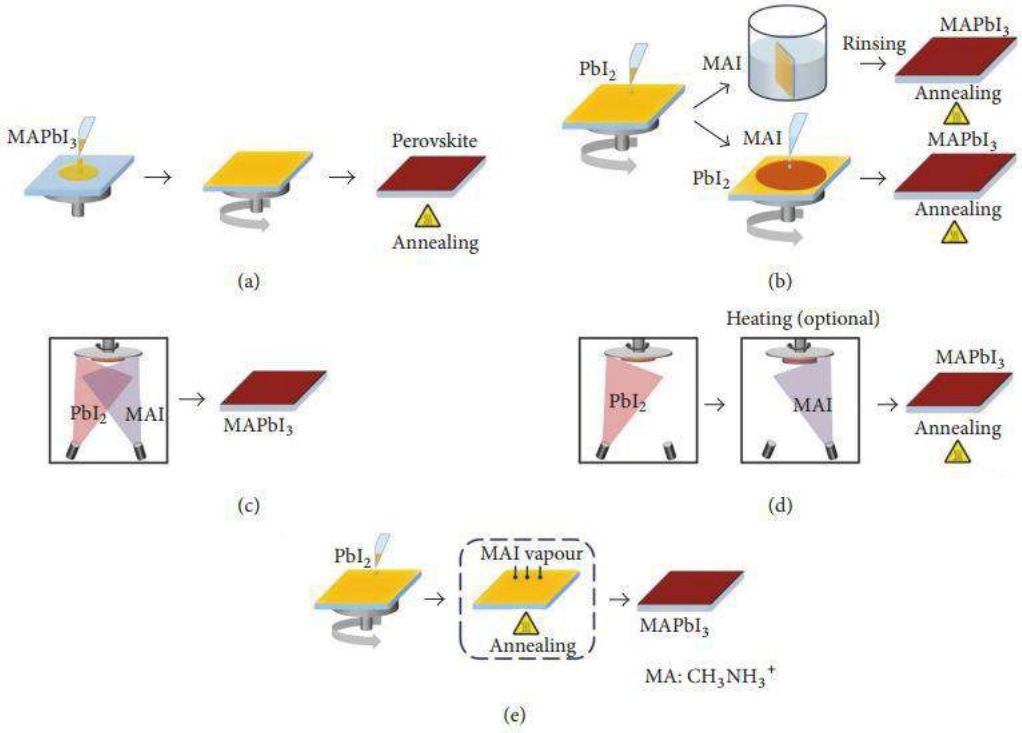

Figure 2.6. Illustration of different deposition methods for perovskite layer (a) solution-based one-step method (b) solution-based two-step method (c) dual-source vapor-deposition method (d) sequential vapor deposition method and (e) vapor-assisted solution method (Djurišić et al., 2017).

Deposition of ZnO ETM at a low temperature also resulted in flexible perovskite solar cells with n-i-p structures (planar structures) (Figure 2.7 (b)) (Bi et al., 2013; H. Zhou et al., 2014). At temperatures lower than 150 degrees Celsius, ZnO nanoparticles have also been deposited. Kelly et al. reported a 10.2% power conversion efficiency (PCE) for an n-i-p structured flexible perovskite solar cell (D. Liu & Kelly, 2013). A TiO_x compact layer formed by atomic layer deposition (ALD) was recently used to produce a high efficiency flexible perovskite solar cell with a PCE of over 12% (B. J. Kim et al., 2015). This solar cell has superior mechanical endurance properties, demonstrating that its energy conversion efficiency does not change after 1000 cycles of bending tests with a bending radius of 10 mm, indicating that flexible perovskite solar cells could be used as a power source for future wearable devices.

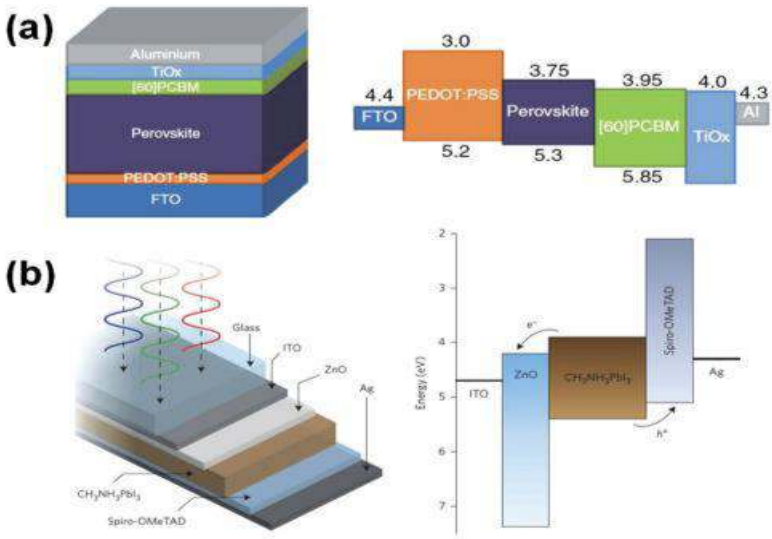

Figure 2.7. (a) A typical p-i-n device configuration and schematic band diagram of the fabricated solar cell and (b) a typical n-i-p device configuration and schematic band diagram of fabricated solar cell (Docampo et al., 2013; Y. Li et al., 2015).

2.6. Pressure Effects on Multilayered Solar Cell Structures

2.6.1. Pressure effects on the optoelectronic properties of PSCs

Pressure, a thermodynamic variable, provides a powerful tool to tune material's structures and properties (M. Li et al., 2020). The soft lattices of perovskites render them sensitive to mechanical compression, which can effectively adjust their atomic and electronic structures, as well as their physical properties, without changing their chemical composition.

The application of external pressure can cause dramatic changes in both the structural and physical properties of perovskites, including the shrinkage and titling of $[BX_6]^{4-}$ octahedra, lattice disordering, bandgap closing, and carrier lifetime modification (C. Zhou et al., 2019). Furthermore, as ions A, B, and X usually have different compressibility, the tolerance factors t changes as a function of the applied pressure, which leads to improved structure and electronic tunability.

PSCs' optoelectronic properties have previously been improved by applying pressure on perovskite films. Pressure application has improved film morphology and charge transport, resulting in increased charge extraction and less charge carrier recombination (Oyelade et al., 2020; Ichwani et al., 2022) Recently, Shi et al applied pressure (400-500 mbar) during the encapsulation of perovskite solar cells and found an improved photovoltaic performance. Recently, Shi et al. applied pressure (400-500 mbar) during the encapsulation of perovskite solar cells and found an improved photovoltaic performance (Bu et al., 2017; Shi et al., 2019). It has been shown from the

XRD pattern, Raman and absorbance spectra that low pressure applied to the perovskite film gives a redshift while high pressure results in a blueshift (Figure 2.8) (Yin et al., 2021).

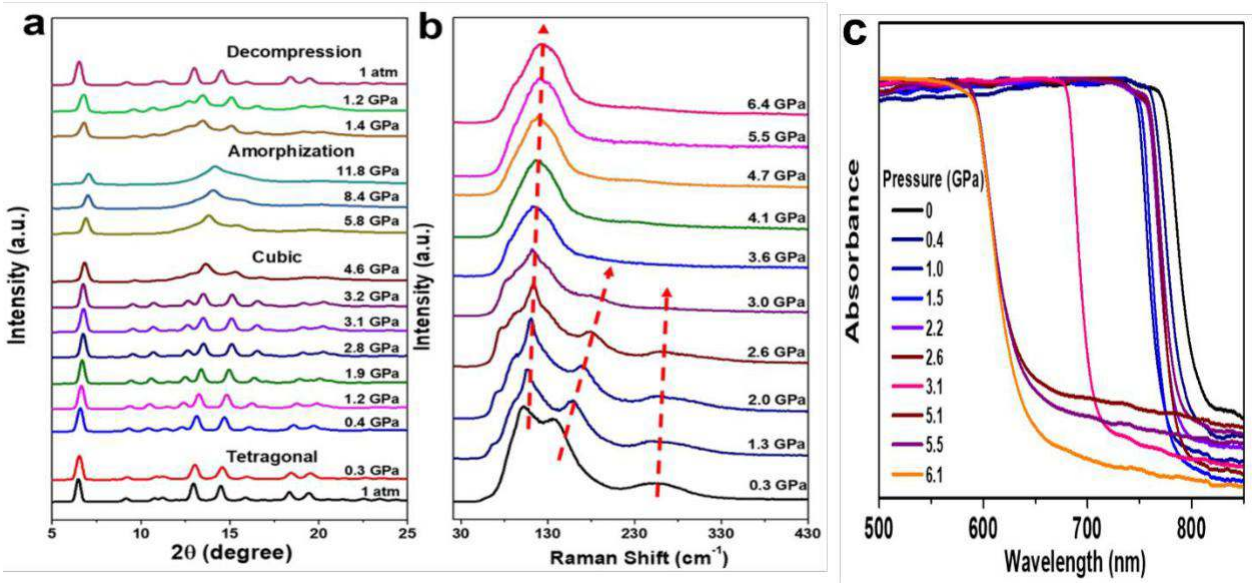

Figure 2.8. XRD patterns of MAPbI3 collected at different pressures up to 11.8 GPa and decompression. (b) Raman spectra of MAPbI3 MCs at different pressures (c) UV-vis absorption spectra of MAPbI3 MCs at different pressures (Yin et al., 2021).

It was also demonstrated that applying pressure to $FAPbI_3$ reduces its bandgap from 1.489 to 1.337 eV and is partially maintained after pressure is released (G. Liu et al., 2017). A gas-flow-induced gas-pumped technique for perovskite films' deposition at pressures up to 1500 Pa was designed with high production efficiencies and PCE of up to 17.03% (Ding et al., 2017).

2.6.2. Effects of pressure on defects

Interfacial and grain boundary defects limit the performance and stability of PSCs (Agyei-Tuffour et al., 2016; Lü et al., 2016; Oyelade et al., 2020). Closing defects can increase charge transport and reduce moisture percolation, both of which damage devices, improving performance and stability. Pressure has been used to close and heal grain boundary defects and interfacial cracks in solar cell structures by increasing the contacts between the layers (Asare et al., 2016; Oyelade et al., 2020). An increase in such contacts can significantly slow the growth of cracks along the device interfaces (Adeniji et al., 2021; Oyelade et al., 2020; Oyewole et al., 2021). It is vital to understand the effect o7f pressure on the layers of organic-inorganic perovskite materials.

The presence of settled particles between layers (Figure 2.9(a)) or surface roughness (Figure 2.9(b)) caused by undissolved particles can cause interfacial and layer defects (Agyei-Tuffour et al., 2017; Akande et al., 2010; O.K. Oyewole et al., 2016; Tong et al., 2015; D. Yu et al., 2014). Improving interfacial surface contact and defects in photoactive material is crucial for highly efficient devices. In prior works, numerous analytical models were employed to study the contact profiles of thin-film interfaces before pressure application (Akande et al., 2010; Oyelade et al., n.d.; J. C. Yu et al., 2015). The top films wrap around the particles when pressure is applied, improving interfacial contact (Figure 2.9(c)).

The deformation of the thin film interfacial particles can be modeled by the displacement of a cantilever beam (Akande et al., 2010; Cao et al., 2014). When the film deflects, the cantilever is brought into contact with the adjacent (bottom) layer. Consequently, the cantilever deflection and interfacial surface contact between adjacent layers provide insights into the formation of interlayer contacts between the adjacent layers of PSCs structures. Interfacial layer contacts are difficult to achieve when the trapped particles between layers are stiff because the void length depends on the

trapped particle's modulus and height (Cao et al., 2014). These rigid particles can sink into the compliant adjacent layers, which can ultimately lead to damage to the device structure. The relationship between the interfacial surface contact (L_c/L) and the applied pressure (P) can be expressed as (Agyei-Tuffour et al., 2016).

(2.10)

where is the interfacial surface contact length, is Young's modulus, is Poisson's ratio, is the film thickness, h is the height of the particle or film surface roughness, is the length of the device structure and is the applied pressure.

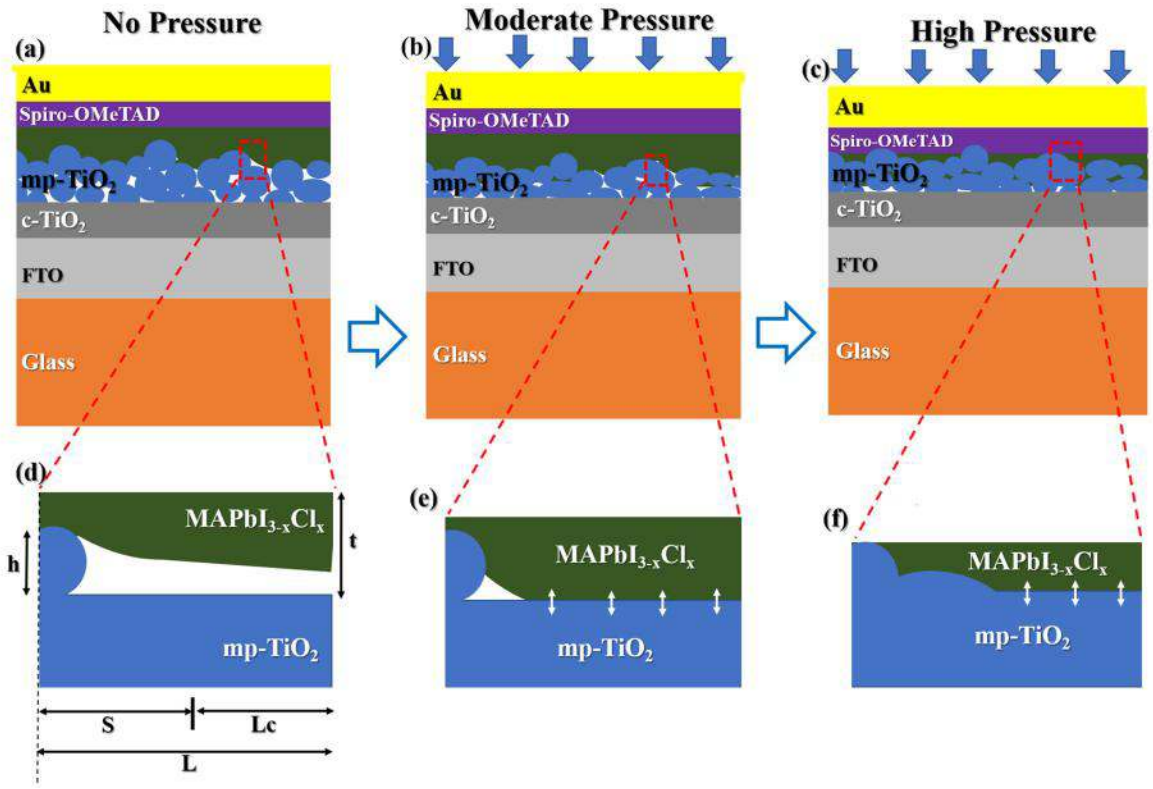

Figure 2.9. Schematics of the interfacial surface contact: (a) no pressure (b) moderate pressure (c) high pressure. Axisymmetric model of the interface surface contact for (d) no pressure case (e) moderate pressure case and (f) high pressure.

2.7. Annealing Effects on the Mechanical Properties of PSCs

Wearable functional devices with great mechanical flexibility and robustness are also feasible with perovskite materials (G. Lee et al., 2019; M. Park et al., 2015). Integration of these materials on flexible and stretchable devices requires knowledge of their mechanical reaction to dynamic strain. Understanding the differences in the mechanical characteristics of perovskite structures produced under various annealing conditions is crucial for device performance and reliability (Olanrewaju et al., 2022; Oyelade et al., 2022; Koech et al., 2021). The temperature at which the perovskite film is annealed influences its structure, morphology, crystallinity, and photoelectric characteristics. Dualeh et al. observed increased surface coverage and better crystallization of perovskite grains when the annealing temperature was increased to a specific value. A solution-based hot casting technique (Dualeh et al., 2014; Nie et al., 2015). It has previously been shown to produce homogeneous, pin-hole-free perovskite grains on the millimeter scale. Huang et al. reported two annealing strategies for tuning perovskite film morphology: one-step direct annealing and multi-step annealing (Huang et al., 2015). In one-step annealing, a single annealing temperature is applied to the precursor, while two-step annealing involves a stepwise ramp annealing procedure to control the evaporation rate of the solvents used in mixing the precursors. Reyes-Martinez et al. determined the time-and rate-dependent mechanical properties of hybrid organic-inorganic and inorganic perovskite (IP) single crystals by monitoring nanoindentation creep and stress relaxation (Reyes-Martinez et al., 2017). Perovskite solar cells have been processed using a variety of thermal annealing temperatures (Dualeh et al., 2014; M. Kim et al.,

2017). It's vital to understand the small-scale mechanical behaviors of these perovskite structures when produced at various annealing temperatures (80^{o}C, 100^{o}C, 130^{o}C, 150 ^{o}C and 170^{o}C) to ascertain mechanical integrity and robustness.

2.8. Fundamentals of Fracture Mechanics in Electronic Systems

Many structures necessitate the usage of perovskite solar cells with flexibility and stretchability. As a result, knowledge of fracture mechanics is critical for developing durable and flexible/stretchable PSCs. This section summarizes some previous research on the fracture mechanics of electronic systems.

2.8.1 Delamination-Induced Buckling and Interfacial Cracking in Stretchable Thin Film Structures

Stretchable electronic devices deform in use, causing failures such as film delamination and interfacial cracking (Asare et al., 2015; O.K. Oyewole et al., 2016; Oluwaseun K. Oyewole, 2015; Wang et al., 2017). Interfacial cracking in a stretchable structure can cause interfacial buckling. Delamination-induced wrinkling can occur in stretchable thin films (Nolte et al., 2017; O K Oyewole et al., 2015; Watanabe, 2012; Wu et al., 2013), under monotonic or cyclic loading. It is critical to understand the mechanisms of delamination-induced wrinkling and cracking during stretchable perovskite solar cell deformation. The delamination of wrinkle thin films can be modeled by assuming a wrinkle thin film on a polymer substrate with a bi-layered structure (Figure 2.12(a)). Exceeding the critical interfacial energy release rates causes the release of pre-stretched films can result in interfacial delamination and cracking of the initially wrinkled films (Figure 2.12(b)).

Delamination (Wu et al., 2013), (Figure 2.12(b)), and other subcritical cracking mechanisms (Figure 2.12(c)) can also occur because of the following deformation of the wrinkled or buckled films before the commencement of unstable crack propagation. If the onset of film buckling coincides with the onset of unstable interfacial crack propagation, then film buckling occurs when buckling tractions result in crack driving forces greater than the adhesion and interfacial fracture energies.

Finite Element Modeling (FEM) could be used to compute the interfacial energy release rates at the tips of the cracks due to delamination-induced buckling of the films, as shown in Figures 2.12 and 2.13. The energy release rate, , caused by film delamination could be calculated as a function of residual strains, , film and substrate thicknesses, and , and Young's moduli,

and , respectively. As a result,

$$= (\quad \_\_ , \_\_ , \_\_ \quad)^{2} \qquad (2.11)$$

where $= /(1 - ^{2})$, $= /(1 - ^{2})$ and d is the half of the interfacial crack between buckled film and substrate (as shown in Figure 2.12 (d-e)).

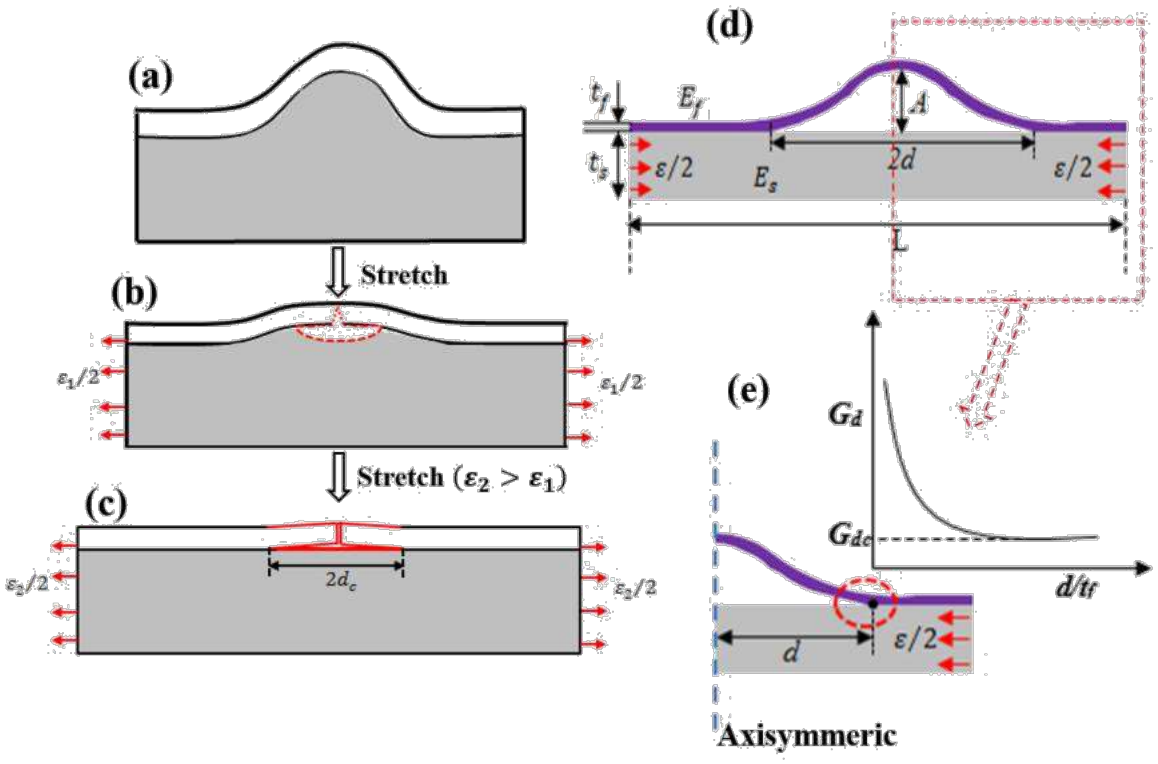

Figure 2.12. Schematics of failure in stretchable solar cell structures: (a) A simple bi-layered structure of wrinkled structure (b) interfacial delamination and initiation of cracking in film upon stretching (c) delamination-induced cracking upon further stretching (d) bi-layered model of interfacial crack driving force and (e) axisymmetric model of the crack driving force

2.8.2. Wrinkling Models for Stretchable Solar Cells

When a thin film is deposited on pre stretched substrates and then released, wrinkled stretchable films are created (Lipomi et al., 2011, 2012). Compressive residual strains caused by temperature mismatch could also cause wrinkling in thin films. Wrinkling of thin films occurs when induced tensions in the film layer reach critical values on flexible or elastic substrates. For stretchable solar cells, the substrate is pre-stretched before the deposition of layered films (Figure 2.13 (a)). Upon release of the substrates, the films wrinkle to form wavy stretchable structures (Figure 2.13 (b)). These wavy stretchable structures are called unstrained solar cells. The critical strains, , required

for the initiation of wrinkling of thin layered films when the substrates are released are given by (Khang et al., 2009; Watanabe, 2012):

$$= [3\ ((1 - {}^{2})/8\ (1 - {}^{2})]^{2/3} \quad (2.12)$$

where and are the Young's moduli of layered film and the substrate, and are the Poisson ratio respectively.

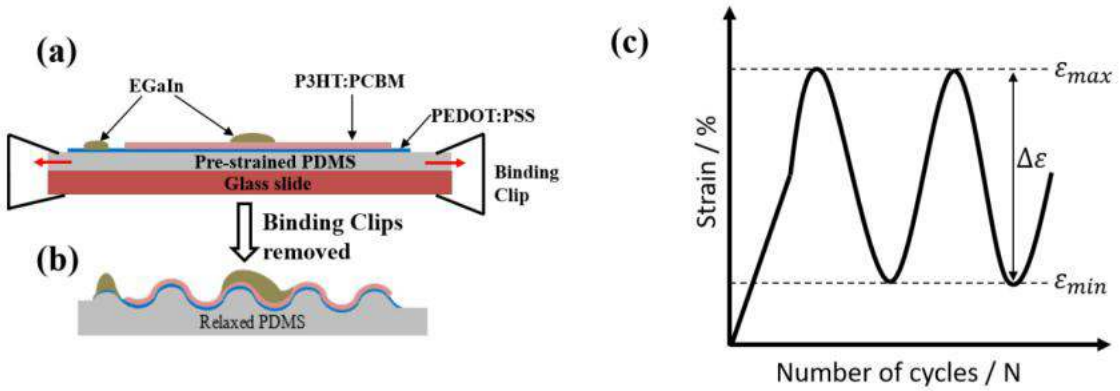

Figure 2.13 (a-b) Schematics of fabrication procedure of layered stretchable solar cells, showing the (a) deposition of different layers on pre-strained PDMS that was clipped on glass substrate (a) and (b) stretchable solar cell upon release of the pre-strained substrate (c) A typical sinusoidal strain-time curve of cyclic deformation of the wrinkled films, showing the maximum ( ) and minimum ( ) strains as well as the strain range (Δ)

2.8.3. Fatigue and Lifetimes of Stretchable Solar Cells

Since stretchable solar cells could be subject to cyclic loading circumstances that can lead to fatigue failure, it is necessary to understand the underlying mechanisms of film deformation and cracking that can lead to stretchable organic solar cell failure. The fatigue lifetimes of multilayer

thin films in stretchable solar cells can be studied using low cycle fatigue (LCF) and high cycle fatigue (HCF) regimes. Figure 2.12c depicts a typical sinusoidal curve for cyclic loading. When thin films are strained after each cycle under the LCF regime, they can deform plastically. Using the Coffin-Manson relationship, the lifetimes of the films are represented as a function of the plastic strain range, p (Kraft et al., 2001; Suresh, n.d.):

$$\frac{\Delta}{} = {}'_{(2)} \quad (2.13)$$

where ′ and are the fatigue ductility coefficient and exponent, while and Δ /2 are the number of cycles to failure and strain amplitude, respectively.

HCF is conducted under stress control. Basquin defined the link between applied stress and the number of cycles to failure as follows:

$$\Delta = {}'( ) \quad (2.14)$$

where Δ is the stress amplitude, ′ is the fatigue strength coefficient and is the fatigue exponent.

2.9. Bending Mechanics

When an external bending motion is applied to devices in a mono-layer system, physical deformation occurs everywhere in the structure. Then, to resist shape deformation, inner stress is created. Because stress can be localized due to the non-uniform position, the stress distribution is heterogeneous throughout the devices. Within the linear elastic range, the elastic modulus, according to Hooke's law, relates stress and strain by a simple ratio (Harris et al., 2016). When a

film-on-substrate model (Figure 2b) is bent into a cylinder of radius R as a mechanical beam, the outer surface experiences tensile strain while the inner surface experiences compressive strain. Inside the device, there is a mechanical neutral plane with no uniaxial strain, and its position is proportional to Young's modulus and layer thickness (Gleskova et al., 1999). Ultra-flexibility is achieved by placing the stiff film on the mechanical neutral plane. Bending mechanics in multilayer structures becomes complicated due to differences in material properties (such as elastic modulus and Poisson's ratio) (S. Il Park et al., 2008). The mismatch between the stiff film and the flexible substrate causes stress to concentrate on the film or the interface between layers. When the obtained stress exceeds the tolerance limit, structures get destroyed (e.g., crack (S. R. Kim & Nairn, 2000; S. Il Park et al., 2008) or delamination (Dai et al., 2015), and their optical and electrical properties deteriorate.

Cracks develop at defect sites of component layers under tensile strain. The film buckles with a large unbonded area under compression strain, and normal and shear stresses can cause the buckle area to grow like a crack. As a result, the bonding strength (adhesion) is proportional to the compression strain endurance. The strain in the convex surface is equal to the distance from the neutral plane divided by (Suo et al., 1999)

$$= \quad - \tag{2.15}$$

Thin film undergoes low bending strain at a given bending radius , as stated in Equation (2.15), and maintains its function at a low critical bending radius. The distance between the outer surface and the mechanical neutral plane can be calculated as follows:

$$= \quad \frac{}{2} + \frac{(1+2 + \ ^2)}{(1+)(1+)} \tag{2.16}$$

where the subscripts " " and " " denote the film and substrate, respectively; = / , where and denote the thickness of the film and substrate, respectively; = / , where and denote the Young's modulus of the film and substrate, respectively.

Therefore, the strain in convex surface can be described as:

$$= \frac{+}{2}\frac{(1+2 + {}^{2})}{(1+)(1+)} \quad (2.17)$$

When the film and substrate have similar elastic moduli, that is ≈ , ≈ 1, the position of neutral plane coincides with the midplane of device, Equation (2.16) can be simplified as

$$= \frac{+}{2} \quad (2.18)$$

and Equation (2.17) becomes

$$= \frac{+}{2} \quad (2.19)$$

In a complicated multilayer structure, the component layers can be modeled as a composite beam subject to a bending curvature. The distance is given by (D. H. Kim et al., 2008; S. Il Park et al., 2009, 2010)

$$= \frac{\Sigma \quad h](\Sigma \quad h)- \quad]}{} \quad (2.20)$$

where is the total number of layers; h is the thickness of the h layer; when the devices are narrow —is equal to the Young's modulus of each layer; when the biaxial deformation should be

considered, is equal to the plane strain modulus = $(1 - {}^{2})$ where and denote the Young's modulus and the Poisson's ratio of the h layer, respectively.

2.10. References

Adeniji, S. A., Cromwell, J., Oyewole, D. O., Oyelade, O. V., Koech, R. K., Sanni, D. M., Oyewole, O. K., Babatope, B., & Soboyejo, W. O. (2021). Pressure-assisted fabrication of perovskite light emitting devices. *AIP Advances*, *11*(2), 025112. https://doi.org/10.1063/5.0035953

Adeniji, S., Oyewole, O., Koech, R., Oyewole, D., Cromwell, J., Ahmed, R., Oyelade, O., Sanni, D., Orisekeh, K., Bello, A., & Soboyejo, W. (2021). Failure Mechanisms of Stretchable Perovskite Light-Emitting Devices under Monotonic and Cyclic Deformations. *Macromolecular Materials and Engineering*, *306*(11), 2100435.

Agyei-Tuffour, B., Doumon, N. Y., Rwenyagila, E. R., Asare, J., Oyewole, O. K., Shen, Z., Petoukhoff, C. E., Zebaze Kana, M. G., Ocarroll, D. M., & Soboyejo, W. O. (2017). Pressure effects on interfacial surface contacts and performance of organic solar cells. *Journal of Applied Physics*, *122*(20). https://doi.org/10.1063/1.5001765

Agyei-Tuffour, B., Rwenyagila, E. R., Asare, J., Oyewole, O. K., Zebaze Kana, M. G., O'Carroll, D. M., & Soboyejo, W. O. (2016). Influence of Pressure on Contacts between Layers in Organic Photovoltaic Cells. *Advanced Materials Research*, *1132*, 204–216. https://doi.org/10.4028/WWW.SCIENTIFIC.NET/AMR.1132.204

Aharon, S., Gamliel, S., Cohen, B. El, & Etgar, L. (2014). Depletion region effect of highly

efficient hole conductor free CH3NH3PbI3 perovskite solar cells. *Physical Chemistry Chemical Physics*, *16*(22), 10512–10518. https://doi.org/10.1039/C4CP00460D

Akande, W. O., Cao, Y., Yao, N., & Soboyejo, W. (2010). Adhesion and the cold welding of gold-silver thin films. *Journal of Applied Physics*, *107*(4), 043519. https://doi.org/10.1063/1.3305791

Asare, J., Agyei-Tuffour, B., Oyewole, O. K., Anye, V. C., Momodu, D. Y., Zebaze-Kana, G. M., & Soboyejo, W. O. (2015). Effects of Deformation on Failure Mechanisms and Optical Properties of Flexible Organic Solar Cell Structures. *Advanced Materials Research*, *1132*, 125–143.

Barnett, J. L., Cherrette, V. L., Hutcherson, C. J., & So, M. C. (2016). Effects of Solution-Based Fabrication Conditions on Morphology of Lead Halide Perovskite Thin Film Solar Cells. *Advances in Materials Science and Engineering*, *2016*. https://doi.org/10.1155/2016/4126163

Best Research-Cell Efficiency Chart | Enhanced Reader. (n.d.). Retrieved October 1, 2021, from moz-extension://59238ff8-d379-460e-a75f-f63264ca7971/enhanced-reader.html?openApp&pdf=https%3A%2F%2Fwww.nrel.gov%2Fpv%2Fassets%2Fpdfs%2Fbest-research-cell-efficiencies.20190802.pdf

Bi, D., Moon, S. J., Häggman, L., Boschloo, G., Yang, L., Johansson, E. M. J., Nazeeruddin, M. K., Grätzel, M., & Hagfeldt, A. (2013). Using a two-step deposition technique to prepare perovskite (CH3NH3PbI3) for thin film solar cells based on ZrO2 and TiO2 mesostructures. *RSC Advances*, *3*(41), 18762–18766. https://doi.org/10.1039/C3RA43228A

Bu, T., Wu, L., Liu, X., Yang, X., Zhou, P., Yu, X., Qin, T., Shi, J., Wang, S., Li, S., Ku, Z., Peng,

Y., Huang, F., Meng, Q., Cheng, B., & Zhong, J. (2017). *Synergic Interface Optimization with Green Solvent Engineering in Mixed Perovskite Solar Cells*. https://doi.org/10.1002/aenm.201700576

Burschka, J., Pellet, N., Moon, S. J., Humphry-Baker, R., Gao, P., Nazeeruddin, M. K., & Grätzel, M. (2013). Sequential deposition as a route to high-performance perovskite-sensitized solar cells. *Nature 2013 499:7458*, *499*(7458), 316–319. https://doi.org/10.1038/nature12340

Cao, Y., Kim, C., Forrest, S. R., Soboyejo, W., Cao, Y., Kim, C., & Forrest, S. R. (2014). *Effects of dust particles and layer properties on organic electronic devices fabricated by stamping Effects of dust particles and layer properties on organic electronic devices*. *033713*(2005). https://doi.org/10.1063/1.1994935

Chen, C.-W., Kang, H.-W., Hsiao, S.-Y., Yang, P.-F., Chiang, K.-M., & Lin, H.-W. (2014). Efficient and Uniform Planar-Type Perovskite Solar Cells by Simple Sequential Vacuum Deposition. *Advanced Materials*, *26*(38), 6647–6652. https://doi.org/10.1002/ADMA.201402461

Chen, Q., Zhou, H., Hong, Z., Luo, S., Duan, H. S., Wang, H. H., Liu, Y., Li, G., & Yang, Y. (2014). Planar heterojunction perovskite solar cells via vapor-assisted solution process. *Journal of the American Chemical Society*, *136*(2), 622–625. https://doi.org/10.1021/JA411509G/SUPPL_FILE/JA411509G_SI_001.PDF

Conings, B., Baeten, L., Jacobs, T., Dera, R., D'Haen, J., Manca, J., & Boyen, H.-G. (2014). An easy-to-fabricate low-temperature TiO2 electron collection layer for high efficiency planar heterojunction perovskite solar cells. *APL Materials*, *2*(8), 081505. https://doi.org/10.1063/1.4890245

Correa-Baena, J.-P., Abate, A., Saliba, M., Tress, W., Jacobsson, T. J., Grätzel, M., & Hagfeldt, A. (2017). The rapid evolution of highly efficient perovskite solar cells. *Energy & Environmental Science*, *10*(3), 710–727. https://doi.org/10.1039/C6EE03397K

Da, P., & Zheng, G. (2017). Tailoring interface of lead-halide perovskite solar cells. *Undefined*, *10*(5), 1471–1497. https://doi.org/10.1007/S12274-016-1405-2

Dai, L., Huang, Y., Chen, H., Feng, X., & Fang, D. (2015). Transition among failure modes of the bending system with a stiff film on a soft substrate. *Applied Physics Letters*, *106*(2), 021905. https://doi.org/10.1063/1.4905697

DB, M., S, W., CA, F., CA, C., & AM, G. (1995). Conducting Layered Organic-inorganic Halides Containing -Oriented Perovskite Sheets. *Science (New York, N.Y.)*, *267*(5203), 1473–1476. https://doi.org/10.1126/SCIENCE.267.5203.1473

Ding, B., Li, Y., Huang, S. Y., Chu, Q. Q., Li, C. X., Li, C. J., & Yang, G. J. (2017). Material nucleation/growth competition tuning towards highly reproducible planar perovskite solar cells with efficiency exceeding 20%. *Journal of Materials Chemistry A*, *5*(15), 6840–6848. https://doi.org/10.1039/C7TA00027H

Djurišić, A. B., Liu, F. Z., Tam, H. W., Wong, M. K., Ng, A., Surya, C., Chen, W., & He, Z. B. (2017). Perovskite solar cells - An overview of critical issues. *Progress in Quantum Electronics*, *53*, 1–37. https://doi.org/10.1016/J.PQUANTELEC.2017.05.002

Docampo, P., Ball, J. M., Darwich, M., Eperon, G. E., & Snaith, H. J. (2013). Efficient organometal trihalide perovskite planar-heterojunction solar cells on flexible polymer substrates. *Nature Communications 2013 4:1*, *4*(1), 1–6. https://doi.org/10.1038/ncomms3761

Dualeh, A., Tétreault, N., Moehl, T., Gao, P., Nazeeruddin, M. K., & Grätzel, M. (2014). *Effect of Annealing Temperature on Film Morphology of Organic – Inorganic Hybrid Pervoskite Solid-State Solar Cells*. https://doi.org/10.1002/adfm.201304022

Forgács, D., Gil-Escrig, L., Pérez-Del-Rey, D., Momblona, C., Werner, J., Niesen, B., Ballif, C., Sessolo, M., Bolink D Forgács, H. J., Gil-Escrig, L., Pérez-Del-Rey, D., Momblona, C., Sessolo, M., Bolink, H. J., Werner, J., Niesen, B., & Ballif, C. (2017). Efficient Monolithic Perovskite/Perovskite Tandem Solar Cells. *Advanced Energy Materials*, *7*(8), 1602121. https://doi.org/10.1002/AENM.201602121

Gleskova, H., Wagner, S., & Suo, Z. (1999). Failure resistance of amorphous silicon transistors under extreme in-plane strain. *Applied Physics Letters*, *75*(19), 3011. https://doi.org/10.1063/1.125174

Green, M. A., Dunlop, E. D., Hohl-Ebinger, J., Yoshita, M., Kopidakis, N., & Ho-Baillie, A. W. Y. (2020). Solar cell efficiency tables (Version 55). *Progress in Photovoltaics: Research and Applications*, *28*(1), 3–15. https://doi.org/10.1002/PIP.3228

Green, M. A., Ho-Baillie, A., & Snaith, H. J. (2014). The emergence of perovskite solar cells. *Nature Photonics 2014 8:7*, *8*(7), 506–514. https://doi.org/10.1038/nphoton.2014.134

Harris, K. D., Elias, A. L., & Chung, H. J. (2016). Flexible electronics under strain: a review of mechanical characterization and durability enhancement strategies. *Journal of Materials Science*, *51*(6), 2771–2805. https://doi.org/10.1007/s10853-015-9643-3

Heo, J. H., Im, S. H., Noh, J. H., Mandal, T. N., Lim, C.-S., Chang, J. A., Lee, Y. H., Kim, H.-J., Sarkar, A., Nazeeruddin, M. K., Grätzel, M., & Seok, S. Il. (2013). Efficient inorganic-organic hybrid heterojunction solar cells containing perovskite compound and polymeric hole

conductors. *NaPho*, *7*(6), 486–491. https://doi.org/10.1038/NPHOTON.2013.80

Huang, L., Hu, Z., Xu, J., Zhang, K., Zhang, J., & Zhu, Y. (2015). Multi-step slow annealing perovskite films for high performance planar perovskite solar cells. *Solar Energy Materials and Solar Cells*, *141*, 377–382. https://doi.org/10.1016/J.SOLMAT.2015.06.018

Ichwani, R., Koech, R., Oyewole, O. K., Huda, A., Oyewole, D. O., Cromwell, J., Martin, J. L., Grimm, R. L., & Soboyejo, W. O. (2022). Interfacial fracture of hybrid organic–inorganic perovskite solar cells. *Extreme Mechanics Letters*, *50*, 101515. https://doi.org/10.1016/J.EML.2021.101515

Jacobsson, T. J., Correa-Baena, J.-P., Pazoki, M., Saliba, M., Schenk, K., Grätzel, M., & Hagfeldt, A. (2016). Exploration of the compositional space for mixed lead halogen perovskites for high efficiency solar cells. *Energy & Environmental Science*, *9*(5), 1706–1724. https://doi.org/10.1039/C6EE00030D

Jain, A., Castelli, I. E., Hautier, G., Bailey, D. H., & Jacobsen, K. W. (2013). Performance of genetic algorithms in search for water splitting perovskites. *Journal of Materials Science*, *48*(19), 6519–6534. https://doi.org/10.1007/S10853-013-7448-9

Jeon, N. J., Noh, J. H., Yang, W. S., Kim, Y. C., Ryu, S., Seo, J., & Seok, S. Il. (2015). Compositional engineering of perovskite materials for high-performance solar cells. *Nature 2015 517:7535*, *517*(7535), 476–480. https://doi.org/10.1038/nature14133

Kaltenbrunner, M., Adam, G., Głowacki, E. D., Drack, M., Schwödiauer, R., Leonat, L., Apaydin, D. H., Groiss, H., Scharber, M. C., White, M. S., Sariciftci, N. S., & Bauer, S. (2015). Flexible high power-per-weight perovskite solar cells with chromium oxide-metal contacts for improved stability in air. *Nature Materials*, *14*(10), 1032–1039.

https://doi.org/10.1038/nmat4388

Khang, D. Y., Rogers, J. A., & Lee, H. H. (2009). Mechanical buckling: Mechanics, metrology, and stretchable electronics. *Advanced Functional Materials*, *19*(10), 1526–1536. https://doi.org/10.1002/ADFM.200801065

Kim, B. J., Kim, D. H., Lee, Y. Y., Shin, H. W., Han, G. S., Hong, J. S., Mahmood, K., Ahn, T. K., Joo, Y. C., Hong, K. S., Park, N. G., Lee, S., & Jung, H. S. (2015). Highly efficient and bending durable perovskite solar cells: Toward a wearable power source. *Energy and Environmental Science*, *8*(3). https://doi.org/10.1039/c4ee02441a

Kim, D. H., Ahn, J. H., Won, M. C., Kim, H. S., Kim, T. H., Song, J., Huang, Y. Y., Liu, Z., Lu, C., & Rogers, J. A. (2008). Stretchable and foldable silicon integrated circuits. *Science (New York, N.Y.)*, *320*(5875), 507–511. https://doi.org/10.1126/SCIENCE.1154367

Kim, H.-S., Im, S. H., & Park, N.-G. (2014). Organolead Halide Perovskite: New Horizons in Solar Cell Research. *Journal of Physical Chemistry C*, *118*(11), 5615–5625. https://doi.org/10.1021/JP409025W

Kim, M., Kim, G.-H., Oh, K. S., Jo, Y., Yoon, H., Kim, K.-H., Lee, H., Kim, J. Y., & Kim, D. S. (2017). High-Temperature–Short-Time Annealing Process for High-Performance Large-Area Perovskite Solar Cells. *ACS Nano*, *11*(6), 6057–6064. https://doi.org/10.1021/ACSNANO.7B02015

Kim, S. R., & Nairn, J. A. (2000). Fracture mechanics analysis of coating/substrate systems: Part I: Analysis of tensile and bending experiments. *Engineering Fracture Mechanics*, *65*(5), 573–593. https://doi.org/10.1016/S0013-7944(99)00141-1

Koech, R. K., Ichwani, R., Martin, J. L., Oyewole, D. O., Oyelade, O. V., Olanrewaju, Y. A., Sanni, D. M., Adeniji, S. A., Grimm, R. L., Bello, A., Oyewole, O. K., Ntsoenzok, E., & Soboyejo, W. O. (2021). A study of the effects of a thermally evaporated nanoscale CsBr layer on the optoelectronic properties and stability of formamidinium-rich perovskite solar cells. *AIP Advances*, *11*(9), 095112. https://doi.org/10.1063/5.0064398

Kraft, O., Schwaiger, R., & Wellner, P. (2001). Fatigue in thin films: Lifetime and damage formation. *Materials Science and Engineering A*, *319–321*, 919–923. https://doi.org/10.1016/S0921-5093(01)00990-X

Krishnamoorthy, T., Ding, H., Yan, C., Leong, W. L., Baikie, T., Zhang, Z., Sherburne, M., Li, S., Asta, M., Mathews, N., & Mhaisalkar, S. G. (2015). Lead-free germanium iodide perovskite materials for photovoltaic applications. *Journal of Materials Chemistry A*, *3*(47), 23829– 23832. https://doi.org/10.1039/C5TA05741H

Lee, G., Kim, M., Choi, Y. W., Ahn, N., Jang, J., Yoon, J., Kim, S. M., Lee, J.-G., Kang, D., Jung, H. S., & Choi, M. (2019). Ultra-flexible perovskite solar cells with crumpling durability: toward a wearable power source. *Energy & Environmental Science*, *12*(10), 3182–3191. https://doi.org/10.1039/C9EE01944H

Lee, J.-W., Kim, D.-H., Kim, H.-S., Seo, S.-W., Cho, S. M., & Park, N.-G. (2015). Formamidinium and Cesium Hybridization for Photo- and Moisture-Stable Perovskite Solar Cell. *Advanced Energy Materials*, *5*(20), 1501310. https://doi.org/10.1002/AENM.201501310

Lee, J. W., Seol, D. J., Cho, A. N., & Park, N. G. (2014). High-efficiency perovskite solar cells based on the black polymorph of HC(NH2)2PbI3. *Advanced Materials*, *26*(29), 4991–4998. https://doi.org/10.1002/ADMA.201401137

Lee, M. M., Teuscher, J., Miyasaka, T., Murakami, T. N., & Snaith, H. J. (2012). Efficient hybrid solar cells based on meso-superstructured organometal halide perovskites. *Science (New York, N.Y.)*, *338*(6107), 643–647. https://doi.org/10.1126/SCIENCE.1228604

Li, C., Lu, X., Ding, W., Feng, L., Gao, Y., & Guo, Z. (2008). Formability of ABX 3 (X = F, Cl, Br, I) halide perovskites. *Acta Crystallographica Section B: Structural Science*, *64*(6), 702–707. https://doi.org/10.1107/S0108768108032734

Li, L., Zhang, F., Hao, Y., Sun, Q., Li, Z., Wang, H., Cui, Y., & Zhu, F. (2017). High efficiency planar Sn–Pb binary perovskite solar cells: controlled growth of large grains via a one-step solution fabrication process. *Journal of Materials Chemistry C*, *5*(9), 2360–2367. https://doi.org/10.1039/C6TC05325D

Li, M., Liu, T., Wang, Y., Yang, W., & Lü, X. (2020). Pressure responses of halide perovskites with various compositions, dimensionalities, and morphologies. *Matter and Radiation at Extremes*, *5*(1), 018201. https://doi.org/10.1063/1.5133653

Li, Y., Cooper, J. K., Giannini, C., Liu, Y., Toma, F. M., & Sharp, I. D. (2015). *Fabrication of Planar Heterojunction Perovskite Solar Cells by Controlled Low-Pressure Vapor Annealing*. https://doi.org/10.1021/jz502720a

Liang, K., Mitzi, D. B., & Prikas, M. T. (1998). Synthesis and Characterization of Organic−Inorganic Perovskite Thin Films Prepared Using a Versatile Two-Step Dipping Technique. *Chemistry of Materials*, *10*(1), 403–411. https://doi.org/10.1021/CM970568F

Lipomi, D. J., & Bao, Z. (2011). Stretchable, elastic materials and devices for solar energy conversion. *Energy & Environmental Science*, *4*(9), 3314–3328. https://doi.org/10.1039/C1EE01881G

Lipomi, D. J., Lee, J. A., Vosgueritchian, M., Tee, B. C. K., Bolander, J. A., & Bao, Z. (2012). Electronic properties of transparent conductive films of PEDOT:PSS on stretchable substrates. *Chemistry of Materials*, *24*(2), 373–382. https://doi.org/10.1021/CM203216M/SUPPL_FILE/CM203216M_SI_001.PDF

Lipomi, D. J., Tee, B. C.-K., Vosgueritchian, M., & Bao, Z. (2011). Switchable Wettability: Stretchable Organic Solar Cells (Adv. Mater. 15/2011). *Advanced Materials*, *23*(15), 1770–1770. https://doi.org/10.1002/ADMA.201190054

Liu, C., Fan, J., Li, H., Zhang, C., & Mai, Y. (2016). Highly Efficient Perovskite Solar Cells with Substantial Reduction of Lead Content. *Scientific Reports 2016 6:1*, *6*(1), 1–8. https://doi.org/10.1038/srep35705

Liu, D., & Kelly, T. L. (2013). Perovskite solar cells with a planar heterojunction structure prepared using room-temperature solution processing techniques. *Nature Photonics 2013 8:2*, *8*(2), 133–138. https://doi.org/10.1038/nphoton.2013.342

Liu, G., Kong, L., Gong, J., Yang, W., Mao, H. K., Hu, Q., Liu, Z., Schaller, R. D., Zhang, D., & Xu, T. (2017). Pressure-Induced Bandgap Optimization in Lead-Based Perovskites with Prolonged Carrier Lifetime and Ambient Retainability. *Advanced Functional Materials*, *27*(3), 1604208. https://doi.org/10.1002/ADFM.201604208

Liu, M., Johnston, M. B., & Snaith, H. J. (2013). Efficient planar heterojunction perovskite solar cells by vapour deposition. *Nature*, *501*(7467), 395–398. https://doi.org/10.1038/NATURE12509

Lü, X., Wang, Y., Stoumpos, C. C., Hu, Q., Guo, X., Chen, H., Yang, L., Smith, J. S., Yang, W., Zhao, Y., Xu, H., Kanatzidis, M. G., & Jia, Q. (2016). *Enhanced Structural Stability and*

Photo Responsiveness of CH 3 NH 3 SnI 3 Perovskite via Pressure-Induced Amorphization and Recrystallization. 3–8. https://doi.org/10.1002/adma.201600771

M, G. (2014). The light and shade of perovskite solar cells. *Nature Materials*, *13*(9), 838–842. https://doi.org/10.1038/NMAT4065

Mahmood, K., Sarwar, S., & Mehran, M. T. (2017). Current status of electron transport layers in perovskite solar cells: materials and properties. *RSC Advances*, *7*(28), 17044–17062. https://doi.org/10.1039/C7RA00002B

Mei, A., Li, X., Liu, L., Ku, Z., Liu, T., Rong, Y., Xu, M., Hu, M., Chen, J., Yang, Y., Grätzel, M., & Han, H. (2014). A hole-conductor–free, fully printable mesoscopic perovskite solar cell with high stability. *Science*, *345*(6194), 295–298. https://doi.org/10.1126/SCIENCE.1254763

Miyata, A., Mitioglu, A., Plochocka, P., Portugall, O., Tse-Wei Wang, J., Stranks, S. D., Snaith, H. J., & Nicholas, R. J. (2015). Direct measurement of the exciton binding energy and effective masses for charge carriers in organic–inorganic tri-halide perovskites. *NATURE PHYSICS* |, *11*. https://doi.org/10.1038/NPHYS3357

Nie, W., Tsai, H., Asadpour, R., Blancon, J. C., Neukirch, A. J., Gupta, G., Crochet, J. J., Chhowalla, M., Tretiak, S., Alam, M. A., Wang, H. L., & Mohite, A. D. (2015). High-efficiency solution-processed perovskite solar cells with millimeter-scale grains. *Science*, *347*(6221), 522–525. https://doi.org/10.1126/SCIENCE.AAA0472/SUPPL_FILE/NIE.SM.PDF

Noel, N. K., Stranks, S. D., Abate, A., Wehrenfennig, C., Guarnera, S., Haghighirad, A.-A., Sadhanala, A., Eperon, G. E., Pathak, S. K., Johnston, M. B., Petrozza, A., Herz, L. M., &

Snaith, H. J. (2014). Lead-free organic–inorganic tin halide perovskites for photovoltaic applications. *Energy & Environmental Science*, *7*(9), 3061–3068. https://doi.org/10.1039/C4EE01076K

Nolte, A. J., Young Chung, J., Davis, C. S., & Stafford, C. M. (2017). Wrinkling-to-delamination transition in thin polymer films on compliant substrates. *Soft Matter*, *13*(43), 7930. https://doi.org/10.1039/C7SM01472D

Olanrewaju, Y. A., Orisekeh, K., Oyelade, O. V., Koech, R. K., Ichwani, R., Ebunu, A. I., Amune, D. I., Bello, A., Anye, V. C., Oyewole, O. K., & Soboyejo, W. O. (2022). Effects of temperature-dependent burn-in decay on the performance of triple cation mixed halide perovskite solar cells. *AIP Advances*, *12*(1), 015122. https://doi.org/10.1063/5.0078821

Oyelade, O. V., Oyewole, O. K., Olanrewaju, Y. A., Ichwani, R., Koech, R., Oyewole, D. O., Adeniji, S. A., Sanni, D. M., Cromwell, J., Ahmed, R. A., Orisekeh, K., Anye, V. C., & Soboyejo, W. O. (2022) Understanding the effects of annealing temperature on the Mechanical properties of layers in FAI-rich perovskite solar cells *AIP Advances 12 (2) 25104*

Oyelade, O. V., Oyewole, O. K., Oyewole, D. O., Adeniji, S. A., Ichwani, R., Sanni, D. M., & Soboyejo, W. O. (2020). Pressure-Assisted Fabrication of Perovskite Solar Cells. *Scientific Reports 2020 10:1*, *10*(1), 1–11. https://doi.org/10.1038/s41598-020-64090-5

Oyewole, D. O., Oyewole, O. K., Kushnir, K., Shi, T., Oyelade, O. V., Adeniji, S. A., Agyei-Tuffour, B., Evans-Lutterodt, K., Titova, L. V., & Soboyejo, W. O. (2021). Pressure and thermal annealing effects on the photoconversion efficiency of polymer solar cells. *AIP*

Advances, *11*(4). https://doi.org/10.1063/5.0045694

Oyewole, O.K., Asare, J., Oyewole, D. O., Agyei-Tuffour, B., Anye, V. C., Zebaze Kana, M. G., & Soboyejo, W. O. (2016). Effects of Adhesion and Stretching on Failure Mechanisms and Optical Properties of Organic Solar Cells. *Advanced Materials Research*, *1132*, 89–105. https://doi.org/10.4028/WWW.SCIENTIFIC.NET/AMR.1132.89

Oyewole, O K, Yu, D., Du, J., Asare, J., Oyewole, D. O., Anye, V. C., Fashina, A., Zebaze Kana, M. G., & Soboyejo, W. O. (2015). Micro-wrinkling and delamination-induced buckling of stretchable electronic structures. *Journal of Applied Physics*, *117*(23), 235501.

Oyewole, Oluwaseun K. (2015). Effects of Adhesion and Deformation on Stretchable Electronic Structures. In *Phd Thesis submitted to African University of Science and Technology*.

Park, S. Il, Ahn, J. H., Feng, X., Wang, S., Huang, Y., & Rogers, J. A. (2008). Theoretical and Experimental Studies of Bending of Inorganic Electronic Materials on Plastic Substrates. *Advanced Functional Materials*, *18*(18), 2673–2684. https://doi.org/10.1002/ADFM.200800306

Park, S. Il, Le, A. P., Wu, J., Huang, Y., Li, X., & Rogers, J. A. (2010). Light emission characteristics and mechanics of foldable inorganic light-emitting diodes. *Advanced Materials (Deerfield Beach, Fla.)*, *22*(28), 3062–3066. https://doi.org/10.1002/ADMA.201000591

Park, S. Il, Xiong, Y., Kim, R. H., Elvikis, P., Meitl, M., Kim, D. H., Wu, J., Yoon, J., Chang-Jae, Y., Liu, Z., Huang, Y., Hwang, K. C., Ferreira, P., Xiuling, L., Choquette, K., & Rogers, J. A. (2009). Printed assemblies of inorganic light-emitting diodes for deformable and semitransparent displays. *Science*, *325*(5943), 977–981.

https://doi.org/10.1126/science.1175690

Park, M., Kim, H. J., Jeong, I., Lee, J., Lee, H., Son, H. J., Kim, D.-E., & Ko, M. J. (2015). Mechanically Recoverable and Highly Efficient Perovskite Solar Cells: Investigation of Intrinsic Flexibility of Organic–Inorganic Perovskite. *Advanced Energy Materials*, *5*(22), 1501406. https://doi.org/10.1002/AENM.201501406

Qian, J., Xu, B., & Tian, W. (2016). A comprehensive theoretical study of halide perovskites ABX3. *Organic Electronics*, *C* (37), 61–73. https://doi.org/10.1016/J.ORGEL.2016.05.046

Reyes-Martinez, M. A., Abdelhady, A. L., Saidaminov, M. I., Chung, D. Y., Bakr, O. M., Kanatzidis, M. G., Soboyejo, W. O., & Loo, Y.-L. (2017). Time-Dependent Mechanical Response of APbX3 (A = Cs, CH3NH3; X = I, Br) Single Crystals. *Advanced Materials*, *29*(24), 1606556. https://doi.org/10.1002/ADMA.201606556

Rodrigues, E. M. G., Melício, R., Mendes, V. M. F., & Catalão, J. P. S. (n.d.). *Simulation of a Solar Cell considering Single-Diode Equivalent Circuit Model*. https://doi.org/10.24084/repqj09.339

Roldán-Carmona, C., Malinkiewicz, O., Soriano, A., Mínguez Espallargas, G., Garcia, A., Reinecke, P., Kroyer, T., Dar, M. I., Nazeeruddin, M. K., & Bolink, H. J. (2014). Flexible high efficiency perovskite solar cells. *Energy & Environmental Science*, *7*(3), 994–997. https://doi.org/10.1039/C3EE43619E

Roy, P., Kumar Sinha, N., Tiwari, S., & Khare, A. (2020). A review on perovskite solar cells: Evolution of architecture, fabrication techniques, commercialization issues and status. *Solar Energy*, *198*, 665–688. https://doi.org/10.1016/J.SOLENER.2020.01.080

Sarukura, N., Murakami, H., Estacio, E., Ono, S., El Ouenzerfi, R., Cadatal, M., Nishimatsu, T., Terakubo, N., Mizuseki, H., Kawazoe, Y., Yoshikawa, A., & Fukuda, T. (2007). Proposed design principle of fluoride-based materials for deep ultraviolet light emitting devices. *Optical Materials*, *1*(30), 15–17. https://doi.org/10.1016/J.OPTMAT.2006.11.031

Shi, L., Zhang, M., Cho, Y., Young, T. L., Wang, D., Yi, H., Kim, J., Huang, S., & Ho-Baillie, A. W. Y. (2019). Effect of Pressing Pressure on the Performance of Perovskite Solar Cells. *ACS Applied Energy Materials*, *2*(4), 2358–2363. https://doi.org/10.1021/ACSAEM.8B01608/SUPPL_FILE/AE8B01608_SI_001.PDF

Song, Z., Watthage, S. C., Phillips, A. B., & Heben, M. J. (2016). Pathways toward high-performance perovskite solar cells: review of recent advances in organo-metal halide perovskites for photovoltaic applications. *Journal of Photonics for Energy*, *6*(2), 022001. https://doi.org/10.1117/1.JPE.6.022001

Suarez, B., Gonzalez-Pedro, V., Ripolles, T. S., Sanchez, R. S., Otero, L., & Mora-Sero, I. (2014). Recombination Study of Combined Halides (Cl, Br, I) Perovskite Solar Cells. *Journal of Physical Chemistry Letters*, *5*(10), 1628–1635. https://doi.org/10.1021/JZ5006797

Suo, Z., Ma, E. Y., Gleskova, H., & Wagner, S. (1999). Mechanics of rollable and foldable film-on-foil electronics. *Applied Physics Letters*, *74*(8), 1177. https://doi.org/10.1063/1.123478

Suresh, S. (n.d.). *Fatigue of Materials (Cambridge Solid State Science Series) Second Edition by S. Suresh*. Retrieved January 2, 2022, from https://www.amazon.com/Fatigue-Materials-Cambridge-Science-Second/dp/0521578477

Tong, T., Babatope, B., Admassie, S., Meng, J., Akwogu, O., Akande, W., Soboyejo, W. O., Tong, T., Babatope, B., Admassie, S., Meng, J., Akwogu, O., & Akande, W. (2015). *Adhesion in*

organic electronic structures. *083708*(2009). https://doi.org/10.1063/1.3246786

Travis, W., Glover, E. N. K., Bronstein, H., Scanlon, D. O., & Palgrave, R. G. (2016). On the application of the tolerance factor to inorganic and hybrid halide perovskites: a revised system. *Chemical Science*, *7*(7), 4548–4556. https://doi.org/10.1039/C5SC04845A

W, L., D, Z., Y, Y., N, S., K, G., CR, G., C, W., Y, X., AJ, C., RJ, E., NJ, P., K, Z., RG, X., & Y, Y. (2016). Fabrication of Efficient Low-Bandgap Perovskite Solar Cells by Combining Formamidinium Tin Iodide with Methylammonium Lead Iodide. *Journal of the American Chemical Society*, *138*(38), 12360–12363. https://doi.org/10.1021/JACS.6B08337

Wang, B., Bao, S., Vinnikova, S., Ghanta, P., & Wang, S. (2017). Buckling analysis in stretchable electronics. *Npj Flexible Electronics*, *1*(December 2016), 1–9. https://doi.org/10.1038/s41528-017-0004-y

Watanabe, M. (2012). Wrinkles with a well-ordered checkerboard pattern, created using dip-coating of poly (methyl methacrylate) on a UV-ozone-treated poly (dimethylsiloxane) substrate. *Soft Matter*, *8*(5), 1563–1569. https://doi.org/10.1039/C2SM06669F

Wu, D., Xie, H., Yin, Y., & Tang, M. (2013). Micro-scale delaminating and buckling of thin film on soft substrate. *Journal of Micromechanics and Microengineering*, *23*(3). https://doi.org/10.1088/0960-1317/23/3/035040

Yang, W. S., Noh, J. H., Jeon, N. J., Kim, Y. C., Ryu, S., Seo, J., & Seok, S. Il. (2015). High-performance photovoltaic perovskite layers fabricated through intramolecular exchange. *Science*, *348*(6240), 1234–1237. https://doi.org/10.1126/SCIENCE.AAA9272

Yang, Y., You, J., Hong, Z., Chen, Q., Cai, M., Song, T. Bin, Chen, C. C., Lu, S., Liu, Y., & Zhou,

H. (2014). Low-temperature solution-processed perovskite solar cells with high efficiency and flexibility. *ACS Nano*, *8*(2), 1674–1680. https://doi.org/10.1021/NN406020D/SUPPL_FILE/NN406020D_SI_001.PDF

Yin, Y., Tian, W., Luo, H., Gao, Y., Zhao, T., Zhao, C., Leng, J., Sun, Q., Tang, J., Wang, P., Li, Q., Lü, X., Bian, J., & Jin, S. (2021). Excellent Carrier Transport Property of Hybrid Perovskites Sustained under High Pressures. *ACS Energy Letters*, 154–161. https://doi.org/10.1021/ACSENERGYLETT.1C02359

You, J., Hong, Z., Yang, Y. M., Chen, Q., Cai, M., Song, T., & Chen, C. (2014). *Perovskite Solar Cells with High E ffi ciency and Flexibility*. *2*, 1674–1680.

Yu, D., Oyewole, O. K., Kwabi, D., Tong, T., Anye, V. C., Asare, J., Rwenyagila, E., Fashina, A., Akogwu, O., Du, J., & Soboyejo, W. O. (2014). *Adhesion in flexible organic and hybrid organic / inorganic light emitting device and solar cells*. *074506*. https://doi.org/10.1063/1.4892393

Yu, J. C., Kim, D. Bin, Baek, G., Lee, B. R., Jung, E. D., Lee, S., Chu, J. H., Lee, D. K., Choi, K. J., Cho, S., & Song, M. H. (2015). High-Performance Planar Perovskite Optoelectronic Devices: A Morphological and Interfacial Control by Polar Solvent Treatment. *Advanced Materials (Deerfield Beach, Fla.)*, *27*(23), 3492–3500. https://doi.org/10.1002/ADMA.201500465

Zhou, C., Lin, H., He, Q., Xu, L., Worku, M., Chaaban, M., Lee, S., Shi, X., Du, M. H., & Ma, B. (2019). Low dimensional metal halide perovskites and hybrids. *Materials Science and Engineering: R: Reports*, *137*, 38–65. https://doi.org/10.1016/J.MSER.2018.12.001

Zhou, H., Chen, Q., Li, G., Luo, S., Song, T. B., Duan, H. S., Hong, Z., You, J., Liu, Y., & Yang,

Y. (2014). Interface engineering of highly efficient perovskite solar cells. *Science*, *345*(6196), 542–546. https://doi.org/10.1126/SCIENCE.1254050

Zhu, Q., Bao, X., Yu, J., Zhu, D., Qiu, M., Yang, R., & Dong, L. (2016). Compact Layer Free Perovskite Solar Cells with a High-Mobility Hole-Transporting Layer. *ACS Applied Materials and Interfaces*, *8*(4), 2652–2657. https://doi.org/10.1021/ACSAMI.5B10555

Chapter 3
PRESSURE-ASSISTED FABRICATION OF PEROVSKITE SOLAR CELLS

3.1. Introduction

In recent years, organic - inorganic metal halide perovskites have been integrated into photovoltaic solar cells with power conversion efficiencies that have increased from ~ 3.8% to ~ 23.3% over a period of about 9 years (Cho et al., 2017b; Christians et al., 2018; Qiu et al., 2018; D. Yang et al., 2018; W. S. Yang et al., 2017). Since these structures can be produced using low-cost processing techniques (Y. Yang et al., 2014), this suggests that perovskite solar cells have the potential to compete with silicon solar cells that are now used in the photovoltaic industry (Liang et al., 2014). Furthermore, since perovskite solar cells are produced at relatively low temperatures (<120°C), a wider range of potential substrates and electrode materials can be integrated into their multilayered structures (D. Yang et al., 2018). These include polymer-based flexible substrates with well adhered layers (Kumar et al., 2013), as well as transparent substrates that work well under low temperature conditions (Grinberg et al., 2013). Hence, perovskite solar cells have the potential to offer the 'golden four' characteristics of solar cell technology. This includes low cost, stability, efficiency and added functionality (Fakharuddin et al., 2014).

Pressure is a unique variable that can be used to control the electronic structure and properties of organic-inorganic perovskite solar cells (Xiao et al., 2017). The application of pressure can lead to close packing, while reducing the interatomic distances. This could result ultimately in changes in the electronic orbitals and bonding patterns (Xiao et al., 2014). Hence, the application of pressure can induce changes in the structural, optical, magnetic and electronic properties (Tan & Cheetham,

2011) of organic and inorganic solids. The application of pressure can also increase the contact between layers that are present in solar cell structures. Such contacts can suppress crack growth along the interfaces (Campos et al., 2009; Cao et al., 2005; Fina et al., 2011; Geissler et al., 2003; B. C. Kim & Forrest, 2003; J. H. Kim et al., 2007). It can also promote charge and light transport across the interfaces of solar cells. Understanding the effect of pressure on the layers of organic-inorganic materials can enable us to tune material properties through compression.

Several methods have been used to improve the optoelectronic performance of perovskite solar cells (Chen et al., 2014; Cho et al., 2017a; W. S. Yang et al., 2017; Zhao et al., 2016). These include: the optimization of processing conditions (Cho et al., 2017b), the use of modifying agents (Noel et al., 2014), and the control of starting materials (Tai et al., 2011). Prior work (Agyei-Tuffour et al., 2016; Asare et al., 2016; Doumon et al., 2017; J. Du et al., 2014) has shown that the performance of organic electronic devices (solar cells and light emitting devices) can be improved by application of pressure. In the case of organic light emitting devices (OLEDs), the turn-on voltages of molybdenum trioxide based organic light emitting devices (OLEDs) have been significantly reduced by pressure application (J. Du et al., 2014). Improved efficiencies have also been reengineered in organic solar cells (OSCs) (from 3.5% to 4.4%) by the application of pressures of up to 10 MPa (Doumon et al., 2017). In both cases (OLEDs and OSCs), the improvements in device performance have been attributed largely to the effects of increased interfacial contacts that are associated with the application of pressure (Doumon et al., 2017; J. Du et al., 2014; O. K. Oyewole et al., 2015). However, excessive application of pressure can also lead to the "sink in" of interlayer particles (Xiao et al., 2017), that are present at the interfaces. These can result in layer damage, and a decrease in device efficiency.

In this study, we use a combined computational/analytical and experimental approach to study the effects of pressure on the photoconversion efficiencies of multilayered perovskite solar cells. First, we use computational finite element simulations and analytical models to simulate the effects of pressure on interfacial surface contacts in the layered mixed halide PSCs. The models and simulations, which incorporate the mechanical properties of the layers in the perovskite solar cells (Feng, 2014; Sun et al., 2015), show that contact between the layers increases with increasing applied pressure. The results reveal that increasing pressure results in the densification of the mesoporous layers and the infiltration of the mesoporous layers with the perovskite layers.

The resulting perovskite solar cells have photoconversion efficiencies that increase from ~ 9.84 (9.40 $\pm$ 0.70) to 13.67 (13.10 $\pm$ 0.70) %, for pressure values between 0 and 7 MPa. However, the photoconversion efficiencies decrease with increasing pressure, for pressures beyond 7 MPa, where the increasing initial trends in the photoconversion efficiencies ($p < 7$ MPa), are attributed to the improved surface contacts and the initial densification and infiltration of the mesoporous layer that are associated with increasing applied pressure. However, the subsequent decrease in photoconversion efficiencies at higher pressures ($p > 7$ MPa) is associated with the fragmentation of the perovskite grains, and the sink-in of the perovskite layers into the mesoporous TiO_2 layer (device damage).

3.2. Modeling of Interfacial Surface Contacts Due to Pressure Effect

The interfacial contact between the layers of perovskite solar cells is important for effective transportation of charges and for work function alignment (Bietsch & Michel, 2000; Geissler et al., 2003). The integrity of the interfaces in the resulting multilayered structure also depends on the surface roughnesses of the adjacent layers (Li et al., 2018) and as well as the

cleanliness of the environments that are used for device fabrication (Malinkiewicz et al., 2014). There are impurities/interlayer particles that can be embedded between layers in clean rooms (Cao et al., 2005; Dumond & Yee Low, 2012). These impurities include: particles of silicone, silicon, silica, textile polymer and organic materials (Cao et al., 2005; W.M.Moreau, 1988) with diameters ranging from ~ 0.1 to 20 μm. The presence of these particles reduces the effective contact areas (**Figure** 3.1a) of the bi-material pairs that are relevant to the PSCs. Hence, the application of moderate pressure (to PSCs) can improve the interfacial contacts between layers that sandwich the particles (**Figure** 3.1b). At higher pressures (**Figure** 3.1c), however, the sink in of the trapped impurities/particles can induce damage in surrounding layers in ways that can result in reduced solar cell photoconversion efficiencies.

Hence, this section presents an analytical model for the prediction of surface contacts between layers that are relevant to PSCs. The deformation of thin films (due to applied pressure) was idealized by modeling the deformation of a cantilever beam around the particles (Akande et al., 2010; Hur et al., 2005; Wan & Mai, 1995), as shown in **Figures** 1d – 1f. This gives (Asare et al., 2016; O. K. Oyewole et al., 2015; Oluwaseun K. Oyewole, 2015):

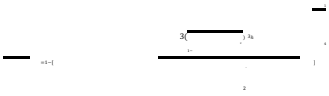

(1)

where h is the height of the impurity particle, t is the thickness of the top layer (cantilever) that deforms upon pressure application, is the void length, is the contact length, is the length of the cantilever beam, is the Young's modulus, is the Poisson ratio and is the applied pressure. Hence, using the materials properties of the films and particles summarized in **Table** 3.1, the interfacial surface contact lengths can be estimated for the range of pressures and film thickness

and roughnesses that are relevant to the different bi-layer configurations in the multilayered perovskite solar cells structures.

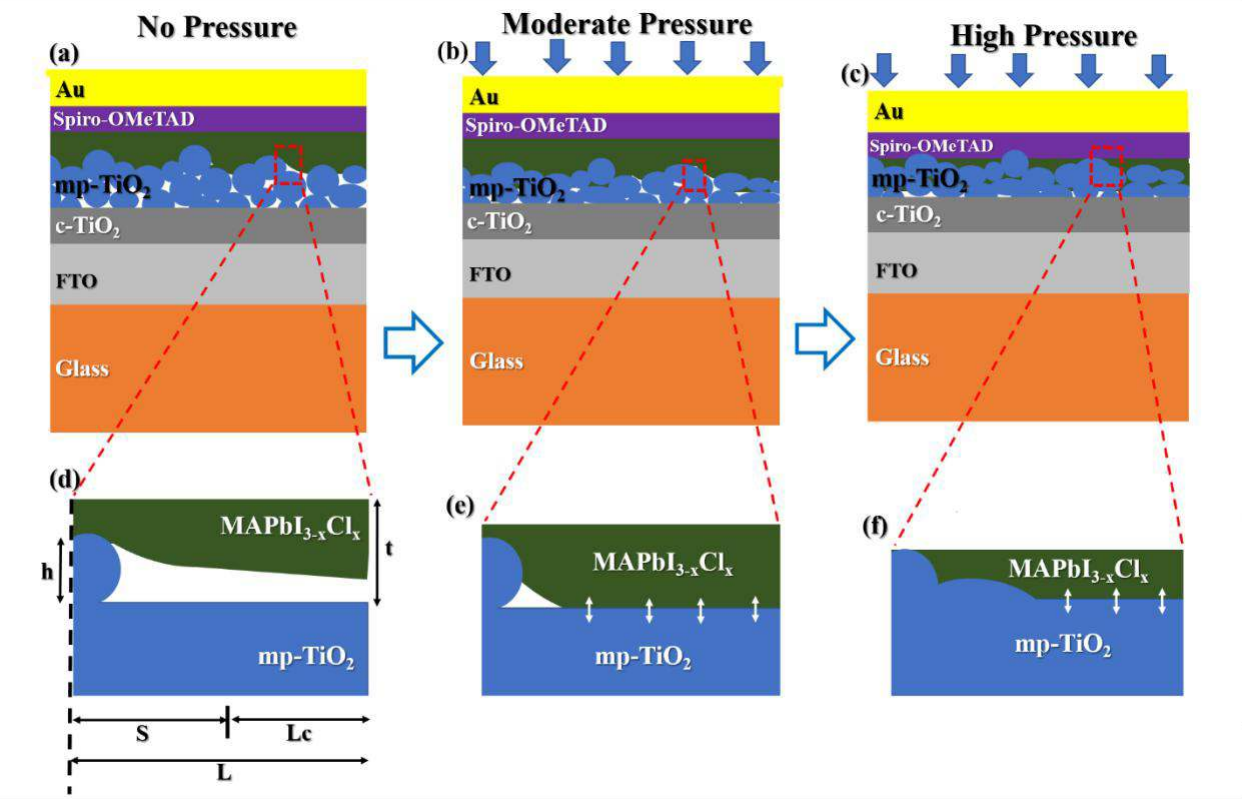

***Figure 3.1**. Schematics of the interfacial surface contact: (a) no pressure; (b) moderate pressure; (c) high pressure. Axisymmetric model of interfacial surface contact for: (d) no pressure case; (e) moderate pressure case and (f) high pressure.*

3.3. Experimental Methods

3.3.1. Processing of perovskite solar cells:

FTO-coated glass (Sigma Aldrich) was cleaned successively in an ultrasonic bath (for 15 minutes each) in deionized water, acetone (Sigma Aldrich) and IPA (Sigma Aldrich). The cleaned glass was then blow-dried in nitrogen gas, prior to UV- Ozone cleaning (Novascan, Main Street Ames,

IA, USA) for 20 minutes to remove organic residuals. Subsequently, an electron transport layer (ETL) (that comprises compact and mesoporous layers of titanium oxide) was deposited onto the FTO-coated glass. First, a compact titanium oxide (c-TiO_2) was spin-coated onto the cleaned FTO-coated glass from a solution of titanium diisopropoxide bis (acetylacetone) (0.15 M in1-butanol) at 2000 rpm for 30 s. This was followed by 5 minutes of annealing at 150^{o}C before spin coating another layer of titanium diisopropoxide bis (acetylacetone) (0.3 M in 1-butanol) at 2000 rpm for 30 s. The deposited c-TiO_2 was then annealed in a furnace (Lindberg Blue M, Thermo Fisher Scientific) at 500^{o}C for 30 minutes. The sample was then allowed to cool down to room-temperature (~ 25^{o}C). A mesoporous titanium oxide (mp-TiO_2) was spin coated from a solution of titanium oxide paste (20 % in ethanol) at 5000 rpm for 30 s before sintering at 500^{o}C for 30 mins in a furnace (Lindberg Blue M, Thermo Fisher Scientific). This was then transferred into a nitrogen filled glove box, where the photoactive perovskite and the hole transport layers were deposited.

A mixed halide perovskite solution was prepared from a mixture of 222.5 mg of lead (II) iodide (PbI_2) (> 98.9 % purity, Sigma Aldrich) and 381.5 mg of methylammonium chloride (MACl) (> 99% purity, Sigma Aldrich) in 1 ml of dimethylformamide (DMF) (Fisher Scientific). This was then stirred at 60^{o}C for 6 hours in the nitrogen filled glove box. The solution was filtered using a 0.2 µm mesh filter before spin-coating onto mp-TiO_2 at 2000 rpm for 50 s. After 30 s of the spin coating of the perovskite layer, 300µl of chlorobenzene was then dispensed onto the film. The perovskite film was then crystallized by annealing at 90^{o}C for 30 minutes to crystallize. Finally, a solution of 2, 2′, 7, 7′-tetrakis (N,N-di-p-methoxxyphenylamine)-9, 9′-spirobifluorene (Spiro-OMeTAD) (> 99 % purity, Sigma Aldrich) was spin coated at 5000 rpm for 30 s.
The Spiro-OMeTAD solution was prepared from a mixture of 72 mg of Spiro-OMeTAD in 1ml of chlorobenzene, 17.5 µl of lithium bis (trifluoromethylsulphony) imide (Li-FTSI) (Sigma

Aldrich) (500mg in 1ml of acetonitrile), 29 µl of tris(2-(1H-pyrazol-1-yl)-4-ter-butylpyridine)-cobalt (III) tris(bis(trifluoromethaylsulfony) imide) (FK209) (Sigma Aldrich) (100 mg in 1 ml of acetonitrile) and 28.2 µl of 4-tert-butylpyridine (tBP) (Sigma Aldrich). The above film was kept overnight in a desiccator before thermally evaporating a ~ 80.0 nm thick gold (Au) layer onto the Spiro-OMeTAD from an Edward E306A evaporation system (Edward E306A, Easton PA, USA). The evaporation was carried out under a vacuum pressure of $< 1.0 \times 10^{-5}$ Torr at a rate of 0.15 nm s^{-1}. Shadow masks were used to define both small and large device active areas of 0.10 cm^2 and 1.1 cm^2 respectively. The resulting device architecture is shown in **Figure 3.**2.

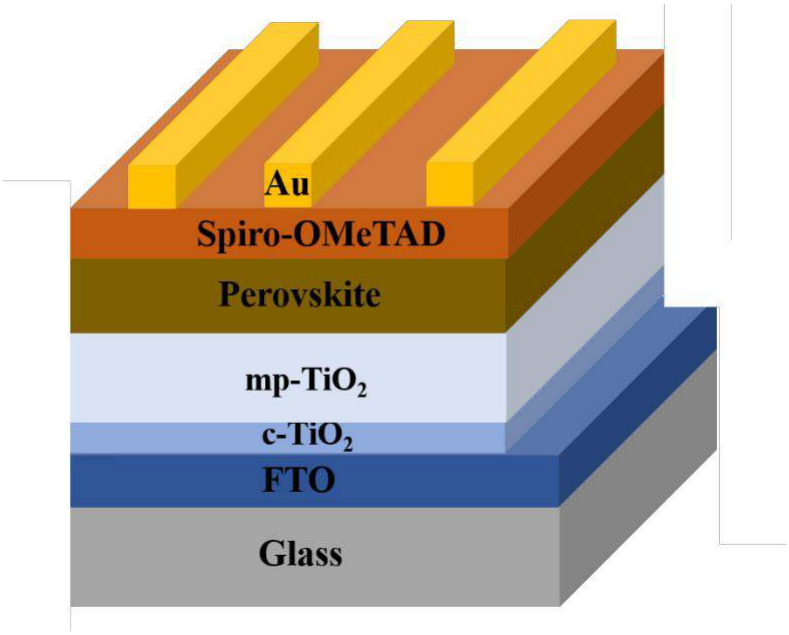

Figure 3.2*. Schematic of perovskite solar cell architecture* **3.3.2. Pressure Experiments**

A range of pressures (0-10 MPa) was applied to the fabricated perovskite solar cells. This was done using a model 5848 MicroTester Instron electrochemical testing machine (Instron, Norwood, MA, USA) with a PDMS anvil placed on the device. First, the PDMS anvil was fabricated from a mixture of Sylgard 184 silicone elastomer base and Sylgard 184 silicone elastomer curing agent

(Dow Corning Corporation, Midland, M I) in a ratio 10:1 by weight. The mixture was degassed and cured (at 65^{o}C for 2 hours) in a mold with a shining silicon base. The PDMS anvil was then cut out into the dimensions of the device glass substrate.

The pressure experiments are summarized schematically (**Figure** 3.3a) along with information on the Instron MicroTester set-up (**Figure** 3.3b). The Instron was set to ramp in compression at a displacement rate of 1.0 mm.min^{-1}, followed by a hold at 2 MPa for 10 minutes. Unloading was then carried out at a displacement rate of ~ -1.0 mm.min^{-1}. This cycle was then repeated to different peak pressures (from 2 MPa to 10 MPa) on the perovskite solar cells and perovskite layers.

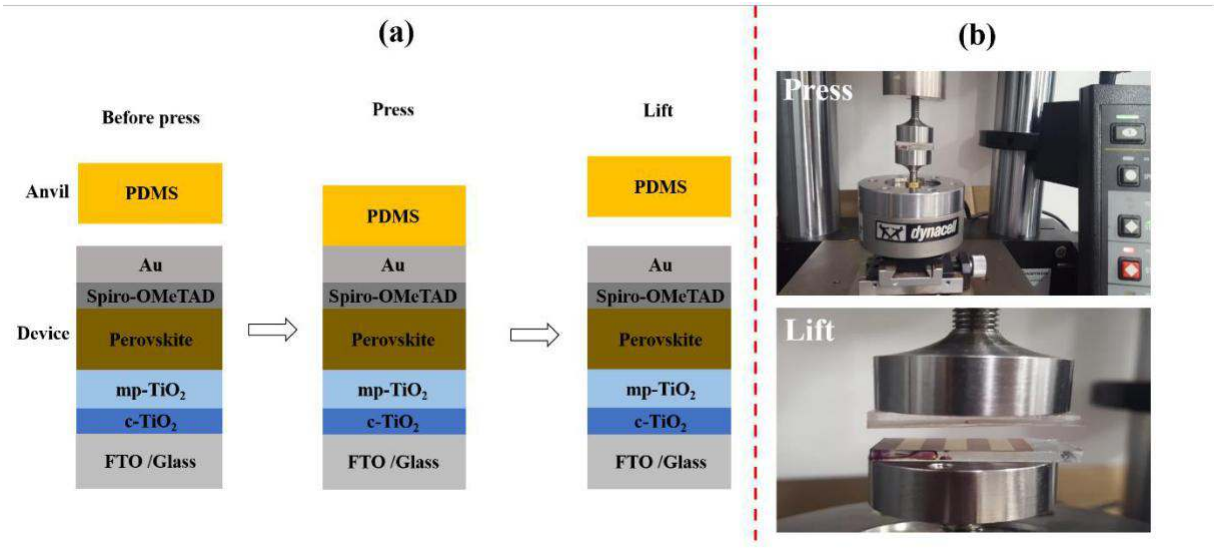

Figure 3.3. *(a) Schematics of the pressure application procedures, showing before press, press and lift of the PDMS anvil. (b) Picture of the set-up of pressure application on the devices using Micro Tester Instron machine for press and lift-up of the anvil.*

3.3.3. Characterization of Current Density-Voltage Behavior

Plots of current density against voltage (J-V) were obtained for the fabricated perovskite solar cells. These were measured (before and after the pressure treatment) using a Keithley SMU2400 system (Keithley, Tektronix, Newark, NJ, USA) that was connected to an Oriel simulator (Oriel, Newport Corporation, Irvine, CA, USA) under AM1.5G illumination of 100 mW cm^{-2}. The J-V curves of devices (with zero pressure) were first measured before subsequent J-V measurements of the devices that were subjected to applied pressures of 0 - 10 MPa.

The optical absorbances of the as-prepared and pressure-assisted perovskite layers were measured using an Avantes UV-Vis spectrophotometer (AvaSpec-2048, Avantes, BV, USA). The X-ray diffraction patterns of as-prepared and pressure-assisted perovskite layers were also obtained using an X-ray diffractometer (Malvern PANalytical, Westborough, MA, USA). The microstructural changes of the as-prepared and pressure-assisted perovskite layers were also observed using field emission scanning electron microscope (SEM) (JEOL JSM-700F, Hollingsworth & Vose, MA, USA).

3.3.4 Computational Modeling of the Pressure-Assisted Perovskite Solar Cells

The finite element simulations of the effects of pressure treatment were carried out using the Abaqus software package (Dassault Systemes Simulia Corporation, Providence, RI, USA). The effects of the clean room particles were considered in the simulations of contact between transport layer (TiO_2) and the photoactive active layer (perovskite). The segments of the devices in the region of the embedded particles were analyzed in the simulations. For simplicity, axisymmetric geometries were used as shown in Figure 3.5a. We assumed that the part of the device, which is

farther from the dust particle, had no significant effect on the mechanics around the dust particle. Majority of the airborne particles in semiconductor clean room environment have a diameter of 1 which is about four times the thickness (250 - 400 nm) of the device active layer. In our simulation, a diameter of 1 was chosen for the dust particle. The mechanical properties of these particles are summarized in **Table** 3.1.

A four-node bilinear axisymmetric quadrilateral element was used in the mesh. The mesh was dense in the regions near the dust particle and the contact surfaces. Identical mesh sizes were also used in the regions near the surface contact regimes to assure convergence in contact simulation. All the materials were assumed to exhibit isotropic elastic behavior. Young's moduli of the materials were obtained from the nanoindentation experiments as described in prior studies. The Young's moduli and the Poisson's ratios of the materials used in the simulations are summarized in **Table** 3.1. The axisymmetric boundary condition was applied at the symmetry axis (**Figure** 3.5a). The bottom of the substrate was fixed to have no displacements and rotations. The outer edge of the model was also fixed to have no lateral movement for continuity, while a pressure was applied from the stamp onto the device.

3.4. Results and Discussion

The contact length ratios, / , associated with the effects of applied pressures were obtained by the substitution of appropriate parameters into Equation 1. First, we considered the effects of varying the thickness of the perovskite layer (100 - 400 nm) and the interlayer particle sizes (W.M.Moreau, 1988). The results of the analytical modeling of surface contact are presented in **Figure 3.**4. For different thicknesses of the perovskite films, the interfacial surface contact length ratio / increases with increasing applied pressure (**Figure 3.**4a). The thinner films also require

less pressure to wrap round the particles. This results in higher interfacial surface contacts around interlayer particles between thinner layers.

In the case where the particle sizes vary under different clean room conditions, decreasing particle sizes results in increasing interfacial surface contact (**Figure 3.**4b).

However, upon the application of pressure, the contact length ratios / increase with increasing applied pressure. The above results are also consistent with previous applications of Equation 1 to organic solar cells (Asare et al., 2016; Doumon et al., 2017) and organic light emitting diodes (J. Du et al., 2014)**.** The analytical model results suggest that increased pressure caused increased contact between the perovskite active layer and the adjacent layers, which improves transportation of charges and work function alignment across interfaces. However, excessive pressure can lead to sink-in of the particles (Ashby, 1997; B. C. Kim & Forrest, 2003)**,** which can cause damage to the adjacent layers in perovskite solar cells. The perovskite layers can also sink into the adjacent mesoporous layers, leading ultimately to short circuiting (**Figure 3.**1). Therefore, for best results, moderate intermediate pressures are required for improved contact.

Finite element modeling was also used to explore the effects of pressure on the surface contact length ratios / , and interlayer/impurity particle sink-in. Previously obtained materials properties (Park et al., 2015; Reyes-Martinez et al., 2017; Soboyejo, 2003; Sun et al., 2015; Tavakoli et al., 2016) (**Table** 3.1) were incorporated into the finite element modeling, which was carried out using the ABAQUS software package (ABAQUS Dassault Systemes Simulia Corporation, Providence, RI, USA). The models utilized axisymmetric geometries of the device architecture. They were simplified by considering a sandwiched particle between two layers, along one of the interfaces of the device structure. The axisymmetric boundary condition was applied along the symmetry axis (**Figure** A.1, **Appendix** A.1). The bottom of the substrate was also fixed

to have no displacements or rotations. For continuity, the outer edge of the model was also fixed to have no lateral motion, while a pressure was applied from a stamp. The details of the finite element simulations are presented in **Appendix** A.1.

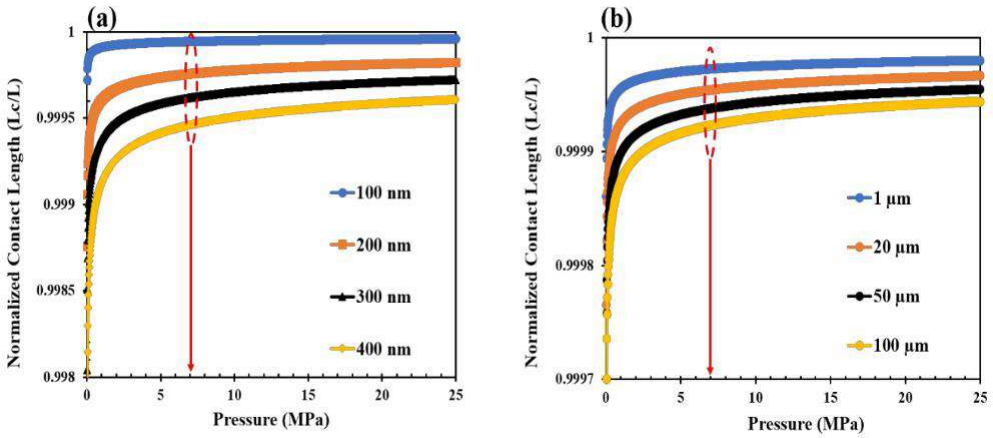

***Figure 3.4**. Analytical model prediction of pressure effects on contact length ratios, / : (a) effects of pressure on the surface contacts for different thicknesses of the films (for particle size of 1µm) and (b) effects of pressure on surface contacts for different sizes of the particles (for a film thickness of 250 nm).*

The results of the finite element simulations (before and after pressure application) are presented in **Figures** 3.5a and 3.5b, respectively, for the interfacial surface contact between perovskite layer and mesoporous TiO_2 layer. Similar improvements in pressure-induced contacts were observed at other interfaces in the device structure. Furthermore, the interfacial surface contacts increased with increasing pressure (1 MPa – 10 MPa), as shown in **Figures** 3.6a – 3.6f. Note that the effects of pressure, and the material properties of the interlayer particles on the surface contact, are presented in **Figures** 3.7a – 3.7f. These show that the interfacial void lengths (between adjacent layers) are greatly reduced with decreasing interlayer particle moduli between 70 GPa – 0.17 GPa (for the

same pressure of MPa). This range of Young's moduli corresponds to the material properties of particles (Bietsch & Michel, 2000; Cao et al., 2005; Jing Du et al., 2013; W.M.Moreau, 1988) that are found in clean room environments (**Table** 3.1).

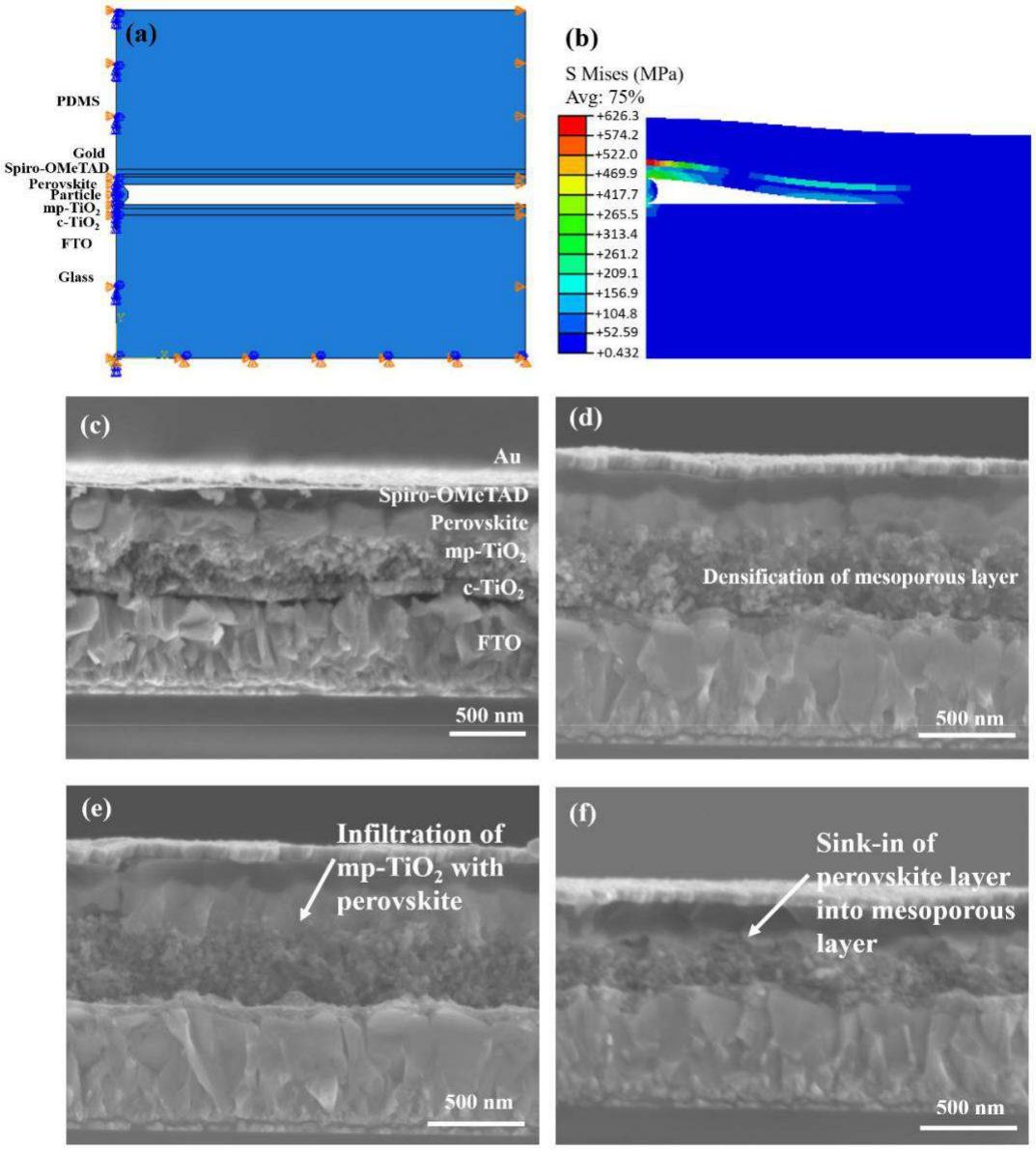

Figure 3.5. *Interfacial surface contacts in perovskite solar cells before and after pressure applications: (a) Stress distributions before contact; (b) Stress distributions after contact; (c)*

Cross section of interfacial void before pressure application; (d) Densification of mesoporous layer after contact, (e) Infiltration of mesoporous structure with perovskite (p = 7 MPa) and (f) Sink-in of the perovskite layer into mesoporous and damage (p = 10 MPa).

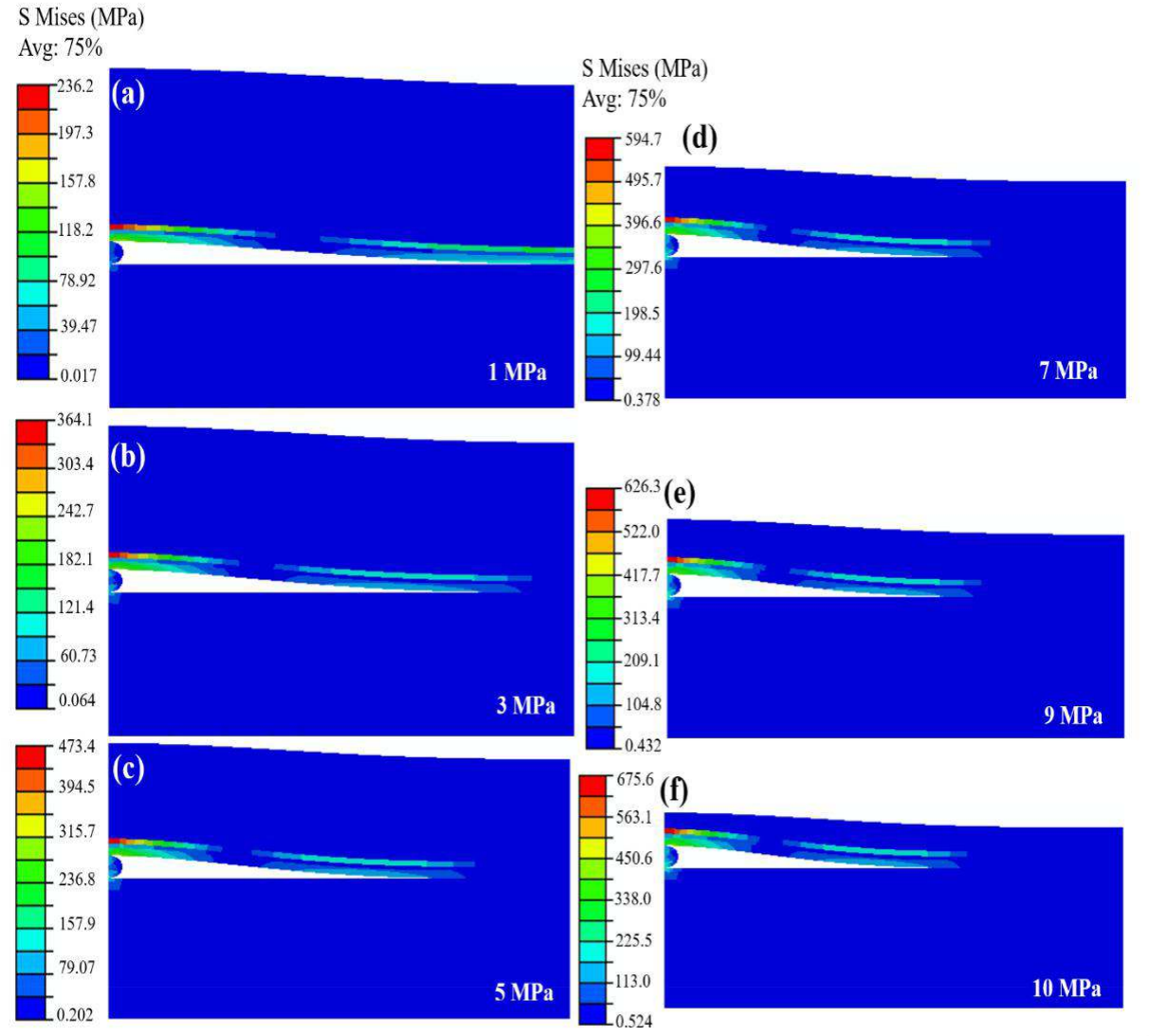

Figure 3.6. *Stress distribution in perovskite solar cells during pressure application at (a) 1 MPa, (b) 3 MPa, (c) 5 MPa, (d) 7 MPa, (e) 9 MPa and (f) 10 MPa. The interfacial surface contact of the increases with increased pressure, while the interfacial void decreases. The color scale bars indicate the stress mises in MPa*

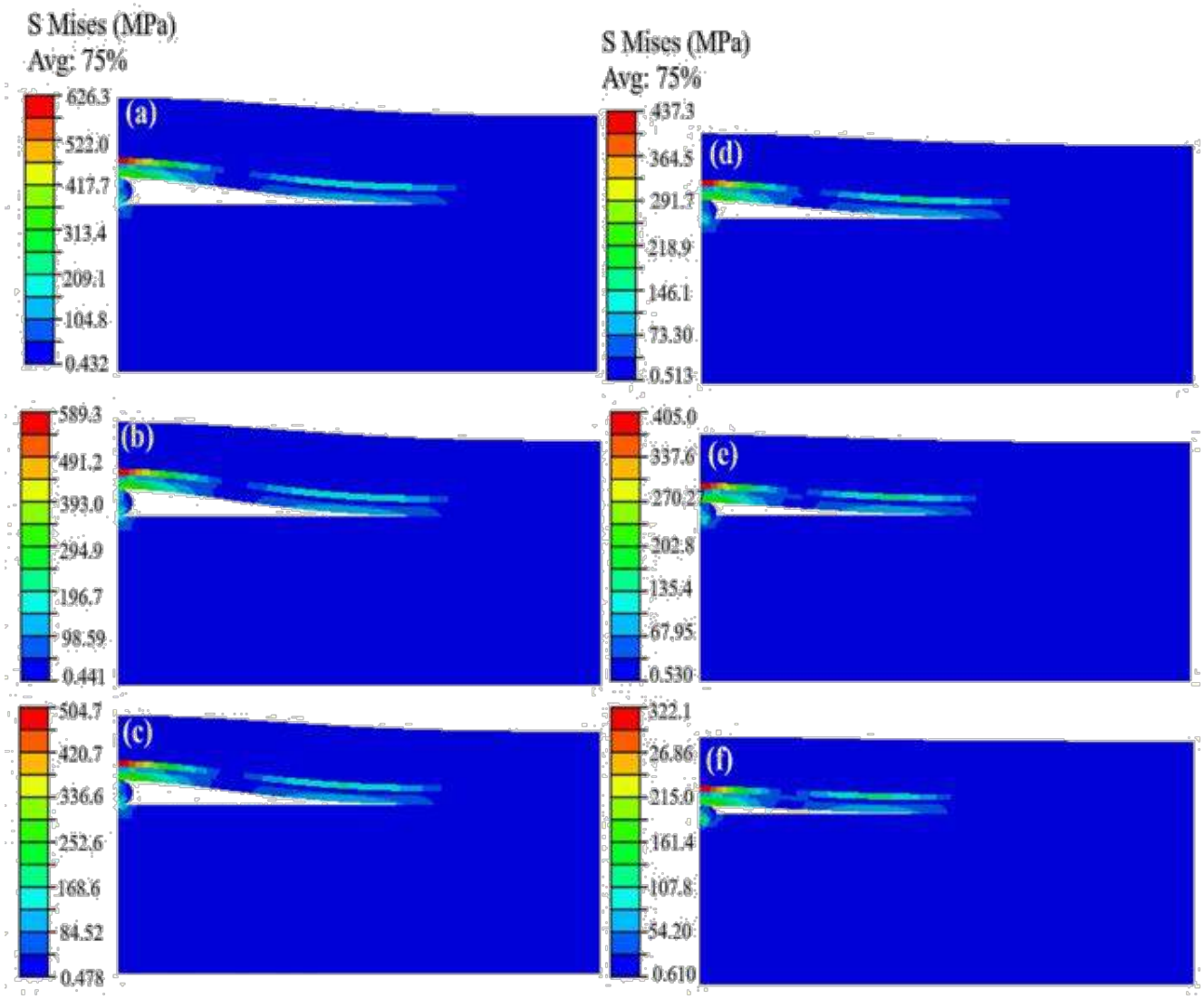

Figure 3.7. *Stress distribution in perovskite solar cells during pressure application, showing effects of particles materials properties. For pressure of 9 MPa, the interfacial void reduces for particles with material properties of (a) 70 MPa, (b) 20 GPa, (c) 500 MPa, (d) 300 MPa, (e) 250 MPa and (f) 170 MPa. The color scale bars indicate the stress mises in MPa.*

The above analytical and computational results are consistent with microstructural observations of the device cross sections (before and after the application of pressure), as shown in **Figures** 3.5a-

3.5d. Note that there were significant interfacial voids between the layers of the perovskite solar cells before the application of pressure (**Figure** 3.5c). However, the interfacial void lengths were reduced, and the mesoporous layers were compacted **Figure** 3.5d) after the application of a pressure of 7 MPa, which resulted in the infiltration of the mesoporous TiO_2 layers with perovskite (**Figure** 3.5e). Sink-in of the perovskite (into the adjacent mesoporous layer) was also observed at a pressure of 10 MPa (**Figure** 3.5f). This is consistent with the compaction and damage phenomena associated with the compressive deformation of porous materials(Ashby, 1997).

Table 3.1. *Mechanical properties of materials used in the analytical modeling and finite element simulations. The clean room particles (Bietsch & Michel, 2000; Cao et al., 2005; Jing Du et al., 2013; W.M.Moreau, 1988) that can constitute interfacial surface void are classified along with the mechanical properties of device materials(Park et al., 2015; Reyes-Martinez et al., 2017; Soboyejo, 2003; Sun et al., 2015; Tavakoli et al., 2016)*.

Class	**Materials**	**Young's modulus (GPa)**	**Poisson ratio**
Clean room particles	Silicone	0.001 – 0.02	0.3
	Photoresist	1 -8	0.3
	Aluminium	70	0.3
Device Materials	FTO	206	0.32
	TiO_2	210	0.3
	Perovskite	19.77	0.33
	Spiro-OMeTAD	15	0.36
	Au	78	0.48
	PDMS	0.003	0.3

The effects of pressure are also evident in the structural and optical properties of the perovskite solar cells. The XRD patterns of the as-prepared perovskite films and those produced via pressure-assisted fabrication are shown in **Figure** 3.8a. It is of interest to discuss the observed effects of pressure on the crystallization of the perovskite layer. Our results show that the 110 and 220 peaks increase with increasing pressure between 0 MPa and 7 MPa. However, the peaks decrease with further increase in pressure (above 7 MPa). The SEM images of the perovskite films with the pressure-induced crystallization are shown in **Figures** 3.8b – 3.8d. Similar observations have been reported by Wang et al. (Wang et al., 2015) and Lu et al. (Lü et al., 2017) who attribute the increase to crystallization phenomena due to small bond lengths that occur with increased initial pressure. Such reduction in bond lengths are also associated with stress-induced phase transformations that increase the percentage of crystalline perovskite phases with (110) and (220) orientations. However, for pressure above 7 MPa, the 110 and 220 peaks were observed to decrease with increasing pressure. The decrease is attributed to the potential onset stress-induced amorphization (Jiang et al., 2016; Lü et al., 2017; Wang et al., 2015) that can occur due to cracking and damage phenomena. Such localized amorphization can reduce the overall crystallinity.

These crystalline structures have also been shown by Wang et al., (Wang et al., 2015) Yuan et al., (Yuan et al., 2019) Jiang et al. (Jiang et al., 2016) and Lu et al. (Lü et al., 2017) to have increased absorbance due to reduction of the band gap (Jiang et al., 2016; Liu et al., 2017; Lü et al., 2017; Wang et al., 2015; Yuan et al., 2019) in the low pressure regime. Our results show that the optical properties of the perovskite films increased with increasing applied pressure, as shown in **Figure** 3.8e. This shows that the optical absorbance of the films increases with pressures between 0 MPa and 7 MPa due to the decrease in bond lengths. The increase in the absorbance of the perovskite film due to increased pressures is evident in the reduction band gaps between 0 MPa and 7 MPa

(as shown in **Figure** 3.8f). For pressures above 7 MPa, the band gaps were observed to increase with increasing pressure. This can also be attributed to local stress-induced phase changes or amorphization phenomena that can occur due to pressure application.

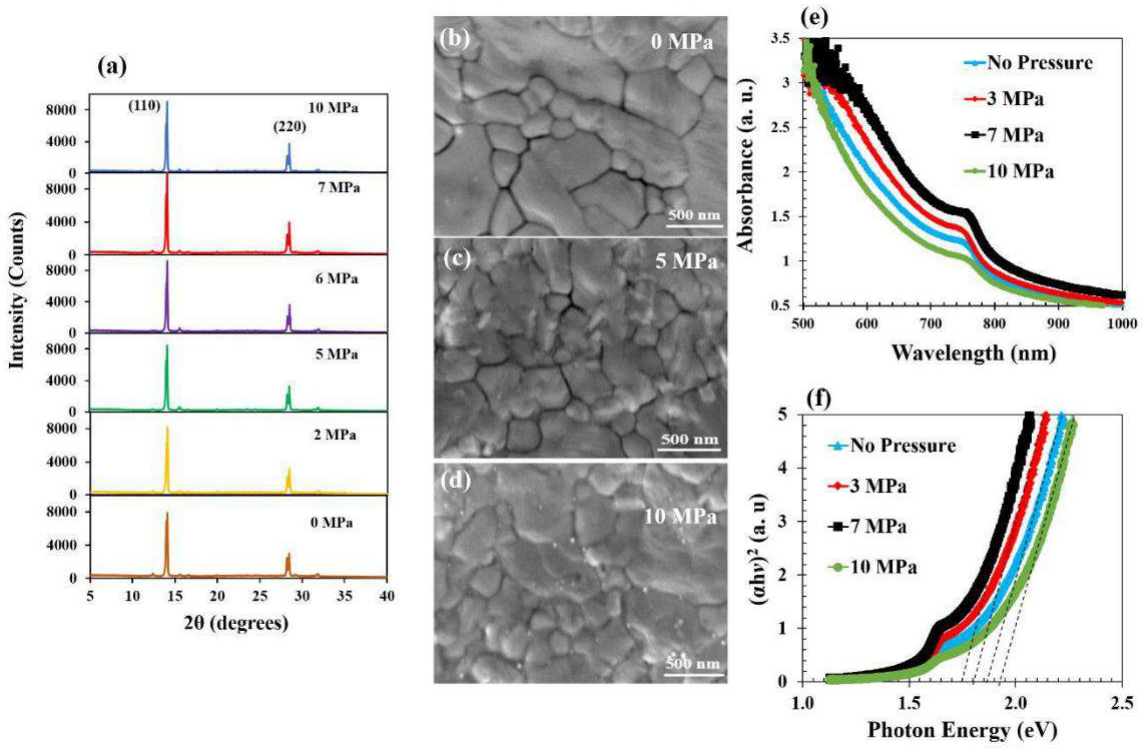

Figure 3.8. *(a) XRD patterns before and after pressure application, (b-d) SEM images of pressure-assisted perovskite films (e) optical absorbance and (f) plot of* $(\alpha h\nu)^2$ *versus photon energy.*

The band gaps were estimated by incorporating the absorption spectra into empirical formula (Ghobadi, 2013)

$$(\alpha h\nu)^2 = A(h\nu - E_g) \quad (2)$$

where h, ν, E_g and α are Planck constant, frequency, optical energy band gap and absorption coefficient, respectively. The decrease in the bandgap exhibits a red shift in the absorption edge

(Liu et al., 2017) that corresponds to an increase in the capacity to generate electron-hole pairs that can travel to the electrodes before recombination. It should, therefore, improve power conversion efficiencies. However, for applied pressures of 10 MPa and above, the optical absorbance decreased significantly with increasing applied pressure. High pressures can cause damage, which can lead to light scattering and unexpected blue shifts in the absorption edge.

The results of the device parameters (before and after pressures) are presented in **Figures** 3.9a-3.9g. A typical set of current density-voltage (J-V) curves obtained for the perovskite solar cells are presented in **Figure** 3.9a. The areas under the curves increased with increasing pressure. Each of the curves is an average of J-V curves obtained from five devices. The effects of applied pressure on short circuit current density (J_{sc}), open circuit voltage (V_{oc}), power conversion efficiency (PCE) and fill factor (FF) are presented in **Figures** 3.9b, 3.9c and 3.9d, respectively. The device characteristics are also presented in **Table** 3.2, while the overall device parameters obtained for other sets of devices are presented in **Table** 3.3.

Table 3.2. *Device characteristic parameters for pressure-assisted perovskite solar cells indicating the average of the PCEs*

Pressure (MPa)	V_{oc} (V)	J_{sc} ($mAcm^{-2}$)	FF	PCE ($PCE_{average}$) (%)
0.0	0.96 ±0.0078		19.25±1.20 0.53±0.008	9.84 (9.40 ± 0.70)
2.4	0.96 ±0.0056		20.05±0.60 0.61±0.007	11.66 (10.01 ± 0.60)
5.0	0.97±0.0038		21.71±0.06 0.62±0.004	12.94 (11.92 ± 0.60)
7.0	0.99±0.0045	22.82±0.70	0.61±0.005	13.67 (13.10 ± 0.70)
10.0	0.98±0.0027	19.03±0.30	0.56±0.003	10.89 (10.02 ± 0.30)

Table 3.3. *Detailed device parameters for perovskite solar cells*

Devices	Pressure (MPa)	Voc (V)	Jsc ($mAcm^{-2}$)	FF	PCE (PCE_{avg}) (%)
Set 1[a)]	0	0.82	20.88	0.46	7.91 (6.60 ± 0.90)
	2.4	0.92	21.38	0.54	10.43 (8.13 ± 0.84)
	5.6	0.92	21.44	0.56	11.58 (10.61 ± 0.74)
Set 2[b)]	0	0.83	26.64	0.41	9.22 (8.52 ± 0.61)
	2.4	0.83	27.64	0.40	9.22 (8.66 ± 0.40)
	5.6	0.84	31.85	0.50	13.22 (12.87 ± 0.48)
	7	0.84	31.72	0.45	11.65 (10.10 ± 0.49)
	10	0.83	23.87	0.31	6.22 (5.67 ± 0.52)
Set 3[c)]	0	0.92	17.51	0.54	8.72 (8.74 ± 0.40)
	2.4	0.92	19.42	0.61	10.87 (10.39 ± 0.50)
	5.6	0.91	20.14	0.61	11.23 (10.39 ± 0.90)
	7	0.9	20.11	0.62	11.12 (10.63 ± 0.50)
	10	0.92	16.92	0.47	7.13 (6.61 ± 0.80)
Set 4[d)]	0	0.96	19.25	0.53	9.84 (9.40 ± 0.70)
	2.4	0.96	20.05	0.61	11.66 (10.01 ± 0.60)
	5	0.97	21.71	0.62	12.94 (11.92 ± 0.60)
	7	0.99	22.82	0.61	13.67 (13.10 ± 0.70)
	10	0.98	19.03	0.56	10.89 (10.02 ± 0.30)

[a)]15 devices, 5 for each applied pressure; [b)]20 devices, 4 for each applied pressure; [c)]25 devices, 5 for each applied pressure; [d)]25 devices, 5 for each applied pressure; avg(average)

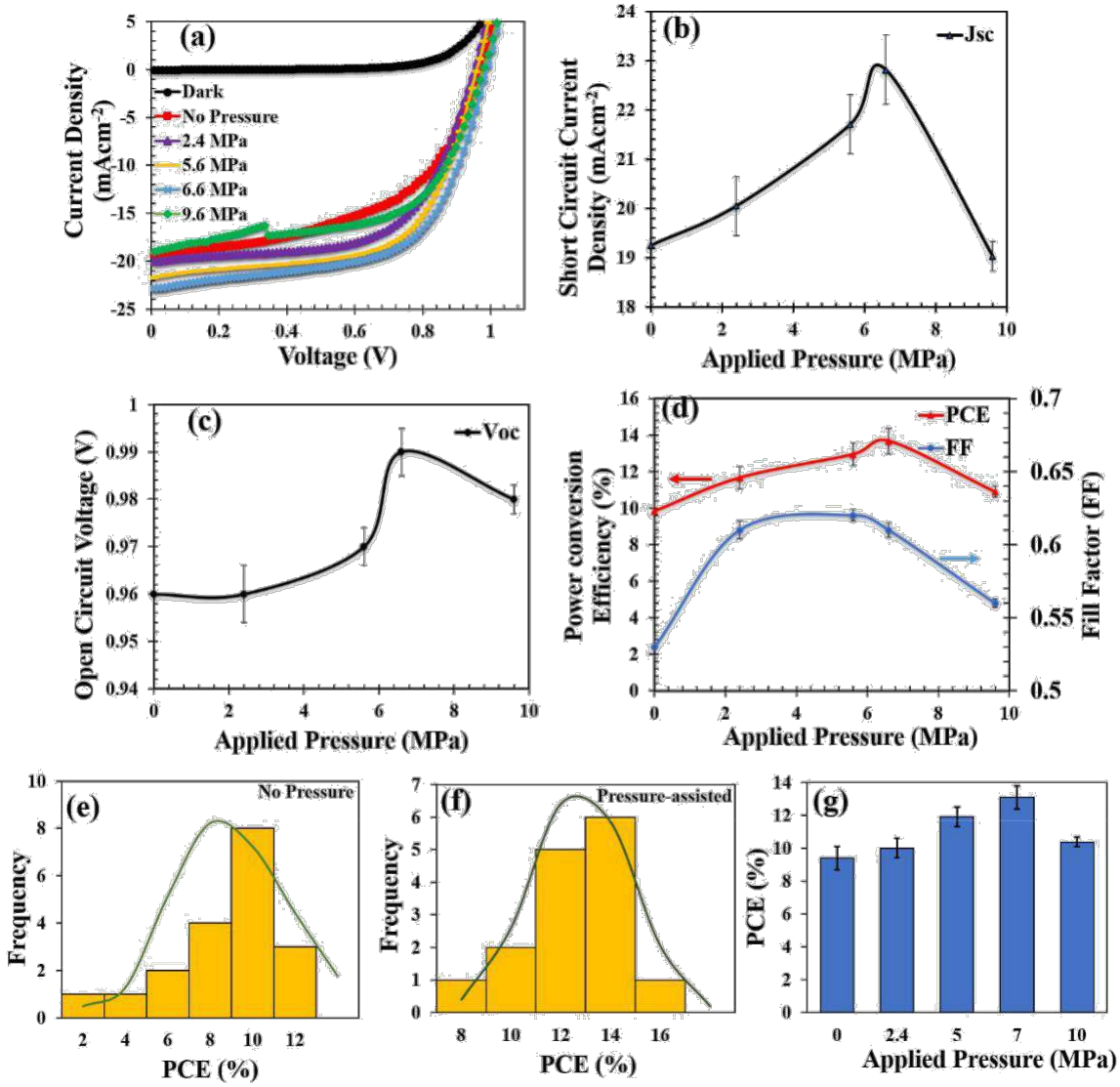

Figure 3.9. *Effects of pressure on performance parameters of perovskite solar cells: (a) Current density-voltage curves; (b) short-circuit current density; (c) open circuit voltage; (d) power conversion efficiency (PCE) and fill factor for different applied pressures; (e) histogram and normal distribution of the PCEs of unpressurized devices (f) histogram and normal distribution of the PCEs of devices subjected to pressure of 2-10 MPa; (g) Bar chart summarizing the effects of pressure discussed in all of the fabricated devices.*

There are two potential scenarios that could explain how relatively low applied pressures can result in high local stresses within the layered structures of perovskite solar cells. In the first scenario, which is illustrated in **Figure.** 3.5b, one can consider the role of interfacial impurities that can give rise to interfacial stress concentration due to elastic or elastic-plastic contact. An idealized example of this is elastic-contact between spherical shapes that is often idealized by Hertzian contact theory.

The second example, which is illustrated in **Figure** 3.10, is the case of interfacial or layer crack/notch subjected to remote stress, (as shown in **Figure** 3.10). In such a scenario, even under compressive loading, the induced local notch/crack stresses are much greater than the remote stresses. Furthermore, even under compressive loading, there can be induced local tensile stresses at the crack or notch tips. Such stresses may be sufficient to cause stress-induced phase changes or amorphization phenomena. Hence, it is possible to have local effects in the vicinity of such notch or crack tips that can induce phase changes/amorphization under conditions in which relatively low remote stresses are applied to a notched or cracked geometry. Based on the above arguments, the stress-induced phenomena can occur due to stress concentrations that are associated with elastic contacts around impurities and/or stress concentrations around interfacial notches or cracks.

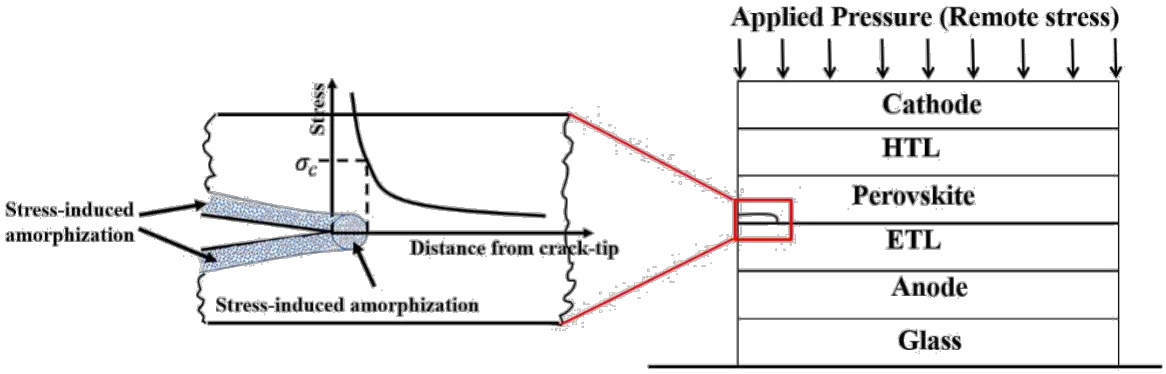

***Figure 3.10**. Schematic of a localized stress in an interfacial layer crack/notch within the multilayered structure of a perovskite solar cell subjected to remote pressure/stress (Effective high stresses at the crack or notch tips can induce amorphization).*

In the case of the perovskite solar cells that were fabricated without pressure application, the PCE and FF were 9.84 (9.40 ± 0.70) % and 0.53±0.008, respectively. However, with the application of pressure (up to 7 MPa), the PCE and FF increased up to 13.67 (13.10 ± 0.70) % and 0.61±0.005 %, respectively. For a higher applied pressure of 10 MPa, the PCE and FF both decreased slightly to 10.89 (10.02 ± 0.30) % and 0.56±0.003, respectively.

The device short circuit current density (J_{sc}) and open circuit voltage (V_{oc}) values (obtained at different applied pressures) increased with the applied pressures between 0-7 MPa. However, for higher applied pressures (p > 7 MPa), the performance parameters of the solar cells (J_{sc}, V_{oc}, FF and PCE) generally decreased (**Figures** 3.9b – 3.9d and 3.9f).

The PCEs obtained for devices fabricated with and without pressure are summarized in the histograms (**Figures 3.**9e and 3.9f) along with the normal distributions. The detailed histograms and normal distributions are presented in **Figure 3.11.** The bar chart in **Figure** 3.9g presents a summary of the effects of pressure on PCEs of all the 85 devices that were fabricated in this study.

The results show that the power conversion efficiencies increased with improved surface contacts at moderate pressures. However, the occurrence of interlayer particle sink-in and the compaction and damage of the mesoporous layer reduces the overall device efficiency at higher applied pressures (**Figure** 3.9d). Similar trends have been observed in organic solar cells (Doumon et al., 2017). However, these do not include the compaction of the mesoporous layers, which were present only in the perovskite solar cells.

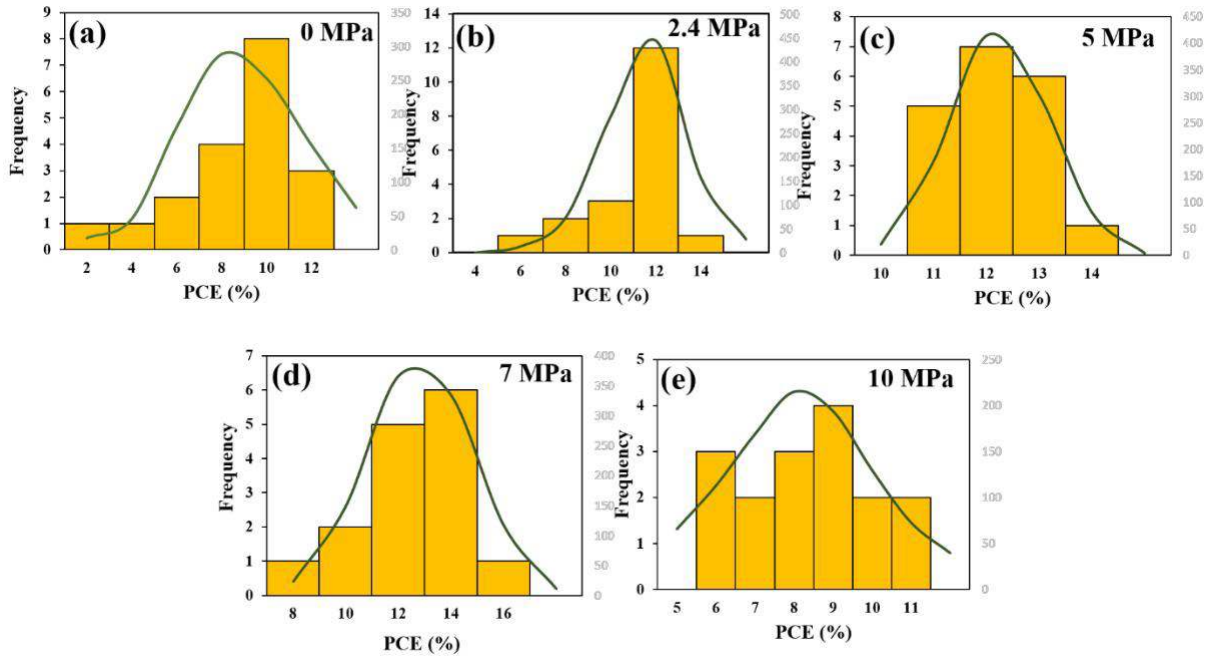

***Figure 3.11**. Histogram and normal distribution curves of the power conversion efficiencies of perovskite solar cells at different applied pressures (a) No pressure (0 MPa), (b) 2.4 MPa, (c) 5 MPa, (d) 7 MPa and (e) 10 MPa.*

The feasibility of the pressure-assisted fabrication technique was also demonstrated in devices with a large active area of 1.1 cm^2 for pressure of 7 MPa. **Figures** 3.12a and 3.12b present the J-V

curves and the steady-state PCEs of the large area devices under 1 sun illumination, respectively. The results showed that pressure application also enhances the PCE of the large active area devices (**Figures 3.**12a) from 8.26±0.21 % to 9.38±0.26 %. **Figure 3.**12a inset presents the picture of one sample of the devices with a large active area. The hysteretic behavior of these devices was studied at different scanning rates between 50 mV/s and 300 mV/s. **Figures 3.**12c – 3.12e present the J-V curves for both forward and reverse scanning directions at different scanning rates. The results showed that hysteresis loop decreases with increasing scanning rates (**Figures 3.**12c – 3.12e). The dependence of hysteresis on the scanning rates and direction of the J-V curves are associated with charge carrier collection efficiencies that strongly depend on built-in potential (Tress et al., 2015).

The above results show that the power conversion efficiencies of perovskite solar cells can be significantly improved by the application of pressure. This results in the closing of voids, and the corresponding increase in the interfacial surface contact lengths, which increases with increasing pressure (**Figures 3.**1 and 3.4). Hence, the improvement in the power conversion efficiencies that was observed with increased pressure (between 0 and 7 MPa) is attributed largely to the effects of increased surface contact and the compaction and infiltration of the TiO_2 layers with perovskite during the application of pressure.

The implications of the above results are significant for the design of a pressure-assisted process that can be used for the fabrication of perovskite solar cells. First, the significant effects of pressure suggest that pressure-assisted processes such as lamination (O. K. Oyewole et al., 2015), cold welding (Asare et al., 2016) and rolling/roll-to-roll processing can be used to fabricated perovskite solar cells with improved performance characteristics (photoconversion efficiencies, fill factors, short circuit currents and open circuit voltages). However, the applied pressures should be ~ 7 MPa or less, to ensure that the applied pressures do not induce layer damage and the excessive sink-in

of perovskite layer (between layers) (Jing Du et al., 2013). Hence, the combined effects of interlayer contact, mesoporous layer compaction and infiltration and the potential for layer damage at higher pressures must be considered in the optimized design of pressure-assisted processes for the fabrication of perovskite solar cells.

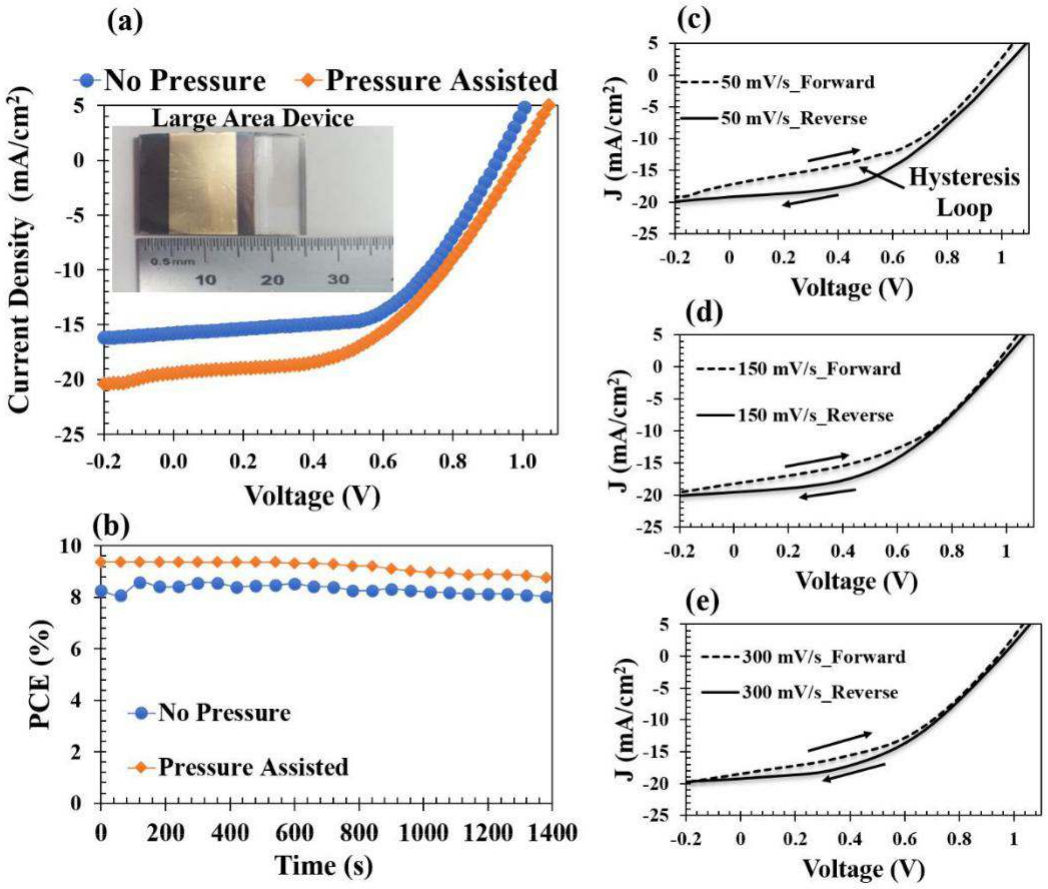

Figure 3.12. *(a) J-V curves of pressure-assisted fabricated devices, showing the picture of the device dimensions, (b) Steady-state PCEs of devices with large active areas under 1 sun illumination, and Hysteretic behavior of J-V curves of the devices with large active areas at scanning rates of (c) 50 mV/s, (d) 150 mV/s and (e) 300 mV/s.*

3.5. Conclusion

This paper presents the results of a combined analytical, computational, and experimental study of the effects of pressure on the performance of perovskite solar cells. The results show that the application of pressure results in improved interlayer surface contact, the compaction of mesoporous TiO_2 layers, and the infiltration of the mesoporous layers with perovskite for pressure up to 7MPa that also result in improved photoconversion efficiencies. However, at higher pressures ($p > 7$ MPa), the damage due to sink-in of the perovskite layers into the adjacent mesoporous layers results in reductions in the photoconversion efficiencies of perovskite solar cells.

3.6 References

Agyei-Tuffour, B., Rwenyagila, E. R., Asare, J., Oyewole, O. K., Zebaze Kana, M. G., O'Carroll, D. M., & Soboyejo, W. O. (2016). Influence of Pressure on Contacts between Layers in Organic Photovoltaic Cells. *Advanced Materials Research*, *1132*, 204–216. https://doi.org/10.4028/WWW.SCIENTIFIC.NET/AMR.1132.204

Akande, W. O., Cao, Y., Yao, N., & Soboyejo, W. (2010). Adhesion and the cold welding of gold-silver thin films. *Journal of Applied Physics*, *107*(4). https://doi.org/10.1063/1.3305791

Asare, J., Adeniji, S. A., Oyewole, O. K., Agyei-Tuffour, B., Du, J., Arthur, E., Fashina, A. A., Zebaze Kana, M. G., & Soboyejo, W. O. (2016). Cold welding of organic light emitting diode: Interfacial and contact models. *AIP Advances*, *6*(6). https://doi.org/10.1063/1.4955141

Ashby, L. J. G. and M. F. (1997). *Cellular Solids Structure and Properties*. Cambridge University Press.

Bietsch, A., & Michel, B. (2000). Conformal contact and pattern stability of stamps used for soft lithography. *Journal of Applied Physics*, *88*(7), 4310–4318. https://doi.org/10.1063/1.1289816

Campos, L. M., Truong, T. T., Shim, D. E., Dimitriou, M. D., Shir, D., Meinel, I., Gerbec, J. A., Hahn, H. T., Rogers, J. A., & Hawker, C. J. (2009). Applications of photocurable PMMS thiol-ene stamps in soft lithography. *Chemistry of Materials*, *21*(21), 5319–5326. https://doi.org/10.1021/cm902506a

Cao, Y., Kim, C., Forrest, S. R., & Soboyejo, W. (2005). Effects of dust particles and layer properties on organic electronic devices fabricated by stamping. *Journal of Applied Physics*, *98*(3). https://doi.org/10.1063/1.1994935

Chen, Q., Zhou, H., Hong, Z., Luo, S., Duan, H. S., Wang, H. H., Liu, Y., Li, G., & Yang, Y. (2014). Planar heterojunction perovskite solar cells via vapor-assisted solution process. *Journal of the American Chemical Society*, *136*(2), 622–625. https://doi.org/10.1021/ja411509g

Cho, K. T., Paek, S., Grancini, G., Roldán-Carmona, C., Gao, P., Lee, Y., & Nazeeruddin, M. K. (2017a). Highly efficient perovskite solar cells with a compositionally engineered perovskite/hole transporting material interface. *Energy and Environmental Science*, *10*(2), 621–627. https://doi.org/10.1039/c6ee03182j

Cho, K. T., Paek, S., Grancini, G., Roldán-Carmona, C., Gao, P., Lee, Y., & Nazeeruddin, M. K. (2017b). Highly efficient perovskite solar cells with a compositionally engineered perovskite/hole transporting material interfaceCho. *Energy & Environmental Science*, *10*(2), 621–627. https://doi.org/10.1039/C6EE03182J

Christians, J. A., Schulz, P., Tinkham, J. S., Schloemer, T. H., Harvey, S. P., Tremolet De Villers, B. J., Sellinger, A., Berry, J. J., & Luther, J. M. (2018). Tailored interfaces of unencapsulated perovskite solar cells for >1,000-hour operational stability. *Nature Energy 2017 3:1*, *3*(1), 68–74. https://doi.org/10.1038/s41560-017-0067-y

Doumon, N. Y., Rwenyagila, E. R., Asare, J., Oyewole, O. K., Shen, Z., Petoukhoff, C. E., Kana, M. G. Z., Ocarroll, D. M., & Soboyejo, W. O. (2017). *Pressure Effects on Interfacial Surface Contacts and Performance of Organic Solar Cells*. https://doi.org/10.1063/1.5001765

Du, J., Anye, V. C., Vodah, E. O., Tong, T., Zebaze Kana, M. G., & Soboyejo, W. O. (2014). Pressure-assisted fabrication of organic light emitting diodes with MoO3 hole-injection layer materials. *Journal of Applied Physics*, *115*(23). https://doi.org/10.1063/1.4881780

Du, Jing, Tong, T., Akande, W., Tsakiridou, A., & Soboyejo, W. (2013). Pressure effects on the lamination of organic light-emitting diodes. *IEEE/OSA Journal of Display Technology*, *9*(8), 601–606. https://doi.org/10.1109/JDT.2013.2253085

Dumond, J. J., & Yee Low, H. (2012). Recent developments and design challenges in continuous roller micro- and nanoimprinting. *Journal of Vacuum Science & Technology B, Nanotechnology and Microelectronics: Materials, Processing, Measurement, and Phenomena*, *30*(1), 010801. https://doi.org/10.1116/1.3661355

Fakharuddin, A., Jose, R., Brown, T. M., Fabregat-Santiago, F., & Bisquert, J. (2014). A perspective on the production of dye-sensitized solar modules. *Energy & Environmental Science*, *7*(12), 3952–3981. https://doi.org/10.1039/C4EE01724B

Feng, J. (2014). Mechanical properties of hybrid organic-inorganic CH3NH 3BX3 (B = Sn, Pb; X = Br, I) perovskites for solar cell absorbers. *APL Materials*, *2*(8).

https://doi.org/10.1063/1.4885256

Fina, M., Liu, D., Ren, L., & Mao, S. S. (2011). Improving organic light-emitting diode performance with patterned structures. *Applied Physics A: Materials Science and Processing*, *105*(2), 323–327. https://doi.org/10.1007/s00339-011-6616-5

Geissler, M., Wolf, H., Stutz, R., Delamarche, E., Grummt, U. W., Michel, B., & Bietsch, A. (2003). Fabrication of metal nanowires using microcontact printing. *Langmuir*, *19*(15), 6301– 6311. https://doi.org/10.1021/la034464x

Ghobadi, N. (2013). Band gap determination using absorption spectrum fitting procedure. *International Nano Letters*, *3*(1), 2–5. https://doi.org/10.1186/2228-5326-3-2

Grinberg, I., West, D. V., Torres, M., Gou, G., Stein, D. M., Wu, L., Chen, G., Gallo, E. M., Akbashev, A. R., Davies, P. K., Spanier, J. E., & Rappe, A. M. (2013). Perovskite oxides for visible-light-absorbing ferroelectric and photovoltaic materials. *Nature*, *503*(7477), 509–512. https://doi.org/10.1038/nature12622

Hur, S. H., Park, O. O., & Rogers, J. A. (2005). Extreme bendability of single-walled carbon nanotube networks transferred from high-temperature growth substrates to plastic and their use in thin-film transistors. *Applied Physics Letters*, *86*(24), 1–3. https://doi.org/10.1063/1.1947380

Jiang, S., Fang, Y., Li, R., Xiao, H., Crowley, J., Wang, C., White, T. J., Goddard, W. A., Wang, Z., Baikie, T., & Fang, J. (2016). Pressure-dependent polymorphism and band-gap tuning of methylammonium lead iodide perovskite. *Angewandte Chemie - International Edition*, *55*(22), 6540–6544. https://doi.org/10.1002/anie.201601788

Kim, B. C., & Forrest, S. R. (2003). *by Low-Pressure Cold Welding* **. *60*(6), 541–545.

Kim, J. H., Seo, S. M., & Lee, H. H. (2007). Nanovoid nature and compression effects in organic light emitting diode. *Applied Physics Letters*, *90*(14), 1–4. https://doi.org/10.1063/1.2720268

Kumar, M. H., Yantara, N., Dharani, S., Graetzel, M., Boix, P. P., & Mathews, N. (2013). Flexible, low-temperature, solution processed ZnO-based perovskite solid state solar cells. *Chemical Communications*, *49*(94), 11089–11091. https://doi.org/10.1039/c3cc46534a

Li, Y., Ji, L., Liu, R., Zhang, C., Mak, C. H., Zou, X., Shen, H. H., Leu, S. Y., & Hsu, H. Y. (2018). A review on morphology engineering for highly efficient and stable hybrid perovskite solar cells. *Journal of Materials Chemistry A*, *6*(27), 12842–12875. https://doi.org/10.1039/c8ta04120b

Liang, P. W., Liao, C. Y., Chueh, C. C., Zuo, F., Williams, S. T., Xin, X. K., Lin, J., & Jen, A. K. Y. (2014). Additive enhanced crystallization of solution-processed perovskite for highly efficient planar-heterojunction solar cells. *Advanced Materials*, *26*(22), 3748–3754. https://doi.org/10.1002/adma.201400231

Liu, G., Kong, L., Gong, J., Yang, W., Mao, H. K., Hu, Q., Liu, Z., Schaller, R. D., Zhang, D., & Xu, T. (2017). Pressure-Induced Bandgap Optimization in Lead-Based Perovskites with Prolonged Carrier Lifetime and Ambient Retainability. *Advanced Functional Materials*, *27*(3), 1604208. https://doi.org/10.1002/ADFM.201604208

Lü, X., Yang, W., Jia, Q., & Xu, H. (2017). Pressure-induced dramatic changes in organic-inorganic halide perovskites. *Chemical Science*, *8*(10), 6764–6776. https://doi.org/10.1039/c7sc01845b

Malinkiewicz, O., Yella, A., Lee, Y. H., Espallargas, G. M., Graetzel, M., Nazeeruddin, M. K., & Bolink, H. J. (2014). Perovskite solar cells employing organic charge-transport layers. *Nature Photonics*, *8*(2), 128–132. https://doi.org/10.1038/NPHOTON.2013.341

Noel, N. K., Abate, A., Stranks, S. D., Parrott, E. S., Burlakov, V. M., Goriely, A., & Snaith, H. J. (2014). Enhanced photoluminescence and solar cell performance via Lewis base passivation of organic-inorganic lead halide perovskites. *ACS Nano*, *8*(10), 9815–9821. https://doi.org/10.1021/nn5036476

Oyewole, O. K., Yu, D., Du, J., Asare, J., Anye, V. C., Fashina, A., Zebaze Kana, M. G., & Soboyejo, W. O. (2015). Lamination of organic solar cells and organic light emitting devices: Models and experiments. *Journal of Applied Physics*, *118*(7). https://doi.org/10.1063/1.4928729

Oyewole, Oluwaseun K. (2015). Effects of Adhesion and Deformation on Stretchable Electronic Structures. In *Phd Thesis submitted to African University of Science and Technology*.

Park, M., Kim, H. J., Jeong, I., Lee, J., Lee, H., Son, H. J., Kim, D. E., & Ko, M. J. (2015). Mechanically Recoverable and Highly Efficient Perovskite Solar Cells: Investigation of Intrinsic Flexibility of Organic–Inorganic Perovskite. *Advanced Energy Materials*, *5*(22), 1501406. https://doi.org/10.1002/AENM.201501406

Qiu, L., Ono, L. K., & Qi, Y. (2018). Advances and challenges to the commercialization of organic–inorganic halide perovskite solar cell technology. *Materials Today Energy*, *7*, 169–189. https://doi.org/10.1016/J.MTENER.2017.09.008

Reyes-Martinez, M. A., Abdelhady, A. L., Saidaminov, M. I., Chung, D. Y., Bakr, O. M., Kanatzidis, M. G., Soboyejo, W. O., & Loo, Y.-L. (2017). Time-Dependent Mechanical

Response of APbX3 (A = Cs, CH3NH3; X = I, Br) Single Crystals. *Advanced Materials*, *29*(24), 1606556. https://doi.org/10.1002/ADMA.201606556

Soboyejo, W. O. (2003). *Mechanical Properties of Enginneered Materials*. Marcel Dekker Inc.

Sun, S., Fang, Y., Kieslich, G., White, T. J., & Cheetham, A. K. (2015). Mechanical properties of organic-inorganic halide perovskites, CH3NH3PbX3 (X = I, Br and Cl), by nanoindentation. *Journal of Materials Chemistry A*, *3*(36), 18450–18455. https://doi.org/10.1039/c5ta03331d

Tai, Y.-L., Yang, Z.-G., & Li, Z.-D. (2011). A promising approach to conductive patterns with high efficiency for flexible electronics. *Applied Surface Science*, *257*(16), 7096–7100. https://doi.org/10.1016/j.apsusc.2011.03.056

Tan, J. C., & Cheetham, A. K. (2011). Mechanical properties of hybrid inorganic-organic framework materials: Establishing fundamental structure-property relationships. *Chemical Society Reviews*, *40*(2), 1059–1080. https://doi.org/10.1039/c0cs00163e

Tavakoli, M. M., Lin, Q., Leung, S. F., Lui, G. C., Lu, H., Li, L., Xiang, B., & Fan, Z. (2016). Efficient, flexible and mechanically robust perovskite solar cells on inverted nanocone plastic substrates. *Nanoscale*, *8*(7), 4276–4283. https://doi.org/10.1039/c5nr08836d

Tress, W., Marinova, N., Moehl, T., Zakeeruddin, S. M., Nazeeruddin, M. K., & Grätzel, M. (2015). Understanding the rate-dependent J-V hysteresis, slow time component, and aging in CH 3 NH 3 PbI 3 perovskite solar cells: The role of a compensated electric field. *Energy and Environmental Science*, *8*(3), 995–1004. https://doi.org/10.1039/c4ee03664f

W.M.Moreau. (1988). *Semiconductor Lithography Principle, Practices and Materials Plenum*.

Wan, K. T., & Mai, Y. W. (1995). Fracture mechanics of a shaft-loaded blister of thin flexible

membrane on rigid substrate. *International Journal of Fracture*, *74*(2), 181–197. https://doi.org/10.1007/BF00036264

Wang, Y., Lü, X., Yang, W., Wen, T., Yang, L., Ren, X., Wang, L., Lin, Z., & Zhao, Y. (2015). Pressure-Induced Phase Transformation, Reversible Amorphization, and Anomalous Visible Light Response in Organolead Bromide Perovskite. *Journal of the American Chemical Society*, *137*(34), 11144–11149. https://doi.org/10.1021/jacs.5b06346

Xiao, G., Cao, Y., Qi, G., Wang, L., Liu, C., Ma, Z., Yang, X., Sui, Y., Zheng, W., & Zou, B. (2017). *Pressure E ff ects on Structure and Optical Properties in Cesium Lead Bromide Perovskite Nanocrystals*. https://doi.org/10.1021/jacs.7b05260

Xiao, G., Zhu, C., Ma, Y., Liu, B., Zou, G., & Zou, B. (2014). Unexpected room-temperature ferromagnetism in nanostructured Bi 2Te3. *Angewandte Chemie - International Edition*, *53*(3), 729–733. https://doi.org/10.1002/anie.201309416

Yang, D., Yang, R., Wang, K., Wu, C., Zhu, X., Feng, J., Ren, X., Fang, G., Priya, S., & Liu, S. (Frank). (2018). High efficiency planar-type perovskite solar cells with negligible hysteresis using EDTA-complexed SnO2. *Nature Communications 2018 9:1*, *9*(1), 1–11. https://doi.org/10.1038/s41467-018-05760-x

Yang, W. S., Park, B. W., Jung, E. H., Jeon, N. J., Kim, Y. C., Lee, D. U., Shin, S. S., Seo, J., Kim, E. K., Noh, J. H., & Seok, S. Il. (2017). Iodide management in formamidinium-lead-halide-based perovskite layers for efficient solar cells. *Science*, *356*(6345), 1376–1379. https://doi.org/10.1126/SCIENCE.AAN2301/SUPPL_FILE/AAN2301_YANG.SM.PDF

Yang, Y., You, J., Hong, Z., Chen, Q., Cai, M., Song, T. Bin, Chen, C. C., Lu, S., Liu, Y., & Zhou, H. (2014). Low-temperature solution-processed perovskite solar cells with high efficiency

and flexibility. *ACS Nano*, *8*(2), 1674–1680. https://doi.org/10.1021/NN406020D/SUPPL_FILE/NN406020D_SI_001.PDF

Yuan, Y., Liu, X. F., Ma, X., Wang, X., Li, X., Xiao, J., Li, X., Zhang, H. L., & Wang, L. (2019). Large Band Gap Narrowing and Prolonged Carrier Lifetime of (C4H9NH3)2PbI4 under High Pressure. *Advanced Science*, *6*(15), 1–7. https://doi.org/10.1002/advs.201900240

Zhao, Q., Li, G. R., Song, J., Zhao, Y., Qiang, Y., & Gao, X. P. (2016). *Improving the photovoltaic performance of perovskite solar cells with acetate*. *December*, 1–10. https://doi.org/10.1038/srep38670

Chapter 4

UNDERSTANDING THE EFFECTS OF ANNEALING TEMPERATURE ON THE MECHANICAL PROPERTIES OF LAYERS IN FAI-RICH PEROVSKITE SOLAR CELLS

4.1. Introduction

Hybrid organic-inorganic perovskite (HOIPs) have emerged as promising energy-related materials for light absorbers in PV cells (Stranks & Snaith, 2015) and emitter in light-emitting diodes (LEDs) (Bade et al., 2015) lasers and photodetectors (Fu et al., 2016). The general formula of (HOIPs is ABX_3 where A = $CH_3NH_3^+$ (MA^+), $CH(NH_2)^{2+}$ (FA^+) or Cs^+ B = Pb^{+2} or Sn^{2+} and X = I^{-1}, Br^{-1} or Cl^{-1}. The efficiency of perovskite solar cells (PSCs) has increased dramatically above 25%(*Best Research-Cell Efficiency Chart | Enhanced Reader*, n.d.) over the past decade due to the novel electronic and optical (Mosconi et al., 2015), thermoelectric (Mettan et al., n.d.), and surface properties of the perovskite absorbers, scalable properties, low processing-temperature (Li et al., 2017), tunable and direct band gaps (Green et al., 2014) high extinction coefficients, high carrier mobility, low exciton binding energies and high absorption over a wide range of wavelengths (Grätzel, 2014). Perovskite materials also have potentials for wearable functional devices with great mechanical flexibility and robustness (Lee et al., 2019; Park et al., 2015). With the growing interest in HOIPs for deformable devices, the knowledge of their mechanical response to dynamic strain can adequately implement these materials on flexible and stretchable devices.

The understanding of the variations in the mechanical properties of HOIP structures that are processed at different annealing conditions is critical for ultimate device performance and

robustness. Annealing temperature influences the structure, morphology, crystallinity, and optoelectrical properties of perovskite films (L.-C. Chen et al., n.d.; Dualeh et al., 2014; Kim et al., 2017; Peng et al., 2016; Su et al., 2017; X et al., 2018). The annealing process is also critical in the formation of perovskite film and consequently on the power conversion efficiency of the assembled devices (Wehrenfennig et al., 2014). Increased annealing temperature can cause inter-diffusion and increased local stresses that can lead to the nucleation of cracks (Oyewole et al., 2021; Olanrewaju et al., 2021; Koech et al., 2021) and pin hole formation.

Although research into the electrical bands and exciton diffusion pathways has progressed quickly, only a few experimental and theoretical studies have been reported on mechanical properties (Feng, 2014; L. Ma et al., 2021; Rakita et al., 2015; Reyes-Martinez et al., 2017; S et al., 2017; Yu et al., 2016). The mechanical properties have an impact on the structural phase transition according to current studies of the production of flexible hybrid perovskite solar cells resistant to fatigue - material degradation and mismatch at interfaces, and the consequent lifetime (Kianoosh Poorkazem et al., 2015; Rakita et al., 2015). Several theoretical (Faghihnasiri et al., 2017; Yu et al., 2016) and experimental (Reyes-Martinez et al., 2017; S et al., 2017) calculations have been used to study the mechanical characteristics of organic-inorganic perovskites single crystals. Feng(Feng, 2014) has used the first-principle method to explore the mechanical characteristics of methylammonium halide perovskite. By monitoring nanoindentation creep and stress relaxation, Reyes-Martinez et al. (Reyes-Martinez et al., 2017) were able to determine the time- and rate-dependent mechanical characteristics of HOIPs and inorganic perovskite (IP) single crystals. However, a complete understanding of the mechanical properties of the HOIP films in nano/micro-scale as a function of the different annealing temperatures is yet to emerge. Several thermal annealing temperatures have been used to process perovskite solar cells (Dualeh et al.,

2014; Kim et al., 2017). It is, therefore, important to understand the mechanical robustness of these perovskite structures that are processed as different annealing temperatures. Motivated by the need to better understand the small-scale mechanical behaviors of HOIPs, nanoindentation experiments have been performed on perovskite structures to ascertain mechanical integrity and robustness.

In this paper, a combined experimental and theoretical approach is used to study micro- to nano-scale contacts in formamidinium-rich perovskite films that are relevant to applications in bendable and wearable perovskite solar cell devices. The perovskite films are processed at different annealing temperatures before relating their mechanical properties to performance characteristics. Contact-induced deformations and the indentation size effects (ISE) are then studied in the micro-and nano-scale regimes. The observed indentation size effects are explained by considering the role of geometrical necessary dislocations (GNDs) using the mechanism-based strain gradient (MSG) theoretical models by Nix and Gao (Gao et al., 1999), and Ma and Clarke(Q. Ma & Clarke, 2011). The intrinsic yield stress/hardness values, extracted from the MSG theory, are shown to exhibit a Hall–Petch dependence on grain size. Young's moduli are determined using the Oliver– Pharr (Oliver & Pharr, 1992) and Hay-Crawford (Hay & Crawford, 2011) methods that account for substrate effects. The implications of the results are then discussed for the design of robust PSCs.

4.2. Theory

A very comprehensive approach for the determination of the hardness and modulus from depth-sensing indentation load-displacement data was developed by Doerner and Nix (Doerner & Nix, 1986) and later by Oliver and Pharr (Oliver & Pharr, 1992) The definition of hardness, by Meyer was adopted in theory (Doerner & Nix, 1986). This is given by:

$$= \qquad \text{——} \tag{1}$$

where is the maximum load and is the projected contact area. The recorded load-displacement data were used to relate the stiffness, from the slope of the initial unloading curve to the reduced elastic modulus, :

$$= \qquad \frac{\sqrt{\quad}}{\quad} \frac{\quad}{\sqrt{\quad}} \tag{2}$$

where is the contact stiffness corresponding to the slope of load penetration curve at the beginning of the unloading, and is expressed in terms of the elastic moduli ( ) and Poisson's ratios ( ) of the indenter ( ) and the indented material ( ):

$$\frac{1}{} = \frac{1-\ _2}{} + \frac{1-\ ^2}{} \tag{3}$$

The projected contact area calibrated with the contact depth h is given by (Lou et al., 2003).

$$(h \qquad) = 24.5h^2 \qquad + h^1 + h^{1/2} \qquad + \cdots + h^{1/128} \tag{4}$$

where 1through 8 are constants.

After accounting for the tip rounding distance, ξ=0.75, for Berkovich indenter (Lou et al., 2003) and indentation pileup height h (Saha & Nix, 2002) the corrected contact area is calculated as follows:

$$(h\ )=24.5(h + \qquad +h\ )^2 + {}_1(h + \qquad +h\ )^1 + {}_2(h + \qquad +h\ )^{1/2} + \cdots +$$

$${}_8(h + \ + h\ )^{1/128} \tag{5}$$

Plasticity theories cannot be utilized to explain indentation size effects in submicron-thin films where the size effect is evident because no material length scales include the phenomenon. Theories on strain gradient plasticity (Fleck et al., 1994; Gao et al., 1999), are therefore necessary to explain the size effects. Nix and Gao (Nix & Gao, 1998) have developed a mechanism-based strain gradient (MSG) model to rationalize the indentation size effects. The model expresses the depth dependence of hardness as:

$$\frac{H^2}{H_0^2} = 1 + \frac{h^*}{h} \quad (6)$$

where H is the hardness for a given indent depth h, H_0 is the size independent hardness, and h^* is the characteristic length parameter that characterizes the depth dependence of the hardness. This model predicts that the hardness square is linear to the indentation depth reciprocal.

Nix and Gao (Nix & Gao, 1998) have also derived an intrinsic length scale ℓ from the MSG model to accommodate the indentation size dependence of hardness with the strain gradient:

$$\left(\frac{\sigma}{\sigma_0}\right)^2 = 1 + \frac{\eta\ell}{\gamma} \quad (7)$$

where σ is the effective flow stress in the presence of a gradient, σ_0 the flow stress in the absence of a gradient, the effective strain gradient and ℓ is a characteristic material length scale. Eq. (7) gives the physical meaning of this characteristic material length scale, ℓ that is a measure of the contribution of strain gradient to the flow stress.

ℓ can be expressed in terms of Burger's vector b and shear modulus μ as:

$$\ell = \frac{1}{\alpha^2}\left(\frac{\mu b}{\sigma_0}\right)^2 \quad (8)$$

The relative contributions of statistically stored dislocations (SSDs) and geometrically necessary dislocation (GNDs) were approximated with a model by Ma and Clarke using Taylor and Tabor relation (QUARRELL, 1952). The strain gradient is the average shear strain ϒ over an indentation size D (Q. Ma & Clarke, 2011). The density of GNDs, is given by (Ashby, 1970)

$$= \frac{4}{} \tag{9}$$

where ϒ is the average shear strain over an indentation size, D.

Hardness can, therefore, be estimated as:

$$\approx[+] \quad \frac{1}{} = [+ \quad \frac{1}{}]^2 \tag{10}$$

whereis the density of statistically stored dislocations (SSD), and is the density of geometrically necessary dislocations (GND). This model shows that the hardness is inversely related to the indent size, D.

Elmustafa et al. (Elmustafa et al., 2002) have shown that the Taylor hardening model of dislocation can simply be modified as

$$\frac{}{}^2 = \frac{}{} + \frac{1}{} \tag{11}$$

where $_1 = 2\sqrt{3}$ and $_2 = 4$.

The yield strength/stress, $_0$, is also affected by the grain size. The grain size dependence is given by the Hall-Petch relationship. The yield strength can be estimated from Tabor's relation (QUARRELL, 1952) which gives $_0 = 3 \ _0$. Hence, the Hall-Petch relationship (Callister & Rethwisch, n.d.) can be expressed as

$$= + \quad (12)$$

where $_{0}$ and are the intrinsic yield strength in the absence of grain size effects and material constant, respectively.

4.3. Materials and Methods

4.3.1. Materials

Etched Fluorine-doped Tin Oxide (FTO)-coated glass (~7 Ω sq^{-1}) was purchased from MSE Supplies, Tucson, AZ, USA. Lead iodide (PbI^2)(99.999%), di-isopropoxide bis(acetylacetone), Formamidinium iodide (FAI) (98%), methylammonium chloride (MACl), methylammonium bromide (MABr) (98%), dimethyformamide (DMF), dimethylsulfoxide (DMSO), titania paste, 1-butanol, ethanol, iso-propyl alcohol (IPA), 4-tert-butylpyridine (tBP), acetonitrile, lithium bis (trifluoromethylsulfonyl) imide (Li-TFSI), 2, 2', 7,7'-tetraksi (N,N-di-p-methoxyphenylamine)-9,9'-spirobifluorene (Spiro-OMeTAD), and anhhrous chlorobenzene were all purchased from Sigma Aldrich (Natick, MA, USA). All the materials were used there as received conditions.

4.3.2. Materials Processing

The etched FTO glasses were cleaned with detergent and deionized water. They were sonicated for 15 minutes successively in deionized water, acetone (Sigma-Aldrich), and IPA (Sigma-Aldrich). The cleaned glass substrates were blown to dry up in nitrogen gas and UV-ozone cleaning (Novascan, Main Street Ames, IA, USA) was used to remove the organic residues.

According to the preceding protocol (Oyelade et al., n.d.), the electron transporting layer (ETL) made of the titanium layers compact (c-TiO_2) and mesoporous (m-TiO_2) was deposited on the FTO glasses. The compact titanium oxide (c-TiO_2) was spin coated onto the cleaned FTO glass from a

0.15M solution of titanium diisopropoxide bis(acetylacetone) in 1-butanol at 2000 rpm for 30 s. This was then annealed at 150^{o}C for 5 minutes before spin coating a 0.3M solution of titanium diisopropoxide bis(acetylacetone) in 1-butanol at 2000 rpm for 30 s. The deposited c-TiO_2 was then sintered in a furnace (Linberg Blue M, Thermo Fisher Scientific) at 500^{o}C for 30 minutes. When the layer cooled down to room temperature, a mesoporous titanium oxide (from a mixture of titania paste and ethanol in ratio 1:5 (w:w)) was spin coated onto it at 4000 rpm for 30 s and sintered at 500^{o}C for 1 hour in the furnace (Linberg Blue M, Thermo Fisher Scientific). A mixture of 0.5993 g of PbI_2 and DMF:DMSO (9.5:0.5; v:v) was used to prepare lead iodide solution which was stirred at 500 rpm for 2 hours at 60^{o}C heating temperature. The mixture was filtered through a 0.45 μm mesh before spin coating onto the mesoporous TiO_2 at 1500 rpm for 30 s. The film was annealed at 70 ^{o}C for 1 minute and allowed to cool down to room temperature.

The formamidinium iodide-rich (FAI-rich) organic solution was then prepared from 60 mg of FAI, 6 mg of MABr, and 6 mg of MACl in 1 ml of IPA. The solution was spin coated onto the PbI_2 layers at 1300 rpm for 30 s. The films were annealed at various temperatures (80, 100, 130, 150 and 170^{o}C) to form the perovskite layer. Some of the annealed perovskite films were set aside for characterization, while a hole transport layer (HTL) was spin coated on the films for PSC devices.

The HTL was prepared by first dissolving 260 mg of Li-TFSI in 1 ml of acetonitrile. Then 72 mg of Spiro-OMeTAD was dissolved in 1 ml of chlorobenzene before adding 30 and 35 µl of tBP and Li-TFSI solutions, respectively. The mixture was sonicated for 5 minutes, and spin coated on to the perovskite films at 4000 rpm for 30 s. Finally, a 90 nm thick layer of gold was thermally evaporated onto the films using an Edward E306A thermal evaporator (Edward E306A, Easton PA, USA). The evaporation was carried out at a vacuum pressure of ~1 x 10^{-6} Torr and a deposition rate of 0.2 nms^{-1}. A shadow mask of 0.12 cm^2 was used to define the area of the device.

Nanoindentation tests were carried out using KLA iMicro nanoindentation testing system (Nanomechanics, Inc., Oak Ridge, Tennessee), a universal nanomechanical in situ testing platform powered by the InForce 1000 electromagnetic actuator and capacitive displacement sensor. An Avantes UV-vis spectrophotometer (Avantes, BV, USA) was used to measure the optical absorbance of the perovskite films that were annealed at different temperatures. The microstructures of the top surfaces and cross sections of the films were observed under a field emission gun scanning electron microscope (SEM) (JSM 7000F, JOEL Ltd., Tokyo, Japan). The surface topographies of the films were examined using atomic force microscope (AFM) (-NX 20 Park Systems, Santa Clara, CA, USA). An X-ray diffractometer (Malvern PANalytical, Westborough, MA, USA) was used to obtain the XRD patterns of the perovskite film under a Cu K_α radiation source with Beta Nickle filter at 40 KV and 40 mA.

For all the perovskite solar cells (PSCs) devices produced at different annealing temperatures, the current density-voltage curves were measured using a Keithley source meter unit 2400 system (Keithley, Tekronix, Newark, NJ, USA) connected to an Oriel solar simulator (Oriel, Newport Corporation, Irvine, CA, USA). The devices were exposed to AM 1.5G illumination of 100 $mWcm^{-2}$ during the current density-voltage measurements. The solar simulator was calibrated using a calibrated silicon cell (91150 V silicon reference cell, Newport).

4.3.3. Nanoindentation Experiments

To measure the mechanical properties of the perovskite films, indentation tests on fused silica were performed to acquire the area function calibration. The calibrating method assumes that Young's modulus of elasticity is unaffected by indentation depth (Oliver & Pharr, 1992). For silica used in the calibration experiment, $= 68.6$. The elastic modulus for the Berkovich indenter is 1140 GPa. The Poisson's ratios for the silica and the indenter are 0.17 and 0.07, respectively. A

projected contact area was estimated for each indent using Eq. (2). The computed area was then plotted against contact depth (**Figure** 4.1) and a fitting procedure was employed to fit the versus h to a polynomial from Eq. (5). Using this approach, the coefficients 1 through 8 have been calibrated for the Berkovich indenter used in the current study. After the calibration, nano-indentation experiments were performed on the perovskite films annealed at 80, 100, 130, 150, and 170 ^{o}C.

The nanoindentation experiments were carried out with the iMicro, a universal nanomechanical in situ testing platform powered by the InForce 1000 electromagnetic actuator and capacitive displacement sensor (Nanomechanics, Inc., Oak Ridge, Tennessee) using the Dynamic CSR for Thin Films test method. The indenter used was a diamond Berkovich indenter with tip radius of 20 nm. The indenter was brought into contact with the film at a speed of 100 nm/sec and surface approach distance of 2000 nm. While oscillating at a frequency of 100 Hz with an amplitude of 1 nm, the indenter was driven into the film's surface at a strain rate of 0.2/sec to 40 percent of the film thickness. At least 64 experimentally valid indentations were done per sample using a separation of 60 μm between two adjacent indentation sites to reduce the possibility of indentation interactions. For each indent, a load–displacement curve was recorded.

In this analysis, the Berkovich diamond indenter properties and used are 1140 GPa and 0.07 respectively. The film's substrate has been shown to have a considerable impact on estimates of the Young's modulus obtained using nanoindentation (Doerner & Nix, 1986). The film-substrate model by Hay and Crawford was used to eliminate the effects of the FTO glass substrate on the perovskite films. The model's inputs include the film thickness, Poisson's ratio of the film, and the substrate's elastic characteristics. The input values used in this work are as

follows: h $= 500$, $= 0.33$, $= 105$, and $= 0.4$.

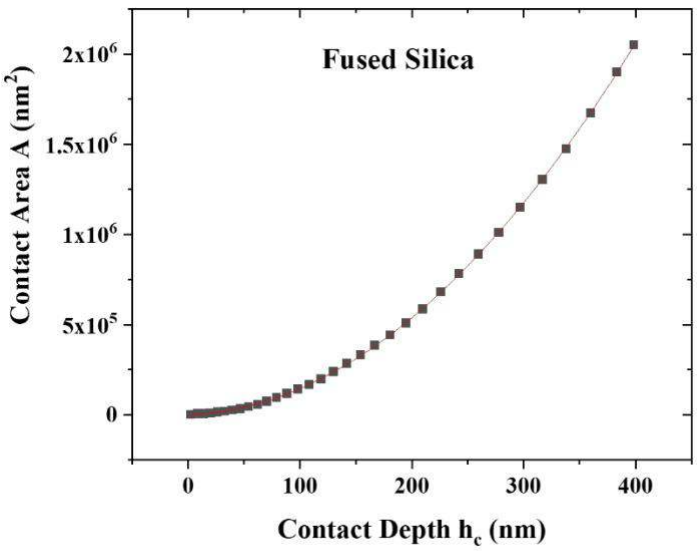

Figure 4.1. *The computed projected contact area as a function of contact depth* h *with a polynomial fit*

4.4. Results and Discussion

4.4.1. Microstructure of Perovskite Films

The perovskite films were processed and observed under SEM. **Figures** 4.2(a) - 4.2(e) present the SEM microstructural images of the perovskite film annealed at 80^{o}C and 170^{o}C. We estimated the grain size values from SEM images of several perovskite films that were processed at different annealing temperatures. The SEM images were analyzed using ImageJ software (Image J, National Institutes of Health, Bethesda, MD, USA). The average roughness values were estimated from AFM images that were analyzed using a Gwyddion software. To the best of our knowledge, the values were obtained accurately. The results show that the size of the grain increases with

increasing annealing temperature. Similar trends have been reported in prior work (L.-C. Chen et al., n.d.; Oyewole et al., 2021).

The average grain size estimated increased from 493.0 ± 135.4 nm to 1616.0 ± 457.3 nm, as the annealing temperature increased from 80 to 170 ^{o}C. The estimated grain size is summarized in **Table** 4.1. A smooth compact perovskite film layer was obtained as the annealing temperature increased to 130^{o}C (**Figures** 4.2(b) - 4.2(c)). Lower annealing temperature (80 ^{o}C) yielded rough films with pinhole-like defects (**Figure** 4.2(a)). For the films annealed at higher temperature, the film rapidly crystallizes to form larger grains (**Figures** 4.2(d) - 4.2(e)) which resulted in formations of defects (void and cracks) along the grain boundaries (**Figure** 4.2(e)).

Large and irregularly shaped plate-like grains were observed in perovskite films annealed at 150 ^{o}C. The films were also rougher and had bigger grain sizes than those observed in perovskite films annealed at lower temperatures. Larger grains with voids between them were also observed in the films annealed at 170 °C. The rapid growth of grains from a few nucleation sites was also associated with void formation (Oyewole et al., 2021), and significant reductions in solar cell performance.

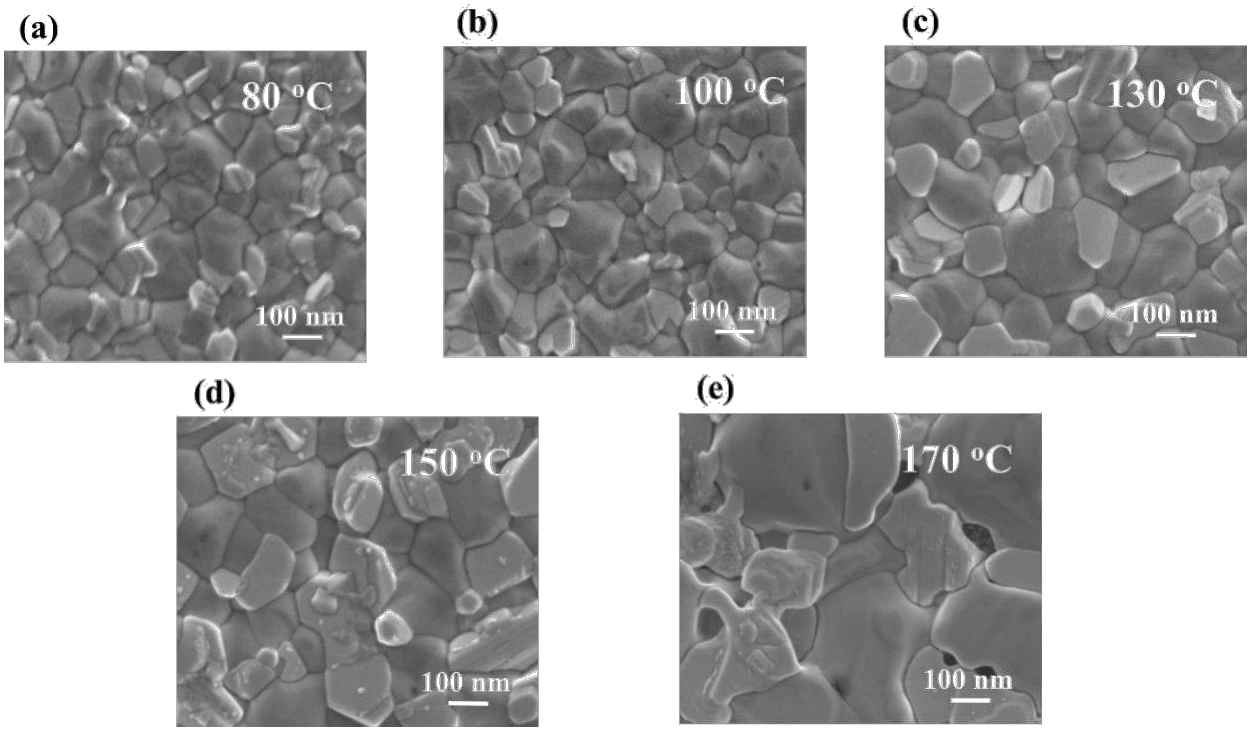

Figure 4.2. *(a)-(e) SEM images of perovskite layers annealed at (a) 80 ^{o}C (b) 100 ^{o}C (c) 130 ^{o}C (d) 150 ^{o}C (e) 170 ^{o}C*

Table 4.1. *Grain size d and surface roughness values*

Temp (^{o}C)	Grain Size d (nm)	Surface Roughness (nm)
80	493.1 ± 135.4	41.3 ± 3.0
100	515 ± 154.5	35.8 ± 0.5
130	677 ± 206.2	38.0 ± 2.5
150	808 ± 228.3	40.4 ± 3.1
170	1616 ± 457.3	73.7 ± 8.0

Contact mode atomic force microscopy (AFM) was used to characterize the surface roughness of the perovskite films. Typical AFM images of the films annealed at different temperatures between

80 – 170 ^{O}C are presented in **Figure** 4.3. The 3D orientations of the AFM images are presented in **Figure** 4.4. The AFM images show the equiaxed grain structures in the deposited films. The surface roughness data that were obtained for the perovskite films are summarized in **Table** 4.1. The results showed that the average surface roughness values of the films annealed at a very high temperature are higher, indicating the presence of large pin holes and grain boundary voids (**Figure** 4.2(e)). The results are consistent with prior studies of film microstructure which show that surface roughness increased with annealing temperature (J.-Q. Chen et al., 2019).

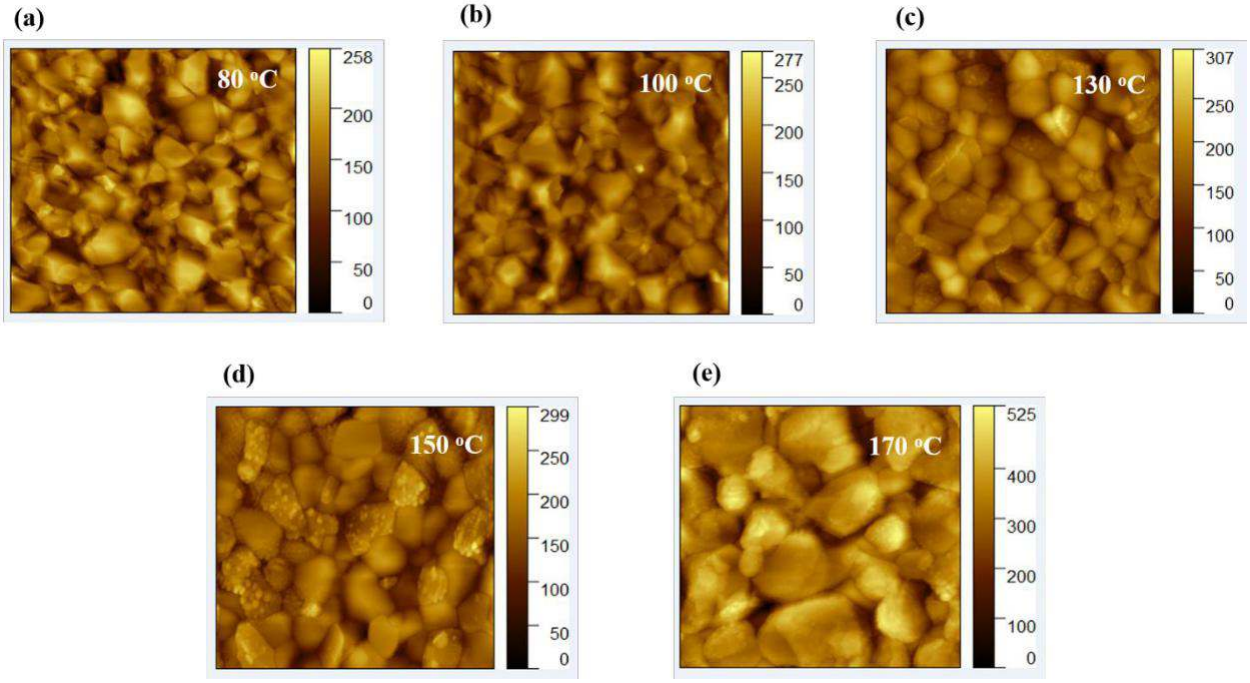

Figure 4.3. *Typical AFM images of the perovskite films annealed at (a) 80 ^{O}C, (b) 100 ^{O}C, (c) 130 ^{O}C, (d) 150 ^{O}C and (e) 170 ^{O}C.*

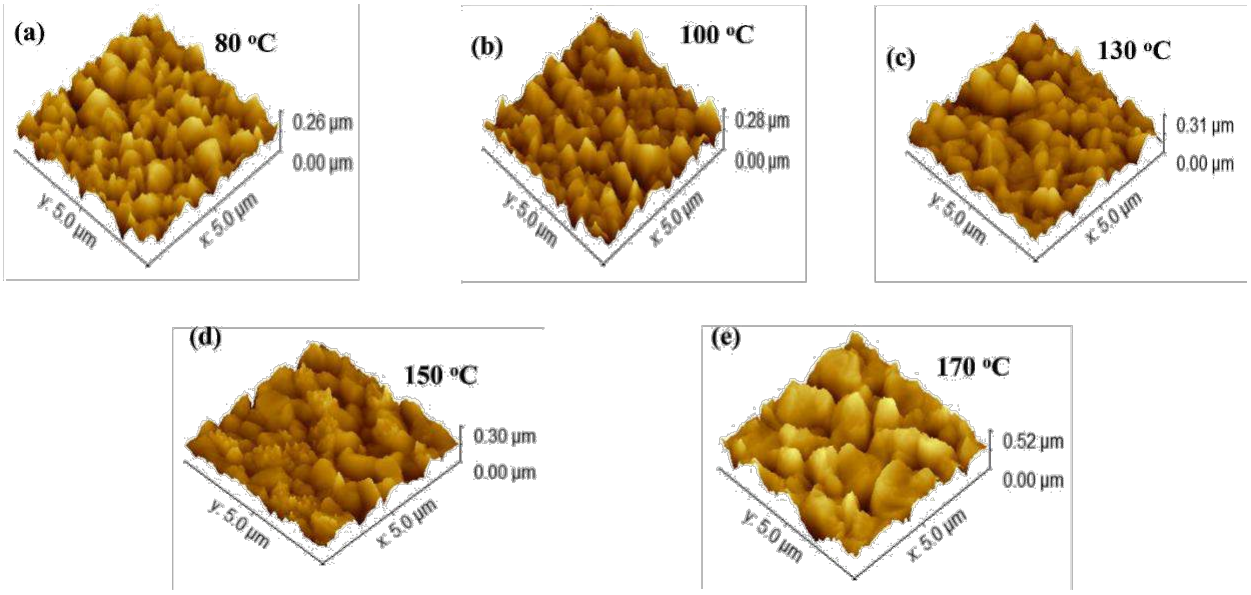

Figure 4.4. *The 3D orientations of the AFM images of the films annealed at (a) 80 ^{o}C (b) 100 ^{o}C (c) 130 ^{o}C (d) 150 ^{o}C (e) 170 ^{o}C*

4.4.2. Mechanical Properties of Perovskite Films

The Young's moduli and hardness of the perovskite films annealed at different temperatures are summarized in **Table** 4.2. The hardness values for films annealed between 80 to 130 ^{o}C is approximately 0.82 GPa. The hardness values for the films annealed above 130 ^{o}C decreased to 0.75 and 0.54 GPa for films annealed at 150 ^{o}C and 170 ^{o}C. The hardness values decrease with increasing temperature to 150 ^{o}C. This is attributed to interactions between dislocations and more widely spaced grain boundaries that occur at temperatures up to 150 ^{o}C. However, above 150 ^{o}C, the occurrence of recrystallization (smaller grains) and micro-voids results in a reduction of hardness after annealing at higher temperatures (Oyewole et al., 2021; Sha et al., 2014; Tong et al., 2015).

The Young's modulus value slightly increased from 12.4 to 13.2 GPa for films annealed between 80 to 130 ^{o}C and decreased to 12.6 and 10.4 GPa for films annealed at 150 ^{o}C and 170 ^{o}C. The

representative load-displacement curves for the film annealed at different temperatures are shown in **Figure** 4.5(a). Plots of Young's modulus versus depth obtained for each of the perovskite films annealed between 80 - 170 ^{o}C are presented in **Figures** 4.6(a) - 4.6(e). The obtained Young's moduli of 10.4 – 13.2 GPa and hardness values of 0.54 – 0.83 GPa are in reasonable agreement with prior reports (S et al., 2017). Ma et al. (L. Ma et al., 2021) have also presented Young's moduli and hardness values of 11.5 – 19.2 GPa and 0.047 – 0.63 GPa, respectively.

4.4.3. Indentation Size Effects

Figure 4.5(b) presents the contact depth dependence of hardness obtained for all the perovskite films annealed at different temperatures. Indentation size effects (ISE), a phenomenon in which the measured hardness values increase with decreasing indentation depth, was observed in all the films tested. This is because of the effects of geometrically necessary dislocations at a small scale(Gao et al., 1999). The hardness values increase at both the micro and nano scales as the indentation depth reduces (**Figure** 4.5(b)). The level of the increase at the nanoscale, however, is much more than that at the microscale. The ISE for films annealed at the different annealing temperatures is presented in Figures **Figure** 4.7(a) - 4.7(b), while the representative images of the indents are presented in **Figures** 4.8(a) - 4.8(c). The indents are typically on grains within the perovskite films (**Figures** 4.8), with pile up occurring in some cases **Figure** 4.8(c).

Table 4.2. *Summary of the Young's modulus and hardness values for perovskite films annealed at different temperatures*

Temp (^{o}C)	E (GPa)	H (GPa)
80	12.4 ± 1.1	0.822 ± 0.103
100	12.9 ± 1.3	0.813 ± 0.107
130	13.2 ± 1.2	0.828 ± 0.112
150	12.6 ± 1.5	0.751 ± 0.146
170	10.4 ± 1.7	0.54 ± 0.144

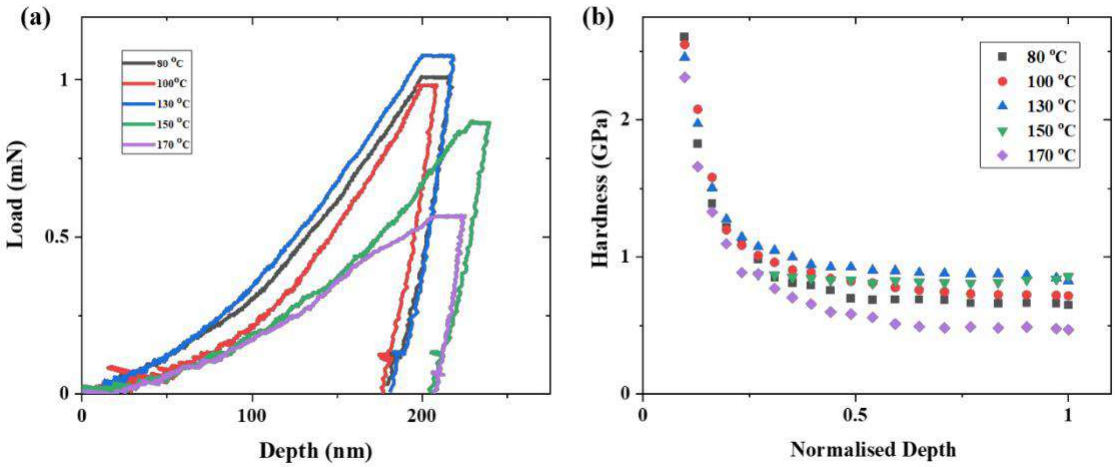

Figure 4.5. *(a) The load-displacement curves for the film annealed at different temperatures and (b) Hardness-depth curves*

To relate the indentation size dependence of hardness to the strain gradient, the intrinsic material length scale ˆ was calculated using a mechanism-based strain gradient (MSG) model (Eq. 8). The shear modulus value of 6.37 GPa (Lei Guo(郭磊), 2019) and Burger's vector 0.2995 nm were

used. The characteristic length scale $\hat{}$ of the material measures how much the stress gradient contributes to the plasticity. The intrinsic length scales for the films at different annealing the temperatures are summarized in **Table** 4.3.

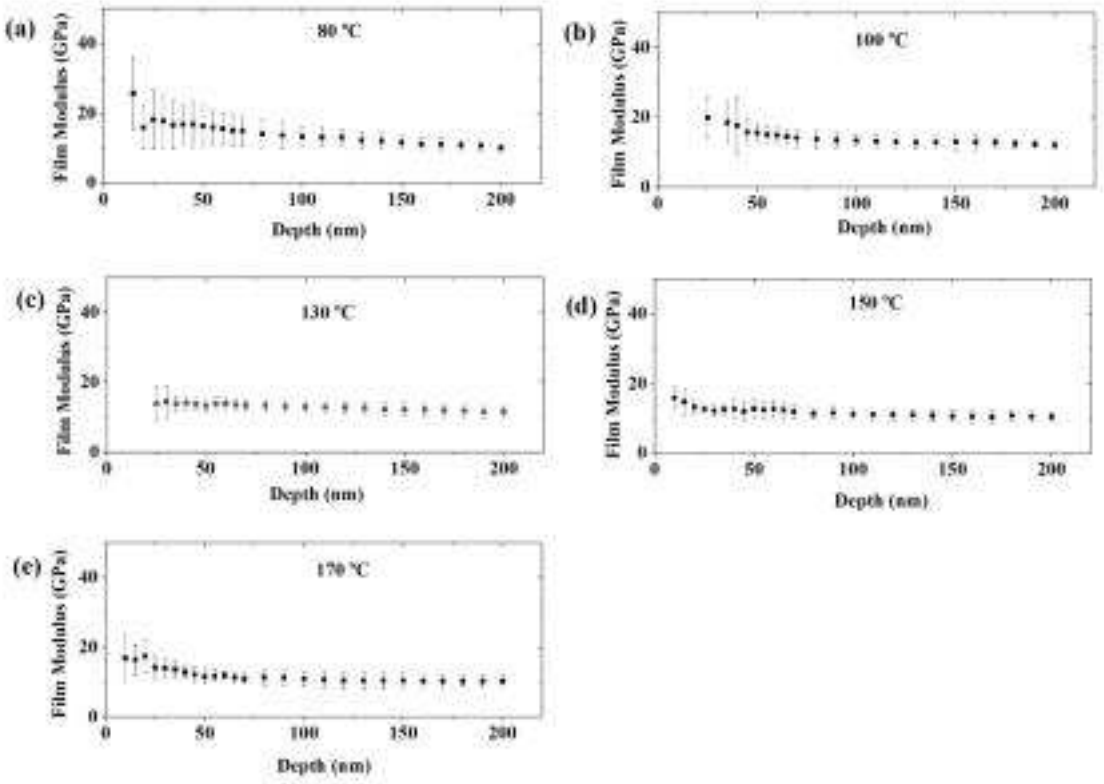

Figure 4.6. *Film modulus versus depth for perovskite films annealed at (a) 80^{o}C (b) 100^{o}C (c) 130^{o}C (d) 150^{o}C (e) 170^{o}C*

Micro length scales between 2.97 - 4.52 μm and nano length scales between 2.68 – 6.59 μm were obtained for annealing temperatures between 80 – 150 ^{o}C. In the case of the films prepared at 170 ^{o}C annealing temperature, 360.89 μm and 34.94 μm of micro and nano length scales were obtained, respectively. The values obtained are close to the value range of 1.15 – 6.51 μm reported by Z. Zong et. al for the nanoscale (Z. Zong et al., 2006) as well as ~ 12 and 6 μm, respectively, reported

for annealed copper and work-hardened copper by Nix and Gao (Nix & Gao, 1998). The measured

values of $\hat{}$ decreased as the annealing temperature increases. Larger values of $\hat{}$ indicate greater spacing between statistically stored dislocations. This could lead to weaker dislocation interactions and lower intrinsic strengthening of films annealed at higher temperatures.

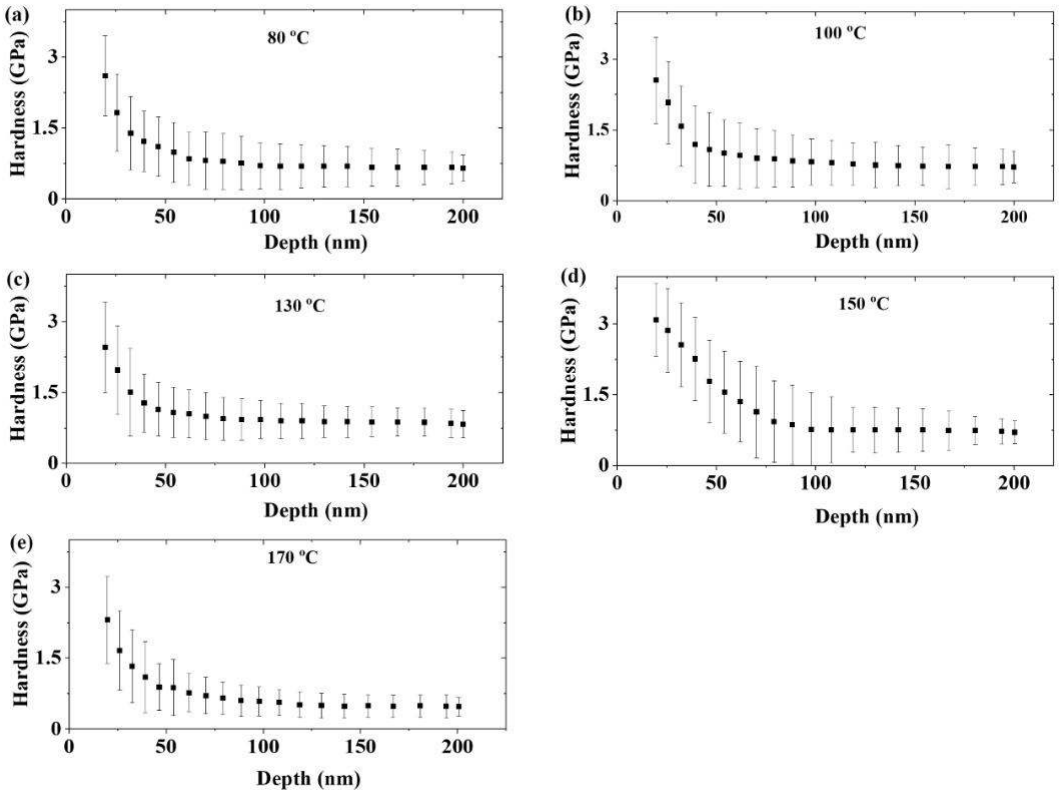

Figure 4.7. *The indentation side effect (ISE) of films annealed at (a) 80 ^{o}C (b) 100 ^{o}C (c) 130 ^{o}C (d) 150 ^{o}C (e) 170 ^{o}C*

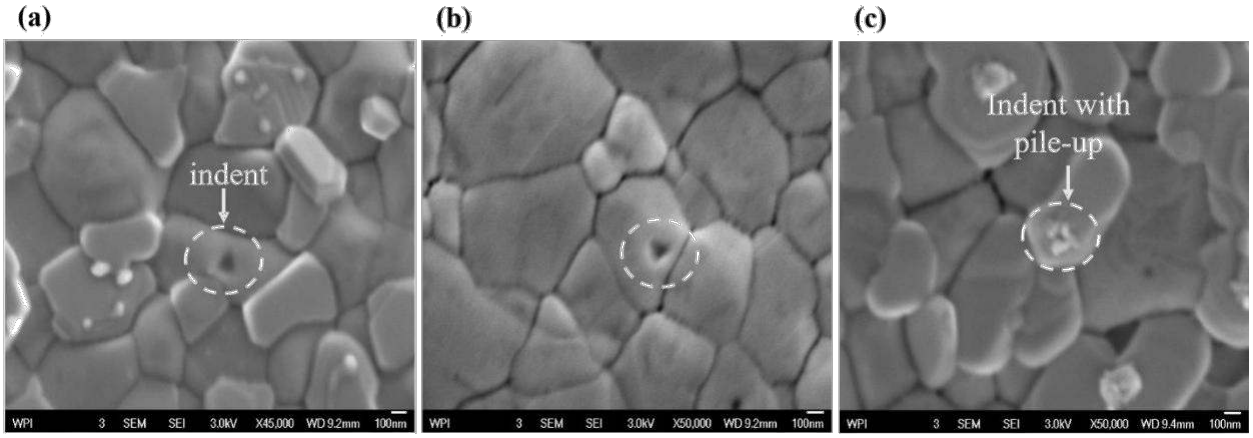

Figure 4.8. *(a) and (b) Typical indents on grains of the perovskite films (c) Indent with pile up*

The density of geometrically necessary dislocations (GNDs), was computed from Eq. (9) and the hardness values were estimated from Eq. (10). This model shows that the square of hardness is inversely related to the indent size, D. The values of the density of statistically stored dislocations (SSDs) and shear strain ϒ were obtained by fitting the experimental data into Eq. (10). The estimated values of : 108 – 197 μm^{-2}, : 0.6 – 1.9 μm^{-2} and ϒ: 13.1 – 21.1 % that were obtained for the different annealing temperatures are summarized in **Table** 4.4. Similar values of 389 – 543 μm^{-2} for and 10 – 21% for ϒ have been reported in prior studies for single crystal metals by Zong et al. [44]. The plots of versus the inverse of the indentation depth D^{-1}, within the nanoscale, are presented in **Figure** 4.9(a) for perovskite films annealed at different temperatures.

***Table** 4.3. Micro and Nano length scales for the different annealing temperatures*

Temp (^{o}C)	Micro-scales l (μm)	Nano-scales (μm)
80	4.52	6.59
100	3.77	3.85
130	1.80	1.72
150	2.97	2.68
170	360.89	34.94

The density of GNDs increases with decreasing indentation depth. Since the SSDs varied slightly in the films annealed at different temperatures, an explanation for the size effect is that the increase in is connected to the increasing strain gradients at small scales. The increased hardness is due

to the increased interactions between the closer spaced GNDs at small scales. These interactions cause hardening and strong indentation size effects in the nano and micro scales. Other researchers have reported similar indentation size dependence on hardness (Cao et al., 2006; Greer & Nix, 2005; Nix & Gao, 1998; Zong Zong & Soboyejo, 2005). The difference in the curve for 80^{o}C Figure 4.9(a) compared to the rest of the annealing temperatures can be associated with texture and crystallinity of the films.

Table 4.4. *Estimates of average shear strain, GNDs and SSDs densities*

Temp ^{o}C	ρ_S (μm^{-2})	ρ_G x 10^5 (μm^{-2})	Υ (%)
80	108.5	1.85	18.7
100	126.8	1.81	19.9
130	196.6	1.89	20.1
150	142.7	1.54	21.5
170	141.8	0.63	13.1

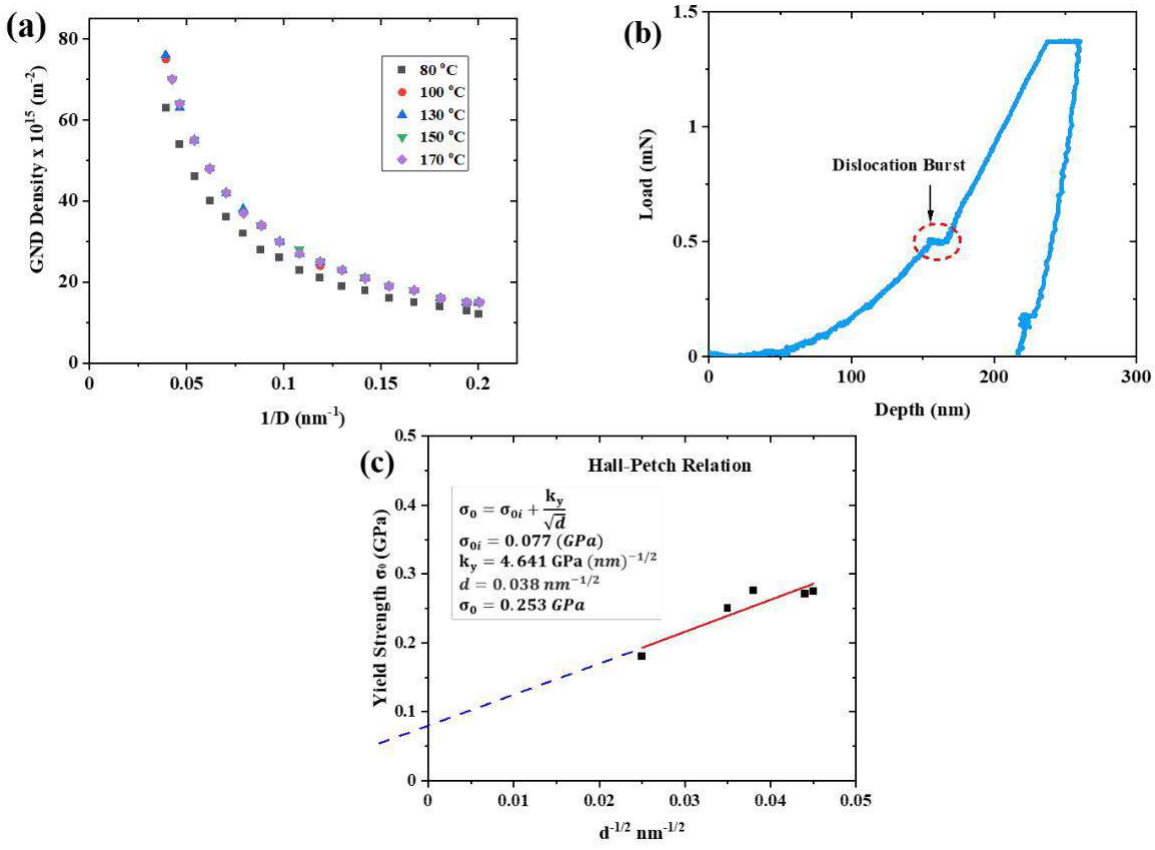

Figure 4.9. *(a) Plots of GND density versus inverse of the indentation depth D^{-1}, (b)*

Dislocation burst on load-displacement curve of perovskite film annealed at 80°C and (c) Plot of $_0$ versus $d^{-1/2}$ with linear fit for perovskite films annealed at different temperatures

A plot of the square of hardness against the reciprocal of the indentation depth in Eq. (11) gives a linear relationship for data at both micro- and nano-scales (**Figure** 4.10(a) - 4.10(e)), but with different slopes for the micro-hardness and nano-hardness data. The results in the nano- and micro-scales constitute a bi-linear indentation size behavior (Elmustafa et al., 2002). For an average indentation size of 100 nm in the nanoscale for the 80^{o}C annealing temperature, the density for GNDs calculated from Eq. (9) is ~2.4 x 10^{16} m^{-2}. At the micro- scale, for an average indentation size of 100 μm, the density for GNDs calculated is ~2.4 x 10^{13} m^{-2}. Hence, the average dislocation spacing ($= 1/\sqrt{}$) for film annealed at 80°C is ~6.45 nm for nano-indentation of ~ 100 nm and ~ 0.204 μm for micro-indentation size of 100 μm.

Consequently, only relatively few GNDs rows are introduced into the deformed regions for an indentation size of ∼100 nm. Multiple dislocations must be initiated to compensate for this dislocation source limited conditions. At such dislocation starved conditions, very high stresses nucleate new dislocations, leading to the observed high strengths (Greer & Nix, 2005) Furthermore, the discrete displacement bursts found during the initial period of nano-indentation in perovskite films are possible evidence of nucleation dislocations (Zong Zong & Soboyejo, 2005). Typical displacement dislocation burst is seen in the film annealed at 80^{o}C (**Figure** 4.9(b)).

At the micro-scale indents, however, there is an established dislocation substructure under the indent. It is assumed that this has a different plasticity length scale in the micro-scale. Hence, the bi-linear behavior is evidence of the differences in the source limited dislocation structures of indentation at the nanoscale and the deformation by established dislocation structures at the sub-

micro and micro scales. The different deformation mechanisms also account for the differences in the length scale$^{\wedge}$ values at the nano and micro scales.

The film grain size was related to the intrinsic film strength/hardness in the absence of strain gradient plasticity (SGP) phenomena. Figure 4.9(c) shows the experimental data of $_0$ versus $d^{-1/2}$ as well as the corresponding linear fit based on Eq. (12). $_0$ is linearly related to $d^{-1/2}$. The values of and $_0$ (obtained using linear fitting for perovskite film) are 4.64 GPa $(nm)^{-1/2}$ and 0.077 GPa, respectively.

The calculated intrinsic yield strengths for the perovskite films annealed between 80 to 170^{o}C are presented in **Table** 4.5. The intrinsic yield strength increases as the annealing temperature increases. This is attributed to the reduction in the grain boundary obstacles per unit volume that occurs with increasing grain sizes at higher annealing temperatures. However, for annealing temperatures between 150 and 170 ^{o}C, the intrinsic yield strength decreased due to the effects of recrystallization and microvoid formation (Schneider et al., 2019; Sha et al., 2014; Yu et al., 2016). Yield strength values of 0.133-0.181 GPa have been previously reported for $MAPbI_3$ (Yu et al., 2016).

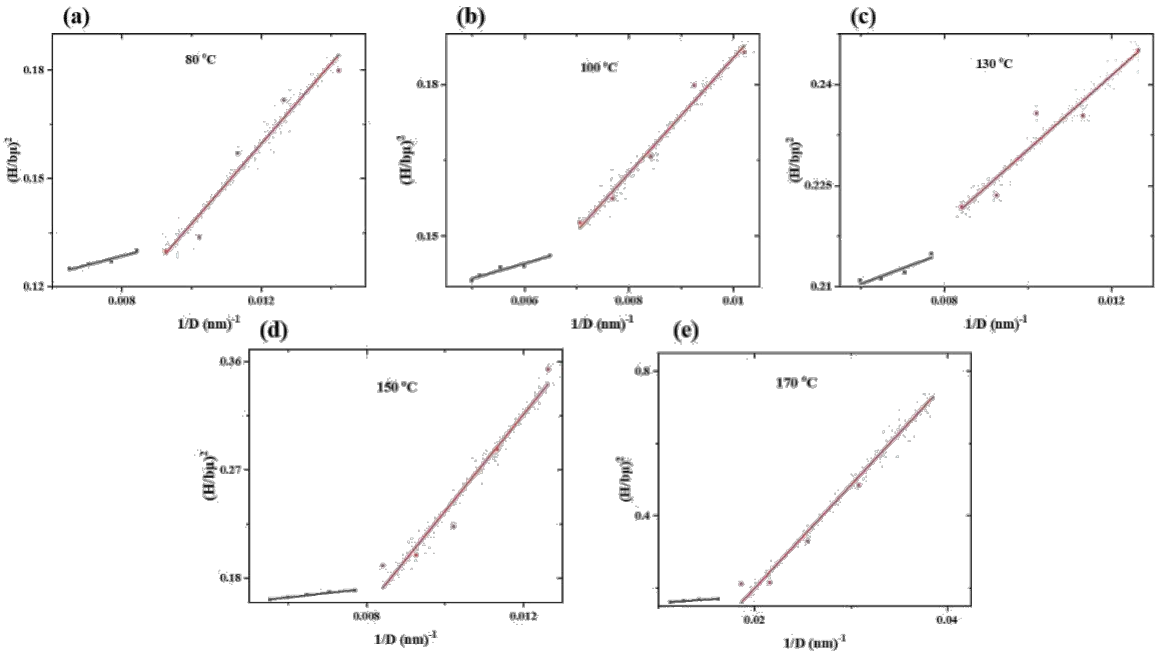

Figure 4.10. *Bi-linear behavior from micro-to nano-scale for perovskite films annealed at (a) 80 ^{o}C (b) 100 ^{o}C (c) 130 ^{o}C (d) 150 ^{o}C (e) 170 ^{o}C. The red line is the micro-scale region while the black line is the nano-scale region.*

Table 4.5. *Yield strength of film annealed at different temperatures*

Temp(^{o}C)	$d^{-1/2}$ $(nm)^{-1/2}$	σ_0 GPa
80	0.045	0.271
100	0.044	0.274
130	0.038	0.276
150	0.035	0.25
170	0.025	0.18

4.4.4 Optical and structural properties

The absorption spectra are presented in **Figure** 4.11(a) for the perovskite films that are prepared at different annealing temperatures. The absorption increases with increasing annealing temperature from 80 to 130 ^{o}C **Figure** 4.11(a) (top)) while the light absorption is reduced as the annealing temperature is raised further from 150 to 170 ^{o}C **Figure** 4.11(a) (bottom)). The increase in the absorbance, for the films annealed between 80 – 130 ^{o}C, is associated with the increased grain size (**Table** 4.1). The increase in the grain size is due to tensile strain in the film which can, therefore, lead to compressive strain along the grain boundaries due to the increasing annealing temperature from 80-170 ^{o}C. The observed decrease in the absorbance peaks for the films annealed at 150 and 170 ^{o}C is associated with the initiation of grain boundary cracks (**Figure** 4.2 (e)) which is driven by the strains along the grain boundaries. The tensile strains in the perovskite films have been presented earlier (Oyewole et al., 2021) for different annealing temperatures.

To further elucidate the effects of annealing temperature on the structure and crystallinity, we used X-ray diffractometer (XRD) to produce X-ray diffraction patterns of the perovskite films **Figure** 4.11(b) presents the XRD patterns of the samples. The results show that the films have strong and sharp diffraction peaks, indicating high crystallinity for the cubic perovskite phase. The crystallinity of the samples increased as the annealing temperature increased from 80 to 130 ^{o}C as shown by the strong and sharp diffraction peaks. At higher temperatures between 150 and 170^{o}C, the crystallinity of the samples reduces, as evident in the reduced diffraction peaks (**Figure** 4.11(b)). The diffraction peak at a 2θ value of ~14^{o} observed from perovskite films suggests the presence of a pure α-perovskite phase (Shin et al., 2015). The intensity of the peak increases with increasing annealing temperature between 80 and 130^{o}C (**Figure** 4.11(b)). The diffraction patterns obtained for the films annealed at temperatures above 130^{o}C show a reduction of the α-phase of

perovskite. This suggests that the α-phase has been converted to cubic PbI_2 (**Figure** 4.11(b)). The cubic PbI_2 phase is more pronounced at 170^{o}C, indicating that at higher temperatures, most of the perovskite film decomposes to PbI_2.

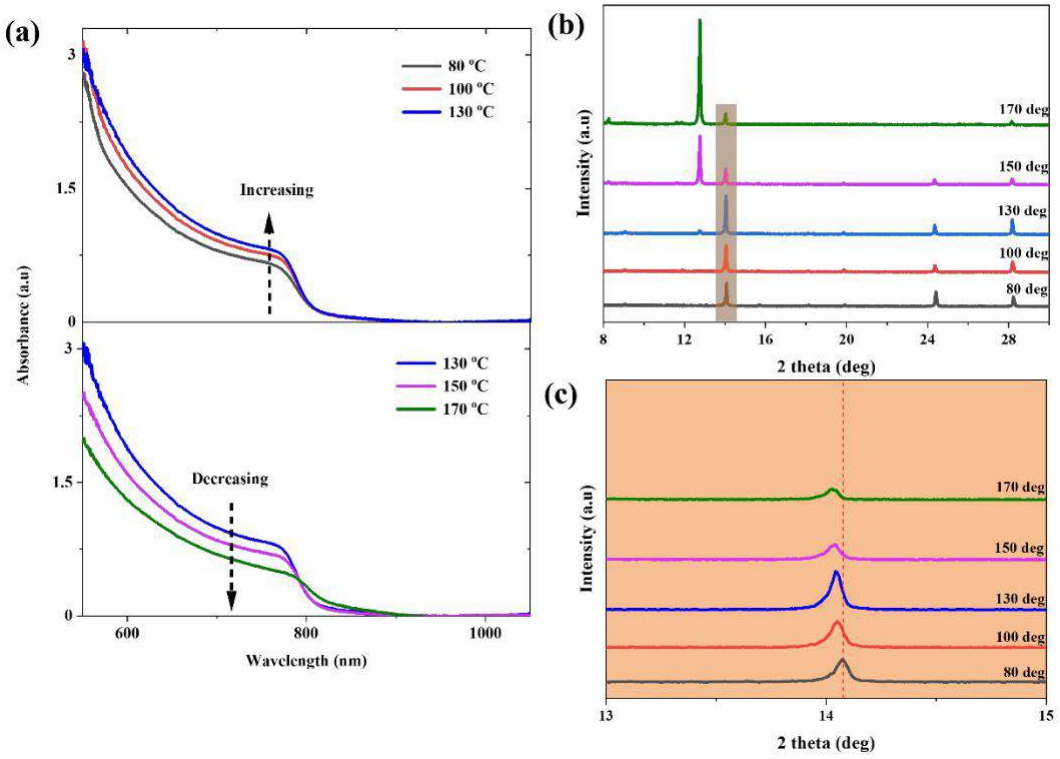

Figure 4.11. *(a) Absorption spectral of films, showing an increase in the absorbance with increasing annealing temperatures from 80^{o}C to 13 ^{o}C (top) and a decrease between 130^{o}C and 170^{o}C (bottom). (b) XRD patterns of films annealed at different temperatures. (c) Magnified XRD patterns of the α-phase of the perovskite films annealed at different temperatures.*

Annealing of the double cation (FA and MA) mixed halide organic components and PbI_2 produces a dark brown cubic perovskite phase (Oyewole et al., 2021), as the annealing temperature rises from 80 to 130^{o}C. At higher temperatures between 150 and 170^{o}C, a hexagonal perovskite phase is formed (Oyewole et al., 2021) which is evident in the PbI_2 peak at 130^{o}C with intensity being higher for the films annealed at 150 and 170^{o}C. Furthermore, a shift to lower diffraction angles

was also observed in the perovskite films (**Figure** 4.11(c)). This shift indicates tensile strain in the perovskite films (Zhu et al., n.d.), due to lattice expansion, that can cause compressive strains at the grain boundaries. The 2θ values of 14^{o}, 24.4^{o} and 28.2^{o} correspond, respectively to (110), (111) and (220) lattice planes for the perovskite tetragonal phase (F. Ma et al., 2016; Tong et al., 2015; Zhao & Zhu, 2013).

4.4.5. Electrical properties of PSCs

To further understand the effects of annealing temperature on the mechanical properties of PSCs, we characterize the current-voltage characteristics of the devices fabricated at different annealing temperatures **Figure** 4.12(a) shows the current density-voltage curves of PSCs prepared at annealing temperatures range between 80 to 170^{o}C. The architecture of the device is presented in **Figure** 4.12(inset). For the films annealed between 80 - 130^{o}C, we observed an increase in the hardness (H), open-circuit voltage (V_{oc}), short circuit current density (J_{sc}), and power conversion efficiency (PCE) (**Figures** 4.12(b) - 4.12(e)). From 80 to 130^{o}C, the devices exhibit improved performance characteristics with increasing hardness of the perovskite film. However, the hardness values of the perovskite films and the device parameters decreased with further increase in the annealing temperature (**Figures** 4.12(b) - 4.12(e)). The device parameters are summarized in **Table** 4.6.

It is important to note that the mechanical properties of films and device performance characteristic parameters show a clear relation with the increasing annealing temperature. The increased annealing temperature results in improved PCEs due to increased grain size and inter-diffusion of materials between layers in the PSCs (Oyewole et al., 2021) while the increased hardness is due to thermal-induced decrease in material length scales (**Table** 4.3) and yield strength (**Table** 4.5).

As the annealing temperature increases from 80 – 130^{o}C, the crystallinity of the sample increases, and we observed an increase in the hardness (H), open-circuit voltage (V_{oc}), short circuit current density (J_{sc}), and power conversion efficiency (PCE) (**Figures** 4.12(b) - 4.12(e)). From 80 to 130^{o}C, the devices exhibit improved performance characteristics. However, the device parameters decreased with further increase in the annealing temperature between 150 to 170^{o}C with reduction in the hardness (H), open-circuit voltage (V_{oc}), short circuit current density (J_{sc}), and power conversion efficiency (PCE). The J-V curves also show the presence of some resistances in the devices due to voids and cracks. At the higher temperatures (150 and 170 ^{o}C), the defects caused by voids and cracks decreased the PCE values, and increased length scale values lowered the hardness of the films. The best performing devices are those annealed at 130°C and have a PCE of 17.98% and hardness value of 0.83 GPa.

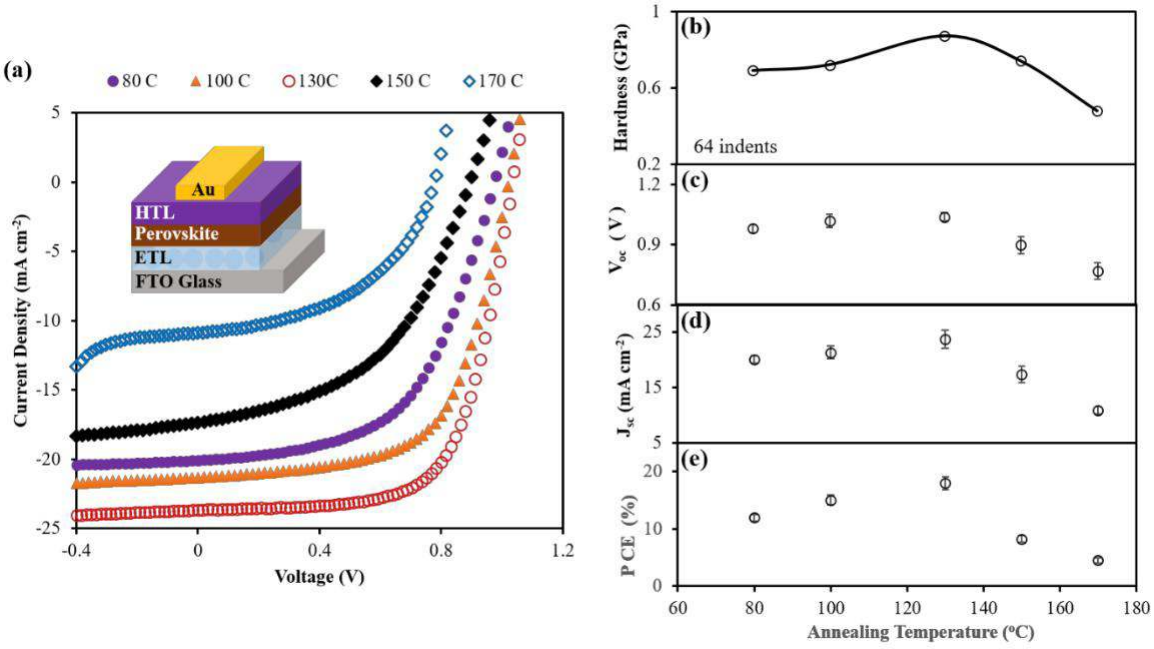

Figure 4.12. *Effects of annealing temperature on performance and mechanical properties. (a) J-V curves with the schematic of the device architecture (inset), (b) Hardness versus temperature,*

(c) Open circuit voltage, (d) Current density and (e) PCE of the PSCs at different annealing temperatures.

Table 4.6. *Summary of device parameters at different annealing temperatures*

Device Parameter	**Annealing Temperature (^{o}C)**				
	80	**100**	**130**	**150**	**170**
V_{oc} (V)	0.980 (0.89±0.021)	1.019 (0.991±0.032)	1.039 (1.002±0.022)	0.899 (0.786±0.043	0.768 (0.678±0.042)
J_{sc} (mA cm^2)	20.08 (19.32±1.34)	21.31 (19.56±2.31)	23.67 (21.54±3.23)	17.35 (15.89±3.02)	10.88 (8.81±1.27)
FF	0.549 (0.510±0.012)	0.625 (0.594±0.021)	0.658 (0.641±0.023)	0.478 (0.421±0.013)	0.484 (0.436±0.041)
PCE (%)	11.99 (10.43±1.20)	15.07 (14.23±1.74)	17.98 (16.02±2.32)	8.28 (7.04±1.24)	4.50 (3.89±0.89)

4.5. Summary and Concluding Remarks

We have shown that the temperature at which perovskite film is annealed affects the mechanical properties of the devices fabricated. The size dependence of hardness is due to the increase in the density of GNDs with decreasing indentation size. The indentation size effects are characterized between the micron- and nanoscales by a bi-linear SGP framework with source-limited and established dislocation substructures. The measured microstructural length scales decrease with increasing annealing temperature to 130^{o}C, after which it began to increase, causing films annealed beyond 130^{o}C to have reduced strengths because the larger microstructural length scales correspond to larger dislocation spacings and weaker dislocation interactions. Perovskite solar devices annealed at temperatures above 130^{o}C have poor performance. We have shown that

perovskite solar cell devices annealed at 130^{o}C exhibit optimal performance and attractive combinations of mechanical properties.

4.6 References

Ashby, M. F. (1970). The deformation of plastically non-homogeneous materials. *Philosophical Magazine*, *21*(170), 399–424. https://doi.org/10.1080/14786437008238426

Bade, S. G. R., Li, J., Shan, X., Ling, Y., Tian, Y., Dilbeck, T., Besara, T., Geske, T., Gao, H., Ma, B., Hanson, K., Siegrist, T., Xu, C., & Yu, Z. (2015). Fully Printed Halide Perovskite Light-Emitting Diodes with Silver Nanowire Electrodes. *ACS Nano*, *10*(2), 1795–1801. https://doi.org/10.1021/ACSNANO.5B07506

Best Research-Cell Efficiency Chart | Enhanced Reader. (n.d.). Retrieved October 1, 2021, from moz-extension://59238ff8-d379-460e-a75f-f63264ca7971/enhanced-reader.html?openApp&pdf=https%3A%2F%2Fwww.nrel.gov%2Fpv%2Fassets%2Fpdfs%2Fbest-research-cell-efficiencies.20190802.pdf

Callister, W. D., & Rethwisch, D. G. (n.d.). *Materials science and engineering: an introduction*.

Cao,Y., Allameh, S., Nankivil, D., Sethiaraj, S., Otiti, T., & Soboyejo, W. (2006). *Nanoindentation measurements of the mechanical properties of polycrystalline Au and Ag thin films on silicon substrates: Effects of grain size and film thickness*. https://doi.org/10.1016/j.msea.2006.04.080

Chen, J.-Q., Huang, Q.-S., Qi, R.-Z., Feng, Y.-F., Feng, J.-T., Zhang, Z., Li, W.-B., & Wang, Z.-S. (2019). Effects of sputtering power and annealing temperature on surface roughness of

gold films for high-reflectivity synchrotron radiation mirrors. *Nuclear Science and Techniques 2019 30:7*, *30*(7), 1–6. https://doi.org/10.1007/S41365-019-0635-X

Chen, L.-C., Wu, J.-R., Tseng, Z.-L., Chen, C.-C., Chang, S. H., Huang, J.-K., Lee, K.-L., & Cheng, H.-M. (n.d.). *materials Annealing Effect on (FAPbI 3) 1−x (MAPbBr 3) x Perovskite Films in Inverted-Type Perovskite Solar Cells*. https://doi.org/10.3390/ma9090747

Doerner, M. F., & Nix, W. D. (1986). A method for interpreting the data from depth-sensing indentation instruments. *Journal of Materials Research*, *1*(4), 601–609. https://doi.org/10.1557/JMR.1986.0601

Dualeh, A., Tétreault, N., Moehl, T., Gao, P., Nazeeruddin, M. K., & Grätzel, M. (2014). Effect of Annealing Temperature on Film Morphology of Organic–Inorganic Hybrid Pervoskite Solid-State Solar Cells. *Advanced Functional Materials*, *24*(21), 3250–3258. https://doi.org/10.1002/ADFM.201304022

Elmustafa, A. A., Lou, J., Adewoye, O., Soboyejo, W. O., & Stone, D. S. (2002). Bilinear behavior in the indentation size effect: A consequence of strain gradient plasticity. *Materials Research Society Symposium - Proceedings*, *750*, 27–32. https://doi.org/10.1557/PROC-750-Y1.7

Faghihnasiri, M., Izadifard, M., & Ghazi, M. E. (2017). DFT Study of Mechanical Properties and Stability of Cubic Methylammonium Lead Halide Perovskites (CH3NH3PbX3, X = I, Br, Cl). *Journal of Physical Chemistry C*, *121*(48), 27059–27070. https://doi.org/10.1021/acs.jpcc.7b07129

Feng, J. (2014). Mechanical properties of hybrid organic-inorganic CH3NH 3BX3 (B = Sn, Pb; X = Br, I) perovskites for solar cell absorbers. *APL Materials*, *2*(8). https://doi.org/10.1063/1.4885256

Fleck, N. A., Muller, G. M., Ashby, M. F., & Hutchinson, J. W. (1994). Strain gradient plasticity: Theory and experiment. *Acta Metallurgica Et Materialia*, *42*(2), 475–487. https://doi.org/10.1016/0956-7151(94)90502-9

Fu, Y., Zhu, H., Schrader, A. W., Liang, D., Ding, Q., Joshi, P., Hwang, L., Zhu, X.-Y., & Jin, S. (2016). Nanowire Lasers of Formamidinium Lead Halide Perovskites and Their Stabilized Alloys with Improved Stability. *Nano Letters*, *16*(2), 1000–1008. https://doi.org/10.1021/ACS.NANOLETT.5B04053

Gao, H., Huang, Y., Nix, W. D., & Hutchinson, J. W. (1999). Mechanism-based strain gradient plasticity - I. Theory. *Journal of the Mechanics and Physics of Solids*, *47*(6), 1239–1263. https://doi.org/10.1016/S0022-5096(98)00103-3

Grätzel, M. (2014). The light and shade of perovskite solar cells. *Nature Materials*, *13*(9), 838–842. https://doi.org/10.1038/NMAT4065

Green, M. A., Ho-Baillie, A., & Snaith, H. J. (2014). The emergence of perovskite solar cells. *Nature Photonics 2014 8:7*, *8*(7), 506–514. https://doi.org/10.1038/nphoton.2014.134

Greer, J. R., & Nix, W. D. (2005). Size dependence of mechanical properties of gold at the sub-micron scale. *Applied Physics A: Materials Science and Processing*, *80*(8), 1625–1629. https://doi.org/10.1007/S00339-005-3204-6

Hay, J., & Crawford, B. (2011). Measuring substrate-independent modulus of thin films. *Journal of Materials Research*, *26*(6), 727–738. https://doi.org/10.1557/JMR.2011.8

Koech, R. K., Ichwani, R., Martin, J. L., Oyewole, D. O., Oyelade, O. V., Olanrewaju, Y. A., Sanni, D. M., Adeniji, S. A., Grimm, R. L., Bello, A., Oyewole, O. K., Ntsoenzok, E., &

Soboyejo, W. O. (2021). A study of the effects of a thermally evaporated nanoscale CsBr layer on the optoelectronic properties and stability of formamidinium-rich perovskite solar cells. *AIP Advances*, *11*(9), 095112. https://doi.org/10.1063/5.0064398

Kianoosh Poorkazem, Dianyi Liu, & L. Kelly, T. (2015). Fatigue resistance of a flexible, efficient, and metal oxide-free perovskite solar cell. *Journal of Materials Chemistry A*, *3*(17), 9241– 9248. https://doi.org/10.1039/C5TA00084J

Kim, M., Kim, G. H., Oh, K. S., Jo, Y., Yoon, H., Kim, K. H., Lee, H., Kim, J. Y., & Kim, D. S. (2017). High-Temperature-Short-Time Annealing Process for High-Performance Large-Area Perovskite Solar Cells. *ACS Nano*, *11*(6), 6057–6064. https://doi.org/10.1021/ACSNANO.7B02015/SUPPL_FILE/NN7B02015_SI_001.PDF

Lee, G., Kim, M. C., Choi, Y. W., Ahn, N., Jang, J., Yoon, J., Kim, S. M., Lee, J. G., Kang, D., Jung, H. S., & Choi, M. (2019). Ultra-flexible perovskite solar cells with crumpling durability: toward a wearable power source. *Energy & Environmental Science*, *12*(10), 3182– 3191. https://doi.org/10.1039/C9EE01944H

Lei Guo, Gang Tang, Jiawang Hong. (2019). Mechanical Properties of Formamidinium Halide Perovskites FABX${3}$ (FA=CH(NH$_{2})_{2}$; B=Pb, Sn; X=Br, I) by First-Principles Calculations. *Chinese Physics Letters*, *36*(5), 056201. https://doi.org/10.1088/0256-307X/36/5/056201

Li, D., Jen, A. K., Zhang, H., Cheng, J., Li, D., Lin, F., Mao, J., Liang, C., Jen, A. K., Grätzel, M., & Choy, W. C. H. (2017). *Toward All Room-Temperature, Solution- Processed , High-Performance Planar Perovskite Solar Cells : A ... Toward All Room-Temperature , Solution-Processed , High-Performance Planar Perovskite Solar Cells : A New Scheme of Pyridine-*

Promoted Perovskite For. *January*. https://doi.org/10.1002/adma.201604695

Lou, J., Shrotriya, P., Buchheit, T., Yang, D., & Soboyejo, W. O. (2003). Nanoindentation study of plasticity length scale effects in LIGA Ni microelectromechanical systems structures. *Journal of Materials Research*, *18*(3), 719–728. https://doi.org/10.1557/JMR.2003.0097

Ma, F., Li, J., Li, W., Lin, N., Wang, L., & Qiao, J. (2016). Stable α/δ phase junction of formamidinium lead iodide perovskites for enhanced near-infrared emission. *Chemical Science*, *8*(1), 800–805. https://doi.org/10.1039/C6SC03542F

Ma, L., Li, W., Yang, K., Bi, J., Feng, J., Zhang, J., Yan, Z., Zhou, X., Liu, C., Ji, Y., Huang, J. C., & Han, X. (2021). A- or X-site mixture on mechanical properties of APbX3 perovskite single crystals. *APL Materials*, *9*(4), 041112. https://doi.org/10.1063/5.0015569

Ma, Q., & Clarke, D. R. (2011). Size dependent hardness of silver single crystals. *Journal of Materials Research 1995 10:4*, *10*(4), 853–863. https://doi.org/10.1557/JMR.1995.0853

Mettan, X., Pisoni, R., Matus, P., Pisoni, A., Jaćimović, J., Náfrádi, B., Spina, M., Pavuna, D., Forró, L., & Horváth, E. (n.d.). *Tuning of the Thermoelectric Figure of Merit of CH 3 NH 3 MI 3 (M=Pb,Sn) Photovoltaic Perovskites*.

Mosconi, E., Umari, P., & Angelis, F. De. (2015). Electronic and optical properties of mixed Sn–Pb organohalide perovskites: a first principles investigation. *Journal of Materials Chemistry A*, *3*(17), 9208–9215. https://doi.org/10.1039/C4TA06230B

Nix, W. D., & Gao, H. (1998). Indentation size effects in crystalline materials: A law for strain gradient plasticity. *JMPSo*, *46*(3), 411–425. https://doi.org/10.1016/S0022-5096(97)00086-0

Oliver, W. C., & Pharr, G. M. (1992). An improved technique for determining hardness and elastic

modulus using load and displacement sensing indentation experiments. *Journal of Materials Research*, *7*(6), 1564–1583. https://doi.org/10.1557/jmr.1992.1564

Olanrewaju, Y. A., Orisekeh, K., Oyelade, O. V., Koech, R. K., Ichwani, R., Ebunu, A. I., Amune, D. I., Bello, A., Anye, V. C., Oyewole, O. K., & Soboyejo, W. O. (2022). Effects of temperature-dependent burn-in decay on the performance of triple cation mixed halide perovskite solar cells. *AIP Advances*, *12*(1), 015122. https://doi.org/10.1063/5.0078821

Oyelade, O. V, Oyewole, O. K., Adeniji, S. A., Ichwani, R., Sanni, D. M., & Soboyejo, W. O. (n.d.). *pressure-Assisted fabrication of perovskite Solar cells*. https://doi.org/10.1038/s41598-020-64090-5

Oyewole, D. O., Koech, R. K., Ichwani, R., Ahmed, R., Tamayo, J. H., Adeniji, S. A., Cromwell, J., Ulloa, E. C., Oyewole, O. K., Agyei-Tuffour, B., Titova, L. V., Burnham, N. A., & Soboyejo, W. O. (2021). Annealing effects on interdiffusion in layered FA-rich perovskite solar cells. *AIP Advances*, *11*(6), 065327. https://doi.org/10.1063/5.0046205

Park, M., Kim, H. J., Jeong, I., Lee, J., Lee, H., Son, H. J., Kim, D.-E., & Ko, M. J. (2015). Mechanically Recoverable and Highly Efficient Perovskite Solar Cells: Investigation of Intrinsic Flexibility of Organic–Inorganic Perovskite. *Advanced Energy Materials*, *5*(22), 1501406. https://doi.org/10.1002/AENM.201501406

Peng, W., Anand, B., Liu, L., Sampat, S., Bearden, B. E., Malko, A. V., & Chabal, Y. J. (2016). Influence of growth temperature on bulk and surface defects in hybrid lead halide perovskite films. *Nanoscale*, *8*(3), 1627–1634. https://doi.org/10.1039/C5NR06222E

QUARRELL, A. G. (1952). The Hardness of Metals. *Nature 1952 170:4333*, *170*(4333), 818–818. https://doi.org/10.1038/170818b0

Rakita, Y., Cohen, S. R., Kedem, N. K., Hodes, G., & Cahen, D. (2015). Mechanical properties of APbX3 (A = Cs or CH3NH3; X= I or Br) perovskite single crystals. *MRS Communications 2015 5:4*, *5*(4), 623–629. https://doi.org/10.1557/MRC.2015.69

Reyes-Martinez, M. A., Abdelhady, A. L., Saidaminov, M. I., Chung, D. Y., Bakr, O. M., Kanatzidis, M. G., Soboyejo, W. O., & Loo, Y.-L. (2017). Time-Dependent Mechanical Response of APbX3 (A = Cs, CH3NH3; X = I, Br) Single Crystals. *Advanced Materials*, *29*(24), 1606556. https://doi.org/10.1002/ADMA.201606556

S, S., FH, I., Z, D., F, W., G, K., PD, B., J, O., & AK, C. (2017). Factors Influencing the Mechanical Properties of Formamidinium Lead Halides and Related Hybrid Perovskites. *ChemSusChem*, *10*(19), 3740–3745. https://doi.org/10.1002/CSSC.201700991

Saha, R., & Nix, W. D. (2002). Effects of the substrate on the determination of thin film mechanical properties by nanoindentation. *Acta Materialia*, *50*(1), 23–38. https://doi.org/10.1016/S1359-6454(01)00328-7

Schneider, M., Werner, F., Langenkämper, D., Reinhart, C., & Laplanche, G. (2019). Effect of Temperature and Texture on Hall–Petch Strengthening by Grain and Annealing Twin Boundaries in the MnFeNi Medium-Entropy Alloy. *Metals 2019, Vol. 9, Page 84*, *9*(1), 84. https://doi.org/10.3390/MET9010084

Sha, Z. D., Quek, S. S., Pei, Q. X., Liu, Z. S., Wang, T. J., Shenoy, V. B., & Zhang, Y. W. (2014). Inverse pseudo Hall-Petch relation in polycrystalline graphene. *Scientific Reports*, *4*. https://doi.org/10.1038/SREP05991

Shin, S. S., Yang, W. S., Noh, J. H., Suk, J. H., Jeon, N. J., Park, J. H., Kim, J. S., Seong, W. M., & Seok, S. Il. (2015). High-performance flexible perovskite solar cells exploiting Zn2SnO4

prepared in solution below 100 °C. *Nature Communications*, *6*(May), 1–8. https://doi.org/10.1038/ncomms8410

Stranks, S. D., & Snaith, H. J. (2015). Metal-halide perovskites for photovoltaic and light-emitting devices. *Nature Nanotechnology 2015 10:5*, *10*(5), 391–402. https://doi.org/10.1038/nnano.2015.90

Su, T., Li, X., Zhang, Y., Zhang, F., & Sheng, Z. (2017). Temperature-modulated crystal growth and performance for highly reproducible and efficient perovskite solar cells. *Physical Chemistry Chemical Physics*, *19*(20), 13147–13152. https://doi.org/10.1039/C7CP00563F

Tong, X., Zhang, H., & Li, D. Y. (2015). Effect of Annealing Treatment on Mechanical Properties of Nanocrystalline α-iron: an Atomistic Study. *Scientific Reports 2015 5:1*, *5*(1), 1–7. https://doi.org/10.1038/srep08459

Wehrenfennig, C., Liu, M., Snaith, H. J., Johnston, M. B., & Herz, L. M. (2014). Charge carrier recombination channels in the low-temperature phase of organic-inorganic lead halide perovskite thin films. *APL Materials*, *2*(8). https://doi.org/10.1063/1.4891595

X, C., L, Z., Y, J., Y, L., X, C., K, Z., L, C., K, D., & J, W. (2018). High annealing temperature induced rapid grain coarsening for efficient perovskite solar cells. *Journal of Colloid and Interface Science*, *524*, 483–489. https://doi.org/10.1016/J.JCIS.2018.04.019

Yu, J., Wang, M., & Lin, S. (2016). *Probing the Soft and Nano-Ductile Mechanical Nature of Single and Polycrystalline Organic-Inorganic Hybrid Perovskites for Flexible Functional Devices Probing the Soft and Nano-Ductile Mechanical Nature of Single and Polycrystalline Organic-Inorganic Hybr*. https://doi.org/10.1021/acsnano.6b05913

Zhao, Y., & Zhu, K. (2013). Charge transport and recombination in perovskite (CH3NH 3) PbI3 sensitized TiO2 Solar Cells. *Journal of Physical Chemistry Letters*, *4*(17), 2880–2884. https://doi.org/10.1021/JZ401527Q/SUPPL_FILE/JZ401527Q_SI_001.PDF

Zhu, C., Niu, X., Fu, Y., Li, N., Hu, C., Chen, Y., He, X., Na, G., Liu, P., Zai, H., Ge, Y., Lu, Y., Ke, X., Bai, Y., Yang, S., Chen, P., Li, Y., Sui, M., Zhang, L., … Chen, Q. (n.d.). *Strain engineering in perovskite solar cells and its impacts on carrier dynamics*. https://doi.org/10.1038/s41467-019-08507-4

Zong, Z., Lou, J., Adewoye, O. O., Elmustafa, A. A., Hammad, F., & Soboyejo, W. O. (2006). Indentation size effects in the nano- and micro-hardness of fcc single crystal metals. *Materials Science and Engineering A*, *434*(1–2), 178–187. https://doi.org/10.1016/j.msea.2006.06.137

Zong, Zong, & Soboyejo, W. (2005). Indentation size effects in face centered cubic single crystal thin films. *Materials Science and Engineering A*, *404*, 281–290. https://doi.org/10.1016/j.msea.2005.05.075

Chapter 5

EFFECTS OF PEO ON FAILURE MECHANISMS OF FLEXIBLE PEROVSKITE SOLAR CELLS UNDER MONOTONIC AND CYCLIC BENDING

5.1 Introduction

Organic-inorganic hybrid perovskites (OIHPs)'s compatibility with low-temperature solution process are promising candidates for photoactive materials for lightweight and flexible photovoltaic devices to meet the increasing needs for portable power sources, such as robotic systems, wearable electronics, consumer electronics, remote power, and automobiles (Chirilă et al., 2013; Kaltenbrunner et al., 2015; Yaowen Li et al., 2016; Nie et al., 2015; Qiu et al., 2014; Ren & Jung, 2018; Yang, Yang, et al., 2016). Due to their outstanding properties, such as defect tolerance (Yang et al., 2018), tunable bandgap (Prasanna et al., 2017; Zhu et al., 2017), high charge carrier mobility (Wehrenfennig, Eperon, et al., 2014; Wehrenfennig, Liu, et al., 2014; Yang et al., 2015), long electron-hole diffusion length (Dong et al., 2015; G et al., 2013; Yang, Zhou, et al., 2016), extremely low trap density, (Lin et al., 2014; Y. Liu et al., 2015; Y. Liu, Zhang, et al., 2016), small exciton–binding energy, large absorption coefficient, and so on, OIHPs have made remarkable achievements (Y. Liu, Sun, et al., 2016; Yu, 2016). Because of recent advancements in interface modification (Chueh et al., 2015; Zhou et al., 2014), morphology manipulation (Jeon et al., 2014; Zuo et al., 2016), and composition engineering (McMeekin et al., 2016; Saliba, Matsui, Seo, et al., 2016), the state-of-the-art OIHPs power conversion efficiency (PCE) has risen from 3.8

% in 2009 to a certified state-of-the-art value of more than 25 % in a short period (Kojima et al., 2009).

Recently flexible perovskite solar cells (FPSCs) have received attention due to their tremendous potential in portable and wearable electronics (Yang Li et al., 2021; Ma et al., 2020). Perovskite solar cells are suitable for flexible applications because of their low-cost materials, high efficiency, and potential for a solution-based roll-to-roll method.

Mechanical stability is a consideration for the development of flexible PSCs. Until now, the mechanical robustness of flexible PSCs has prevented them from being used in portable and wearable devices (Gong et al., 2021; Kaltenbrunner et al., 2015; Kang et al., 2019; Lee et al., 2019). The requirement of low-temperature processing for plastic-based flexible PSCs creates issues in achieving high efficiency and mechanical robustness. In flexible PSCs, the inverted p-i-n architecture is utilized to avoid the usage of metal oxide, which demands a high annealing temperature during fabrication. Flexible PSCs, however, have a lower PCE than rigid PSCs (Huang et al., 2019). Furthermore, monitoring the bending fatigue of flexible perovskite solar cells is critical for the real-world application and commercialization of flexible solar cells.

Additive engineering is used to passivate defects in perovskite to reduce the nonrelative recombination loss and enhance the PCE of the PSCs (Han et al., 2019; Sun et al., 2018). For the perovskite fabrication, various additives such as urea and polymer were developed and incorporated into the precursor solution. Rubidium cation (Rb) can be used to create a perovskite structure with outstanding photoelectric characteristics by incorporating it into a "cation cascade" (Saliba, Matsui, Domanski, et al., 2016). Sodium fluoride and a cross-linkable organic small molecule additive trimethylolpropane triacrylate (TMTA) have been introduced into a perovskite absorber to improve PSC efficiency and stability by strengthening chemical bonding (N. Li et al.,

2019; X. Li et al., 2018). The mentioned strategies aim at improving the film morphology and decreasing defects of the perovskite in flexible PSCs to improve their performance.

In this study, the mechanical robustness of inverted flexible PSCs is increased by introducing small amount of novel additive polymer, polyoxyethylene (PEO) to the double-cation perovskite precursor, to promote the grain size and passivate the defects of the film. PEO has several advantages as a material for interfacial engineering, including low cost, environmental friendliness, high transmittance, high polarity, and ease of mixing with perovskite precursors.

Flexing makes the devices undergo mechanical deformation, inducing the decrease of efficiency, which has been widely reported (S. Adeniji et al., 2021; O. Oyewole et al., 2020; Jin et al., 2018; X. Liu et al., 2018). Since such materials and layered structures can deform and fail by several deformation mechanisms, there is a need to develop a fundamental understanding of the possible deformation and failure mechanisms that can occur in flexible perovskite solar cells.

Herein, we report an effective additive technique developed to control the perovskite morphology on flexible substrates for FPSCs. The PEO additive improved the quality of the perovskite film on the PET/ITO substrates. Specifically, both the grain size and crystallinity were significantly enhanced. We use a combined experimental and theoretical approach to study the failure and fatigue behavior of flexible perovskite solar cells. We began with computational models and simulations to gain insights into cracking and failure mechanisms in layered materials relevant to flexible perovskite solar cells. The simulations were validated with experiments, then a study of the effects of fatigue on the optical properties and photoconversion efficiencies of the layered flexible perovskite solar cells were carried out. We conducted load controlled monotonic and cyclic deformation tests on flexible perovskite solar cells to estimate the fatigue lifetimes at

different applied strains for rollers of different radii. The implication of the current work is then discussed to improve the design of flexible perovskite solar cells.

5.2 Bending Theory

When an external bending motion is applied to devices in a mono-layer system, physical deformation occurs everywhere in the structure. Then, to resist shape deformation, inner stress is created. Because stress can be localized due to the non-uniform position, the stress distribution is heterogeneous throughout the devices. Within the linear elastic range, the elastic modulus, according to Hooke's law, relates stress and strain by a simple ratio (Harris et al., 2016). When a film-on-substrate model is bent into a cylinder of radius R as a mechanical beam, the outer surface experiences tensile strain while the inner surface experiences compressive strain. Inside the device, there is a mechanical neutral plane with no uniaxial strain, and its position is proportional to Young's modulus and layer thickness (Gleskova et al., 1999). Ultra-flexibility is achieved by placing the stiff film on the mechanical neutral plane. Bending mechanics in multilayer structures becomes complicated due to differences in material properties (such as elastic modulus and Poisson's ratio) (Park et al., 2008). The mismatch between the stiff film and the flexible substrate causes stress to concentrate on the film or the interface between layers. When the obtained stress exceeds the tolerance limit, structures get destroyed (e.g., crack (S. R. Kim & Nairn, 2000; Park et al., 2008) or delamination (Dai et al., 2015), and their optical and electrical properties deteriorate.

Cracks develop at defect sites of component layers under tensile strain. The film buckles with a large unbonded area under compression strain, and normal and shear stresses can cause the buckle

area to grow like a crack. As a result, the bonding strength (adhesion) is proportional to the compression strain endurance. The strain in the convex surface is equal to the distance from the neutral plane divided by (Suo et al., 1999)

$$= \quad - \tag{5.1}$$

Thin film undergoes low bending strain at a given bending radius , as stated in Equation (5.1), and maintains its function at a low critical bending radius. The distance between the outer surface and the mechanical neutral plane can be calculated as follows:

$$= \quad \frac{}{2} + \frac{(1+2 + \ ^2)}{(1+)(1+)} \tag{5.2}$$

where the subscripts " " and " " denote the film and substrate, respectively; = / , where and denote the thickness of the film and substrate, respectively; = / , where and denote the Young's modulus of the film and substrate, respectively.

Therefore, the strain in convex surface can be described as:

$$= \quad \frac{}{2} + \frac{(1+2 + \ ^2)}{(1+)(1+)} \tag{5.3}$$

When the film and substrate have similar elastic moduli, that is ≈ , ≈ 1, the position of neutral plane coincides with the midplane of device, Equation (5.2) can be simplified as

$$= \quad \frac{}{2} + \tag{5.4}$$

and Equation (5.3) becomes

$$= \quad \frac{}{2} + \tag{5.5}$$

In a complicated multilayer structure, the component layers can be modeled as a composite beam subject to a bending curvature. The distance is given by (D. H. Kim et al., 2008; Park et al., 2009, 2010)

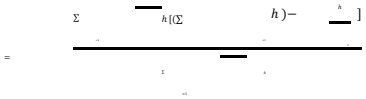

(5.6)

where is the total number of layers; h is the thickness of the h layer; when the devices are narrow is equal to the Young's modulus of each layer; when the biaxial deformation should be considered, is equal to the plane strain modulus = $(1 - ^2)$ where and denote the Young's modulus and the Poisson's ratio of the h layer, respectively.

5.3. Materials and Methods

5.3.1. Materials

ITO- PET(Sigma Aldrich, St Lous, MO, USA), PEO (Alfa Aesar, Ward Hill, MA, USA), PEDOT:PSS (H. C. Starck, Newton, MA, USA), Triton X-100 (Triton, MiliporeSigma, MO, USA) Lead iodide (PbI^2)(99.999%), di-isopropoxide bis(acetylacetone), Formamidinium iodide (FAI) (98%), methylammonium chloride (MACl), methylammonium bromide (MABr) (98%), dimethyformamide (DMF), dimethylsulfoxide (DMSO), PCBM, and anhhrous chlorobenzene were all purchased from Sigma Aldrich (Natick, MA, USA). All the materials were used there as received conditions.

5.3.2. Materials Processing

The flexible ITO-PET was cut into dimensions of 50 mm x 8 mm x 0.5 mm and mounted onto a rigid glass substrate for easy device fabrication and treated with UV-ozone cleaner (Novascan, Main Street Ames, IA, USA) for interface contacting. A mixture of PEDOT:PSS, DMSO and Triton X-100 was prepared with a volume ratio of 94:5:1. The dimethylsulfoxide was added to segregate the weak PSS for strong inter-PEDOT bridging. This increased the conductivity of PEDOT:PSS on the PET/ITO substrate. The Triton X-100 was added to increase the wettability of PEDOT:PSS on the PET/ITO. The mixture was stirred for 2 hours at room temperature before spin-coating onto the PET/ITO at 3000 rpm for 30 seconds and annealed at 100^{o}C for 10 minutes. PbI_2 solution was spin-coated onto the PEDOT:PSS layer at 1500 rpm for 30 seconds and annealed at 70^{o}C for 1 minute.

The formamidinium iodide-rich (FAI-rich) organic solution was prepared from 60 mg of FAI, 6 mg of MABr, and 6 mg of MACl in 1 ml of IPA. 10 mg of PEO was dissolved in 1 ml chlorobenzene and stirred at 30^{o}C for 30 minutes. The solution was incorporated into the perovskite precursor in volume of 0%, 5%, 10% and 30% weight ratio. The FAI-PEO mixture was spin coated on the PbI_2 at 1300 rpm for 30 seconds and annealed at 130^{o}C for 20 minutes. Some of the annealed perovskite films were set aside for characterization, while an electron transport layer (ETL) was spin coated on the films for PSC devices.

The ETL was prepared by dissolving 20 mg of PCBM in 1 ml chlorobenzene and stirred at room temperature for 1 hour. The mixture was spin coated on the perovskite films at 1000 rpm for 30 seconds. Finally, a 150 nm thick layer of silver was thermally evaporated onto the films using an Edward E306A thermal evaporator (Edward E306A, Easton PA, USA). The evaporation was

carried out at a vacuum pressure of ~1 x 10^{-6} Torr and a deposition rate of 0.2 nms^{-1}. A shadow mask of 1.2 cm^2 was used to define the area of the device.

Nanoindentation tests were carried out using KLA iMicro nanoindentation testing system (Nanomechanics, Inc., Oak Ridge, Tennessee), a universal nanomechanical in situ testing platform powered by the InForce 1000 electromagnetic actuator and capacitive displacement sensor. An Avantes UV-vis spectrophotometer (Avantes, BV, USA) was used to measure the optical absorbance. The microstructures of the top surfaces and cross sections of the films were observed under a field emission gun scanning electron microscope (SEM) (JSM 7000F, JOEL Ltd., Tokyo, Japan). The surface topographies of the films were examined using atomic force microscope (AFM) (-NX 20 Park Systems, Santa Clara, CA, USA). An X-ray diffractometer (Malvern PANalytical, Westborough, MA, USA) was used to obtain the XRD patterns of the perovskite film under a Cu K_α radiation source with Beta Nickle filter at 40 KV and 40 mA.

The current density-voltage curves were measured using a Keithley source meter unit 2400 system (Keithley, Tekronix, Newark, NJ, USA) connected to an Oriel solar simulator (Oriel, Newport Corporation, Irvine, CA, USA). The devices were exposed to AM 1.5G illumination of 100 $mWcm^{-2}$ during the current density-voltage measurements. The solar simulator was calibrated using a calibrated silicon cell (91150 V silicon reference cell, Newport).

5.3.3. Monotonic and Cyclic Bending Experiments

The samples of the flexible multilayered films (PET/ITO/PEDOT:PSS/ FAI-PEO) and devices (PET/ITO/PEDOT:PSS/FAI-PEO/PCBM/Ag) in the dimension 50mm x 8mm x 0.5mm were subjected to bending test on the Instron machine (Instron 8872, Instron, Norwood, MA, USA) that was instrumented with a very sensitive calibrated 10N load cell (10N Load cell, Instron Norwood,

MA, USA) using a fabricated fixture, by which the bending conditions, including bending directions, bending radius, and bending cycles were accurately controlled with high reproducibility of every bending result.

5.4. Results and Discussion

Improved crystalline quality and reduced defect concentration was observed with the addition of PEO. The PEO was added into the precursor in varying quantities from 0% to 30% to investigate its influence on the device performance.

The surface profile of the perovskite absorbers with the different amount of PEO in the precursor solution were investigated by scanning electron microscopy (SEM) (Figure 5.1). the average grain size is significantly enlarged from about 100 nm for the 0% PEO film to about 125 nm for the perovskite with 10% PEO (Figure 5.1(a-c)) The incorporation of the PEO results in a much uniform and compact perovskite morphology, which can be seen from the cross-section SEM images of PSCs with or without the PEO in Figure 5.1. With further increase in the PEO quantity to 30%, smaller grains with grain size of around 95 nm distributed between large grains was observed, which is responsible for decreased performance (Figure 5.1d). The root-mean-square decreased from 62.79 nm to 49.64 nm and to 45.43 nm respectively for precursors with 0, 5 and 10% PEO respectively as shown in the atomic force microscopy in Figure 5.2 (a-c). The 3D orientations of the AFM images are presented in Figure 5.3.

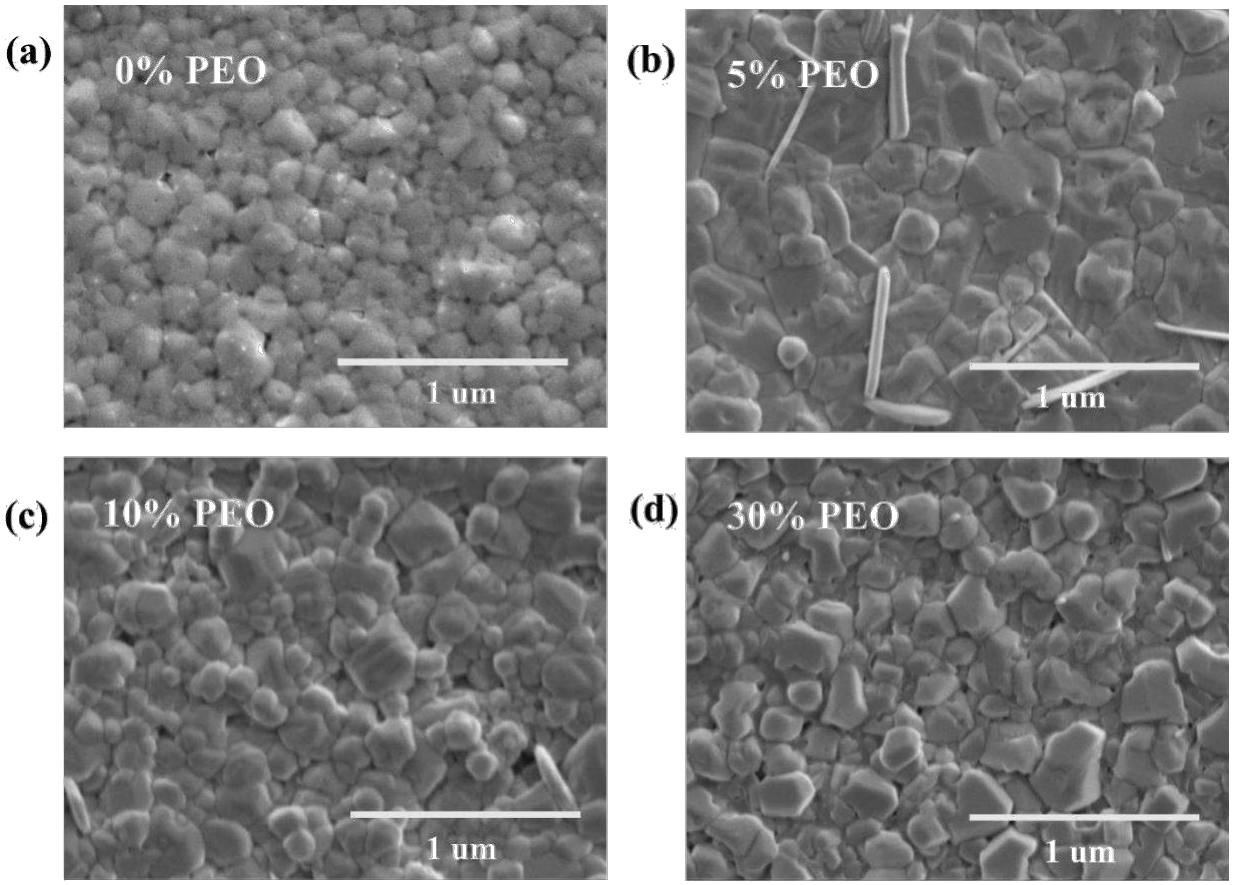

Figure 5.1. *SEM images for perovskite films with incorporation of (a) 0% PEO (b)5% PEO (c) 10% PEO (d) 30% PEO*

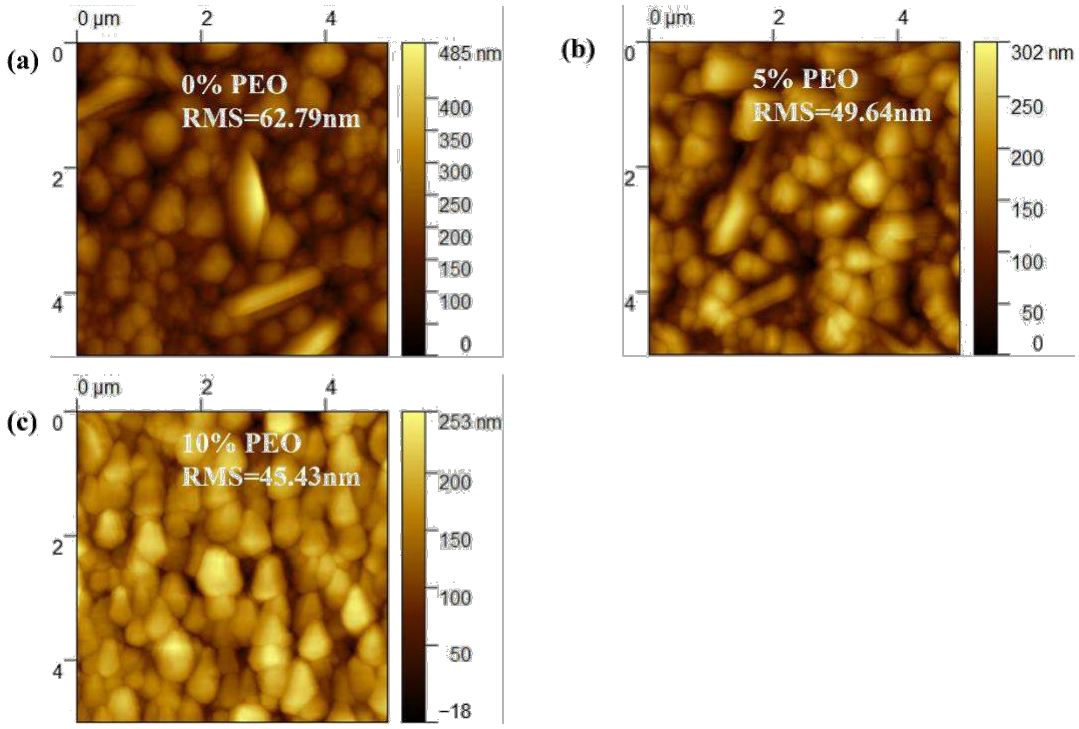

Figure 5.2. *AFM images for perovskite films of flexible PSCs (a) 0% PEO (b)5% PEO (c) 10% PEO*

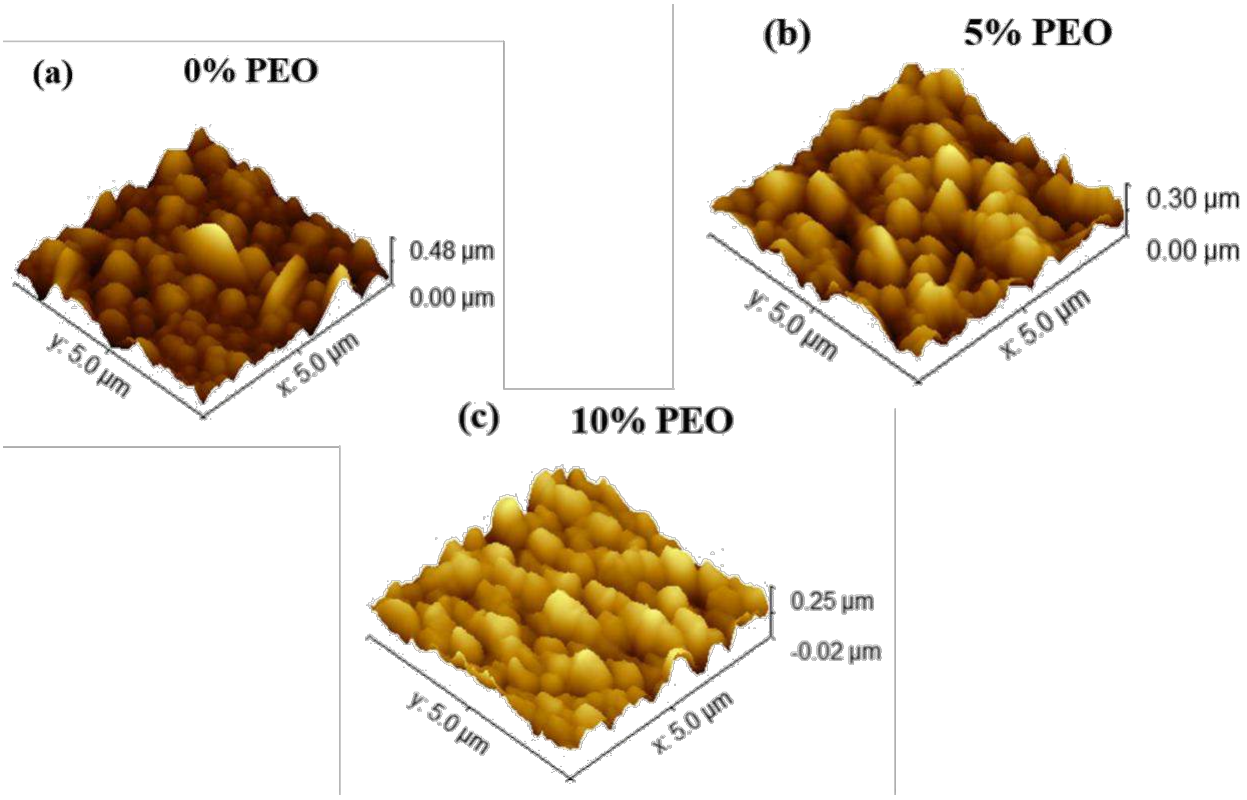

Figure 5.3. *The 3D orientation of the AFM images for perovskite films of flexible PSCs (a) 0% PEO (b)5% PEO (c) 10% PEO*

The bending stability of the device was investigated with three bending radii: 12.7 mm, 5.5 mm, and 3.5 mm for monotonic bend as shown in Figure 5.4 for 0, 5, 10 and 30% PEO content.

(a)

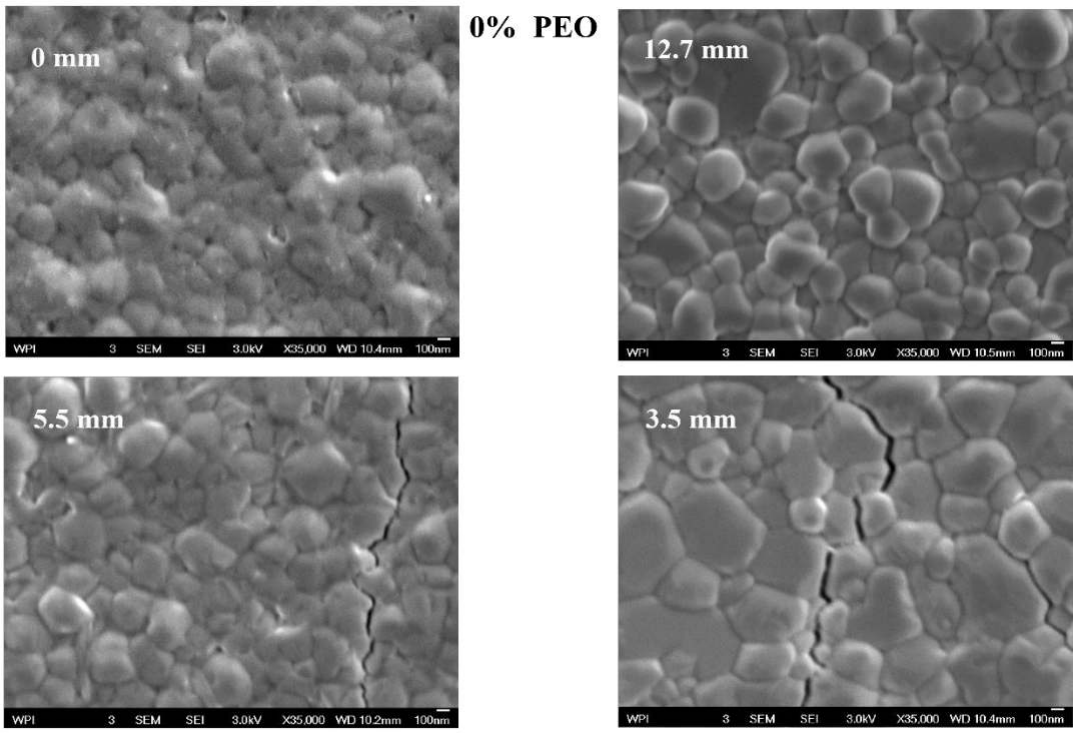

(b)

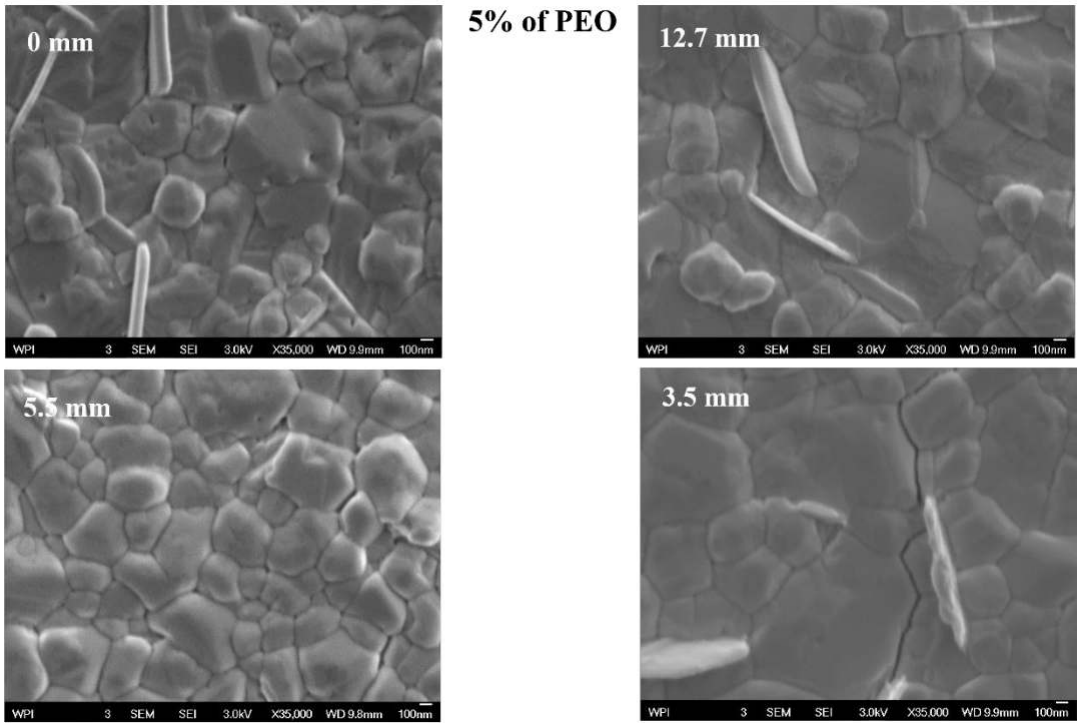

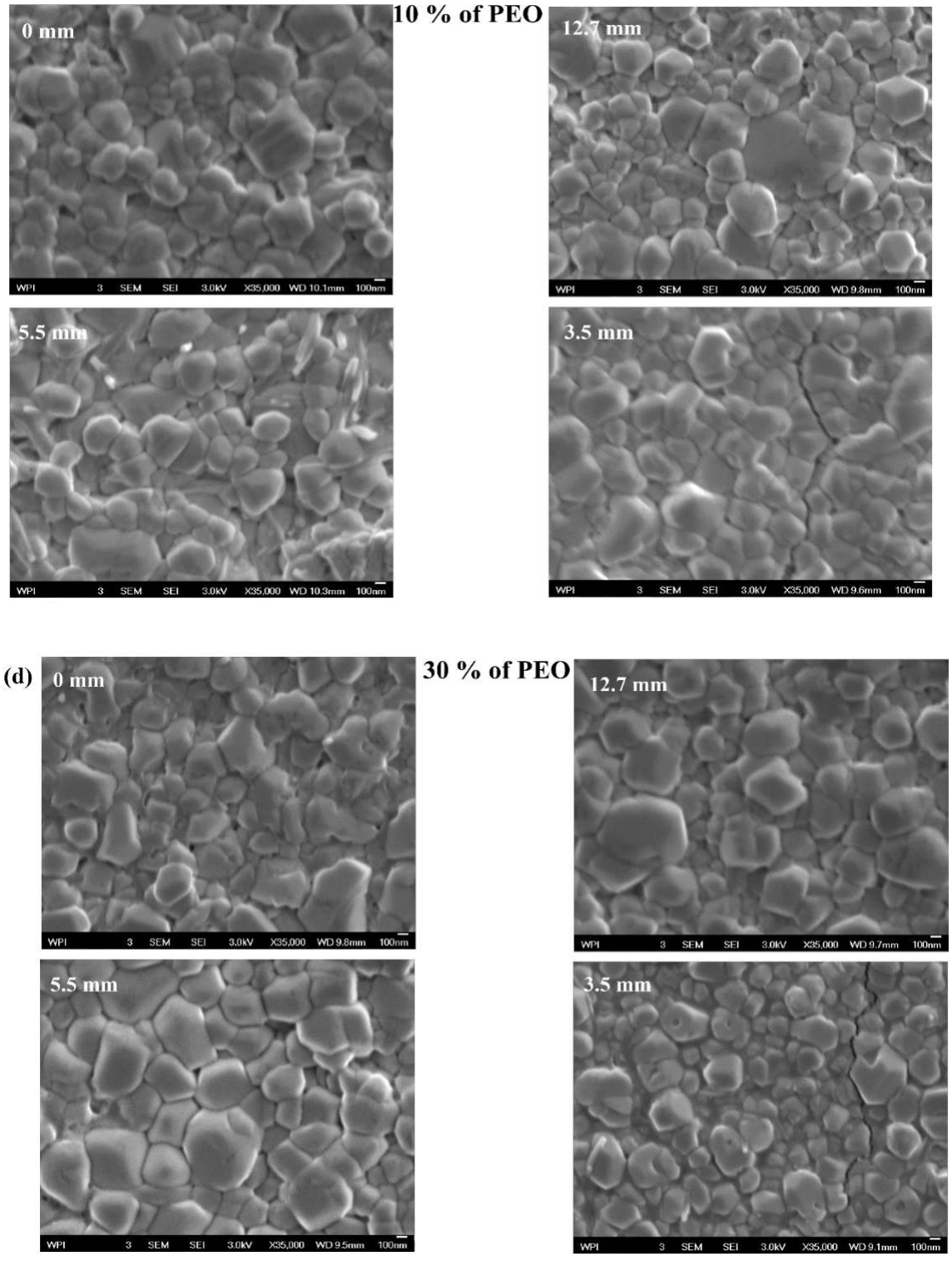

Figure 5.4. *Monotonic bend for all radii for perovskite films with (a) 0% PEO (b)5% PEO (c) 10% PEO (d) 30% PEO content*

The bending stability of the perovskite film for 0, 50 and 200 cycles for the various PEO contents are presented in Figure 5.5.

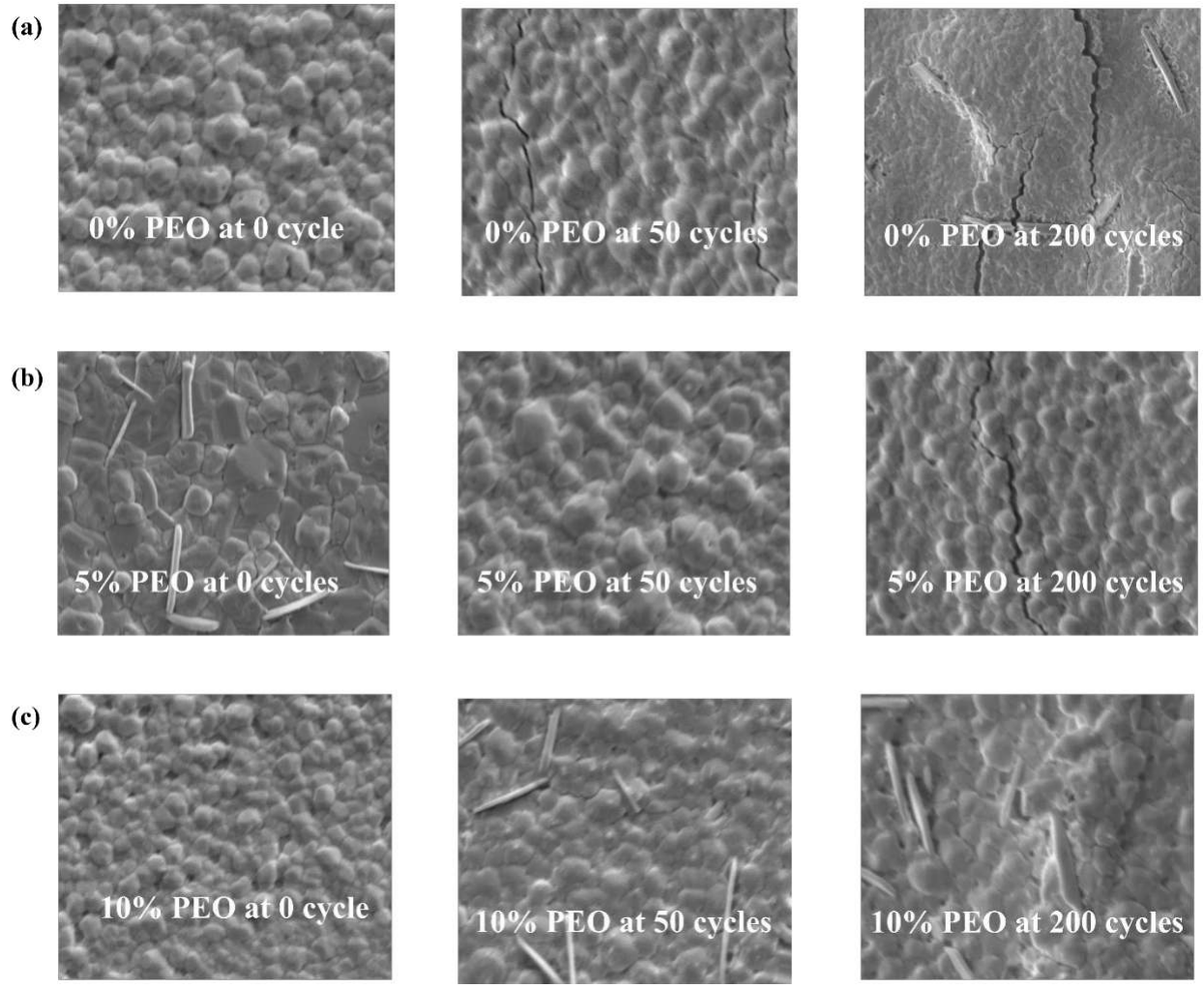

Figure 5.5. *Bending stability of the perovskite film for 0, 50 and 200 cycles for (a) 0% PEO (b)5% PEO (c) 10% PEO*

The improved crystallinity can be seen from the X-ray diffraction (XRD) patterns of the pristine film and PEO incorporated perovskite films (Figure 5.6). No significant shift in the diffraction peaks can be observed, indicating that PEO does not penetrate the pristine crystal lattice. The absorption spectra are presented in Figure 5.7 for the perovskite films incorporated with 0, 5, 10 and 30% PEO. The absorption increased with increasing content of PEO from 0 to 10% and reduced as the PEO content increased to 30%. The increase in absorbance, for films with PEO content, is associated with increased grain size.

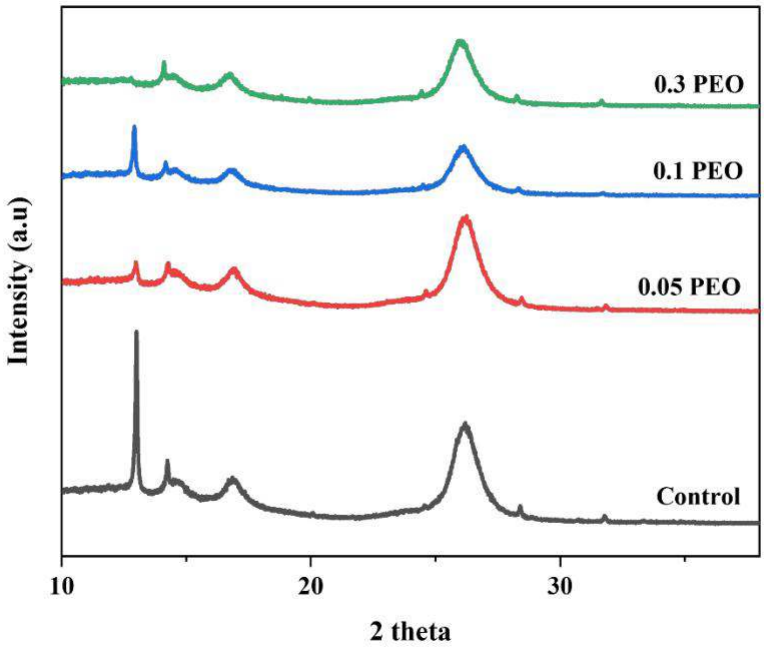

Figure 5.6. *XRD patterns of perovskite films of flexible PSCs*

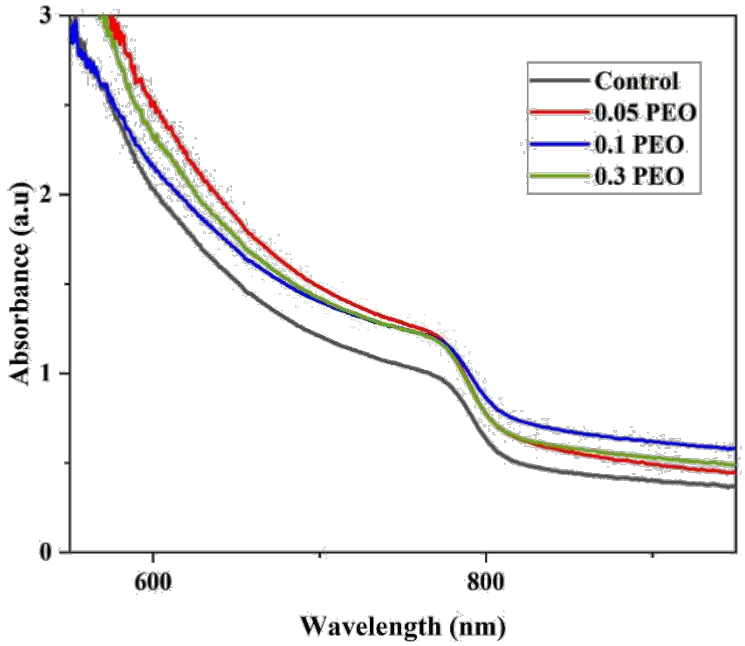

Figure 5.7. *Absorption spectra for perovskite films of flexible PSCs*

5.5. Summary and Concluding Remarks

A polymer additive, PEO was used to improve the crystallinity of FAI-rich perovskite to enhance the performances of the flexible PSCs. The morphology and crystallinity of the perovskite was improved by incorporating optimal content of PEO. The PSCs with 10% PEO exhibit remarkable mechanical robustness and PCE after many bending cycles at the least radius of 3.5 mm. This work provides a strategy to improve the PCE and mechanical robustness of flexible PSCs for the design of portable and wearable electronics.

5.6. References

Adeniji, S., Oyewole, O., Koech, R., Oyewole, D., Cromwell, J., Ahmed, R., Oyelade, O., Sanni, D., Orisekeh, K., Bello, A., Soboyejo, W., Adeniji, S., Oyewole, O., Koech, R., Oyewole, D., Cromwell, J., Ahmed, R., Soboyejo, W., Oyelade, O., … Bello, A. (2021). *Failure Mechanisms of Stretchable Perovskite Light-Emitting Devices under Monotonic and Cyclic Deformations*. https://doi.org/10.1002/mame.202100435

Chirilă, A., Reinhard, P., Pianezzi, F., Bloesch, P., Uhl, A. R., Fella, C., Kranz, L., Keller, D., Gretener, C., Hagendorfer, H., Jaeger, D., Erni, R., Nishiwaki, S., Buecheler, S., & Tiwari, A. N. (2013). Potassium-induced surface modification of Cu(In,Ga)Se2 thin films for high-efficiency solar cells. *Nature Materials*, *12*(12), 1107–1111. https://doi.org/10.1038/NMAT3789

Chueh, C. C., Li, C. Z., & Jen, A. K. Y. (2015). Recent progress and perspective in solution-processed Interfacial materials for efficient and stable polymer and organometal perovskite solar cells. *Energy & Environmental Science*, *8*(4), 1160–1189. https://doi.org/10.1039/C4EE03824J

Dai, L., Huang, Y., Chen, H., Feng, X., & Fang, D. (2015). Transition among failure modes of the bending system with a stiff film on a soft substrate. *Applied Physics Letters*, *106*(2), 021905. https://doi.org/10.1063/1.4905697

Dong, Q., Fang, Y., Shao, Y., Qiu, J., Cao, L., & Huang, J. (2015). *Electron-hole diffusion lengths > 175 μm in solution-grown CH 3 NH 3 PbI 3 single*. *January*, 1–8.

G, X., N, M., S, S., SS, L., YM, L., M, G., S, M., & TC, S. (2013). Long-range balanced electron-and hole-transport lengths in organic-inorganic CH3NH3PbI3. *Science (New York, N.Y.)*,

342(6156), 344–347. https://doi.org/10.1126/SCIENCE.1243167

Gleskova, H., Wagner, S., & Suo, Z. (1999). Failure resistance of amorphous silicon transistors under extreme in-plane strain. *Applied Physics Letters*, *75*(19), 3011. https://doi.org/10.1063/1.125174

Gong, C., Cheng, S., Meng, X., Hu, X., & Chen, Y. (2021). Recent Advances of PEDOT in Flexible Energy Conversion and Storage Devices. *Acta Chimica Sinica*, *79*(7), 853–868. https://doi.org/10.6023/A21030106

Han, T. H., Lee, J. W., Choi, C., Tan, S., Lee, C., Zhao, Y., Dai, Z., De Marco, N., Lee, S. J., Bae, S. H., Yuan, Y., Lee, H. M., Huang, Y., & Yang, Y. (2019). Perovskite-polymer composite cross-linker approach for highly stable and efficient perovskite solar cells. *Nature Communications*, *10*(1). https://doi.org/10.1038/S41467-019-08455-Z

Harris, K. D., Elias, A. L., & Chung, H. J. (2016). Flexible electronics under strain: a review of mechanical characterization and durability enhancement strategies. *Journal of Materials Science*, *51*(6), 2771–2805. https://doi.org/10.1007/s10853-015-9643-3

Huang, K., Peng, Y., Gao, Y., Shi, J., Li, H., Mo, X., Huang, H., Gao, Y., Ding, L., & Yang, J. (2019). High-Performance Flexible Perovskite Solar Cells via Precise Control of Electron Transport Layer. *Advanced Energy Materials*, *9*(44), 1901419. https://doi.org/10.1002/AENM.201901419

Jeon, N. J., Noh, J. H., Kim, Y. C., Yang, W. S., Ryu, S., & Seok, S. Il. (2014). Solvent engineering for high-performance inorganic–organic hybrid perovskite solar cells. *Nature Materials 2014 13:9*, *13*(9), 897–903. https://doi.org/10.1038/nmat4014

Jin, S. W., Lee, Y. H., Yeom, K. M., Yun, J., Park, H., Jeong, Y. R., Hong, S. Y., Lee, G., Oh, S. Y., Lee, J. H., Noh, J. H., & Ha, J. S. (2018). Highly Durable and Flexible Transparent Electrode for Flexible Optoelectronic Applications. *ACS Applied Materials and Interfaces*, *10*(36), 30706–30715. https://doi.org/10.1021/ACSAMI.8B10190

Kaltenbrunner, M., Adam, G., Głowacki, E. D., Drack, M., Schwödiauer, R., Leonat, L., Apaydin, D. H., Groiss, H., Scharber, M. C., White, M. S., Sariciftci, N. S., & Bauer, S. (2015). Flexible high power-per-weight perovskite solar cells with chromium oxide-metal contacts for improved stability in air. *Nature Materials*, *14*(10), 1032–1039. https://doi.org/10.1038/nmat4388

Kang, S. B., Kim, J. H., Jeong, M. H., Sanger, A., Kim, C. U., Kim, C. M., & Choi, K. J. (2019). Stretchable and colorless freestanding microwire arrays for transparent solar cells with flexibility. *Light: Science & Applications 2019 8:1*, *8*(1), 1–13. https://doi.org/10.1038/s41377-019-0234-y

Kim, D. H., Ahn, J. H., Won, M. C., Kim, H. S., Kim, T. H., Song, J., Huang, Y. Y., Liu, Z., Lu, C., & Rogers, J. A. (2008). Stretchable and foldable silicon integrated circuits. *Science (New York, N.Y.)*, *320*(5875), 507–511. https://doi.org/10.1126/SCIENCE.1154367

Kim, S. R., & Nairn, J. A. (2000). Fracture mechanics analysis of coating/substrate systems: Part I: Analysis of tensile and bending experiments. *Engineering Fracture Mechanics*, *65*(5), 573– 593. https://doi.org/10.1016/S0013-7944(99)00141-1

Kojima, A., Teshima, K., Shirai, Y., & Miyasaka, T. (2009). *Organometal Halide Perovskites as Visible-Light Sensitizers for Photovoltaic*. 6050–6051.

Lee, G., Kim, M., Choi, Y. W., Ahn, N., Jang, J., Yoon, J., Kim, S. M., Lee, J.-G., Kang, D., Jung,

H. S., & Choi, M. (2019). Ultra-flexible perovskite solar cells with crumpling durability: toward a wearable power source. *Energy & Environmental Science*, *12*(10), 3182–3191. https://doi.org/10.1039/C9EE01944H

Li, N., Tao, S., Chen, Y., Niu, X., Onwudinanti, C. K., Hu, C., Qiu, Z., Xu, Z., Zheng, G., Wang, L., Zhang, Y., Li, L., Liu, H., Lun, Y., Hong, J., Wang, X., Liu, Y., Xie, H., Gao, Y., … Zhou, H. (2019). Cation and anion immobilization through chemical bonding enhancement with fluorides for stable halide perovskite solar cells. *Nature Energy*, *4*(5), 408–415. https://doi.org/10.1038/S41560-019-0382-6

Li, X., Zhang, W., Wang, Y. C., Zhang, W., Wang, H. Q., & Fang, J. (2018). In-situ cross-linking strategy for efficient and operationally stable methylammoniun lead iodide solar cells. *Nature Communications*, *9*(1). https://doi.org/10.1038/S41467-018-06204-2

Li, Yang, Tao, J., Wang, Q., Zhao, Y., Sun, Y., Li, P., Lv, J., Qin, Y., Wang, W., Zeng, Q., & Liang, J. (2021). Microfluidics-based quantum dot color conversion layers for full-color micro-LED display. *Applied Physics Letters*, *118*(17), 173501. https://doi.org/10.1063/5.0047854

Li, Yaowen, Meng, L., Yang, Y. (Michael), Xu, G., Hong, Z., Chen, Q., You, J., Li, G., Yang, Y., & Li, Y. (2016). High-efficiency robust perovskite solar cells on ultrathin flexible substrates. *Nature Communications 2016 7:1*, *7*(1), 1–10. https://doi.org/10.1038/ncomms10214

Lin, Q., Armin, A., Chandra, R., Nagiri, R., Burn, P. L., & Meredith, P. (2014). Electro-optics of perovskite solar cells. *Nature Photonics*, *9*(2), 106–112. https://doi.org/10.1038/nphoton.2014.284

Liu, X., Guo, X., Lv, Y., Hu, Y., Lin, J., Fan, Y., Zhang, N., & Liu, X. (2018). Enhanced

Performance and Flexibility of Perovskite Solar Cells Based on Microstructured Multilayer Transparent Electrodes. *ACS Applied Materials and Interfaces*, *10*(21), 18141–18148. https://doi.org/10.1021/ACSAMI.8B03557/SUPPL_FILE/AM8B03557_SI_001.PDF

Liu, Y., Sun, J., Yang, Z., Yang, D., Ren, X., Xu, H., Yang, Z., & Liu, S. F. (2016). 20-mm-Large Single-Crystalline Formamidinium-Perovskite Wafer for Mass Production of Integrated Photodetectors. *Advanced Optical Materials*, *4*(11), 1829–1837. https://doi.org/10.1002/ADOM.201600327

Liu, Y., Yang, Z., Cui, D., Ren, X., Sun, J., Liu, X., Zhang, J., Wei, Q., Fan, H., Yu, F., Zhang, X., Zhao, C., & Liu, S. (2015). Two-Inch-Sized Perovskite CH3NH3PbX3 (X = Cl, Br, I) Crystals: Growth and Characterization. *Advanced Materials*, *27*(35), 5176–5183. https://doi.org/10.1002/ADMA.201502597

Liu, Y., Zhang, Y., Yang, Z., Yang, D., Ren, X., Pang, L., & Liu, S. F. (2016). Thinness- and Shape-Controlled Growth for Ultrathin Single-Crystalline Perovskite Wafers for Mass Production of Superior Photoelectronic Devices. *Advanced Materials (Deerfield Beach, Fla.)*, *28*(41), 9204–9209. https://doi.org/10.1002/ADMA.201601995

Ma, C., Liu, Y.-F., Liu, Y.-F., Gao, X.-M., Bi, Y.-G., Zhang, X.-L., Yin, D., Feng, J., Sun, H.-B., Sun, H.-B., & Sun, H.-B. (2020). Enhanced efficiency of organic light-emitting devices by using a directly imprinted nanopillared ultrathin metallic electrode. *Optics Letters, Vol. 45, Issue 17, Pp. 4879-4882*, *45*(17), 4879–4882. https://doi.org/10.1364/OL.402754

McMeekin, D. P., Sadoughi, G., Rehman, W., Eperon, G. E., Saliba, M., Hörantner, M. T., Haghighirad, A., Sakai, N., Korte, L., Rech, B., Johnston, M. B., Herz, L. M., & Snaith, H. J. (2016). A mixed-cation lead mixed-halide perovskite absorber for tandem solar cells. *Science*

(New York, N.Y.), *351*(6269), 151–155. https://doi.org/10.1126/SCIENCE.AAD5845

Nie, W., Tsai, H., Asadpour, R., Blancon, J. C., Neukirch, A. J., Gupta, G., Crochet, J. J., Chhowalla, M., Tretiak, S., Alam, M. A., Wang, H. L., & Mohite, A. D. (2015). High-efficiency solution-processed perovskite solar cells with millimeter-scale grains. *Science*, *347*(6221), 522–525.

Oyewole, O., Oyewole, D., Oyelade, O., Adeniji, S., Koech, R., Asare, J., Agyei-Tuffour, B., & Soboyejo, W. (2020). Failure of Stretchable Organic Solar Cells under Monotonic and Cyclic Loading. *Macromolecular Materials and Engineering*, *305*(11), 2000369. https://doi.org/10.1002/MAME.202000369

Park, S. Il, Ahn, J. H., Feng, X., Wang, S., Huang, Y., & Rogers, J. A. (2008). Theoretical and Experimental Studies of Bending of Inorganic Electronic Materials on Plastic Substrates. *Advanced Functional Materials*, *18*(18), 2673–2684. https://doi.org/10.1002/ADFM.200800306

Park, S. Il, Le, A. P., Wu, J., Huang, Y., Li, X., & Rogers, J. A. (2010). Light emission characteristics and mechanics of foldable inorganic light-emitting diodes. *Advanced Materials (Deerfield Beach, Fla.)*, *22*(28), 3062–3066. https://doi.org/10.1002/ADMA.201000591

Park, S. Il, Xiong, Y., Kim, R. H., Elvikis, P., Meitl, M., Kim, D. H., Wu, J., Yoon, J., Chang-Jae, Y., Liu, Z., Huang, Y., Hwang, K. C., Ferreira, P., Xiuling, L., Choquette, K., & Rogers, J. A. (2009). Printed assemblies of inorganic light-emitting diodes for deformable and semitransparent displays. *Science*, *325*(5943), 977–981. https://doi.org/10.1126/science.1175690

Prasanna, R., Gold-Parker, A., Leijtens, T., Conings, B., Babayigit, A., Boyen, H. G., Toney, M. F., & McGehee, M. D. (2017). Band Gap Tuning via Lattice Contraction and Octahedral Tilting in Perovskite Materials for Photovoltaics. *Journal of the American Chemical Society*, *139*(32), 11117–11124. https://doi.org/10.1021/JACS.7B04981/SUPPL_FILE/JA7B04981_SI_001.PDF

Qiu, L., Deng, J., Lu, X., Yang, Z., & Peng, H. (2014). Integrating Perovskite Solar Cells into a Flexible Fiber. *Angewandte Chemie International Edition*, *53*(39), 10425–10428. https://doi.org/10.1002/ANIE.201404973

Ren, X., & Jung, H. S. (2018). Recent Progress in Flexible Perovskite Solar Cell Development. *Journal of the Korean Ceramic Society*, *55*(4), 325–336. https://doi.org/10.4191/KCERS.2018.55.4.09

Saliba, M., Matsui, T., Domanski, K., Seo, J. Y., Ummadisingu, A., Zakeeruddin, S. M., Correa-Baena, J. P., Tress, W. R., Abate, A., Hagfeldt, A., & Grätzel, M. (2016). Incorporation of rubidium cations into perovskite solar cells improves photovoltaic performance. *Science*, *354*(6309), 206–209. https://doi.org/10.1126/SCIENCE.AAH5557/SUPPL_FILE/SALIBA.SM.PDF

Saliba, M., Matsui, T., Seo, J. Y., Domanski, K., Correa-Baena, J. P., Nazeeruddin, M. K., Zakeeruddin, S. M., Tress, W., Abate, A., Hagfeldt, A., & Grätzel, M. (2016). Cesium-containing triple cation perovskite solar cells: improved stability, reproducibility, and high efficiency. *Energy & Environmental Science*, *9*(6), 1989–1997. https://doi.org/10.1039/C5EE03874J

Sun, C., Pan, F., Bin, H., Zhang, J., Xue, L., Qiu, B., Wei, Z., Zhang, Z. G., & Li, Y. (2018). A

low cost and high-performance polymer donor material for polymer solar cells. *Nature Communications 2018 9:1*, *9*(1), 1–10. https://doi.org/10.1038/s41467-018-03207-x

Suo, Z., Ma, E. Y., Gleskova, H., & Wagner, S. (1999). Mechanics of rollable and foldable film-on-foil electronics. *Applied Physics Letters*, *74*(8), 1177. https://doi.org/10.1063/1.123478

Wehrenfennig, C., Eperon, G. E., Johnston, M. B., Snaith, H. J., Herz, L. M., Wehrenfennig, C., Eperon, G. E., Johnston, M. B., Snaith, H. J., & Herz, L. M. (2014). High Charge Carrier Mobilities and Lifetimes in Organolead Trihalide Perovskites. *Adv. Mater*, *26*, 1584–1589. https://doi.org/10.1002/adma.201305172

Wehrenfennig, C., Liu, M., Snaith, H. J., Johnston, M. B., & Herz, L. M. (2014). Charge carrier recombination channels in the low-temperature phase of organic-inorganic lead halide perovskite thin films. *APL Materials*, *2*(8). https://doi.org/10.1063/1.4891595

Yang, D., Yang, R., Ren, X., Zhu, X., Yang, Z., Li, C., & Liu, S. F. (2016). Hysteresis-Suppressed High-Efficiency Flexible Perovskite Solar Cells Using Solid-State Ionic-Liquids for Effective Electron Transport. *Advanced Materials*, *28*(26), 5206–5213. https://doi.org/10.1002/ADMA.201600446

Yang, D., Yang, R., Wang, K., Wu, C., Zhu, X., Feng, J., Ren, X., Fang, G., Priya, S., & Liu, S. (Frank). (2018). High efficiency planar-type perovskite solar cells with negligible hysteresis using EDTA-complexed SnO2. *Nature Communications 2018 9:1*, *9*(1), 1–11. https://doi.org/10.1038/s41467-018-05760-x

Yang, D., Yang, Z., Qin, W., Zhang, Y., Liu, S., & Li, C. (2015). Alternating precursor layer deposition for highly stable perovskite films towards efficient solar cells using vacuum deposition. *Journal of Materials Chemistry A*, *3*(18), 9401–9405.

https://doi.org/10.1039/C5TA01824B

Yang, D., Zhou, X., Yang, R., Yang, Z., Yu, W., Wang, X., Li, C., Liu, S., & Chang, R. P. H. (2016). Surface optimization to eliminate hysteresis for record efficiency planar perovskite solar cells. *Energy & Environmental Science*, *9*(10), 3071–3078. https://doi.org/10.1039/C6EE02139E

Yu, Z. G. (2016). Rashba Effect and Carrier Mobility in Hybrid Organic-Inorganic Perovskites. *Journal of Physical Chemistry Letters*, *7*(16), 3078–3083. https://doi.org/10.1021/ACS.JPCLETT.6B01404/SUPPL_FILE/JZ6B01404_SI_001.PDF

Zhou, H., Chen, Q., Li, G., Luo, S., Song, T. B., Duan, H. S., Hong, Z., You, J., Liu, Y., & Yang, Y. (2014). Interface engineering of highly efficient perovskite solar cells. *Science*, *345*(6196), 542–546. https://doi.org/10.1126/SCIENCE.1254050

Zhu, X., Yang, D., Yang, R., Yang, B., Yang, Z., Ren, X., Zhang, J., Niu, J., Feng, J., & Liu, S. (2017). Superior stability for perovskite solar cells with 20% efficiency using vacuum co-evaporation. *Nanoscale*, *9*(34), 12316–12323. https://doi.org/10.1039/C7NR04501H

Zuo, L., Dong, S., De Marco, N., Hsieh, Y. T., Bae, S. H., Sun, P., & Yang, Y. (2016). Morphology Evolution of High Efficiency Perovskite Solar Cells via Vapor Induced Intermediate Phases. *Journal of the American Chemical Society*, *138*(48), 15710–15716. https://doi.org/10.1021/JACS.6B09656/SUPPL_FILE/JA6B09656_SI_001.PDF

Chapter 6

CONCLUSIONS AND FUTURE WORK

6.1. Conclusions

This Thesis has presented a combined experimental, computational, and analytical approach to study the effects of pressure, a combination of experiments and theory to study the effects of temperature in the processing of perovskite solar cells to enhance the structural and optoelectronic properties, and performance of organic and hybrid solar cells. The Thesis also explored the failure mechanisms of flexible perovskite solar cells under monotonic and cyclic bending using a combined experimental and computational approach. The key issues discussed in this thesis include: the effects of pressure on photoconversion efficiencies of perovskite solar cells, the effects of annealing temperatures on the mechanical properties of layers in FAI-rich perovskite solar cells and the effects of PEO on the failure mechanisms of flexible perovskite solar cells under monotonic and cyclic bending. The results and the salient conclusion of each of the key issues are summarized below:

1. The effects of pressure on photoconversion efficiencies of perovskite solar cells (PSCs) was studied using a combined experimental and analytical/computational approach. The results show that the application of pressure results in improved interlayer surface contact, the compaction of mesoporous TiO_2 layers, and the infiltration of the mesoporous layers with perovskite for pressure up to 7MPa which also improved photoconversion efficiencies. However, at higher pressures ($p >$ 7 MPa), the damage due to sink-in of the perovskite layers into the adjacent mesoporous layers results in reductions in the photoconversion efficiencies of perovskite solar cells. The implications of the above results are significant for the design of pressure-assisted process such as lamination,

cold welding, and rolling/roll-to-roll processing can be used to fabricated perovskite solar cells with improved performance characteristics (photoconversion efficiencies, fill factors, short circuit currents and open circuit voltages. However, the applied pressures should be ~ 7 MPa or less, to ensure that the applied pressures do not induce layer damage and the excessive sink-in of perovskite layer (between layers). Hence, the combined effects of interlayer contact, mesoporous layer compaction and infiltration and the potential for layer damage at higher pressures must be considered in the optimized design of pressure-assisted processes for the fabrication of perovskite solar cells.

2. A combination of experiments and theory was used to study the effects of annealing temperature on the mechanical properties of hybrid organic-inorganic perovskite (HOIPs).

We have shown that the temperature at which perovskite film is annealed affects the mechanical properties of the devices fabricated. The size dependence of hardness is due to the increase in the density of GNDs with decreasing indentation size. The indentation size effects are characterized between the micron- and nano-scales by a bi-linear SGP framework with source-limited and established dislocation substructures. The measured microstructural length scales decrease with increasing annealing temperature to 130 ^{o}C, after which it began to increase, causing films annealed beyond 130 ^{o}C to have reduced strengths because the larger microstructural length scales correspond to larger dislocation spacings and weaker dislocation interactions. Perovskite solar devices annealed at temperatures above 130 ^{o}C have poor performance. We have shown that perovskite solar cell devices annealed at 130 ^{o}C exhibit optimal performance and attractive combinations of mechanical properties.

3. We report an effective additive technique developed to control the perovskite morphology on flexible substrates for FPSCs. The mechanical robustness of inverted flexible PSCs was increased by introducing a small amount of novel additive polymer, polyoxyethylene (PEO) to the double-cation perovskite precursor, to promote the grain size and passivate the defects of the film.

Experiments, analytic and computational models were used to gain insights into the failure mechanisms in layered materials relevant to flexible perovskite solar cells. The results showed that the morphology and crystallinity of the perovskite was improved by incorporating optimal content of PEO. The PSCs with 10% PEO exhibit remarkable mechanical robustness and PCE after many bending cycles at the least radius of 3.5 mm. This work provides a strategy to improve the PCE and mechanical robustness of flexible PSCs for the design of portable and wearable electronics.

6.2. Suggestions for Future Work

6.2.1. Stretchable Perovskite Solar Cells

The deformation and cracking behavior of thin films and layers relevant to stretchable perovskite solar cells under monotonic and cyclic loading need to be studied to be able to develop mechanically robust flexible/stretchable perovskite solar cells.

6.2.2. Micro-Wrinkling and Delamination-Induced Buckling of Stretchable Perovskite Solar Cells

Portable power sources, such as robotic systems, wearable electronics, consumer electronics, remote power, and automobiles undergo deformation in their domain of application. Therefore, the evidence of wrinkling and buckling failure modes due to temperature effects and cyclic loading should be characterized for different configurations of the devices.

6.2.3. Adhesion in Stretchable/Flexible Organic-Inorganic Perovskite Solar Cells

The wrinkles and buckles formed by unloading of pre-stretched perovskite layers should be characterized using atomic force microscopy and scanning electron microscopy. The critical stresses required for wrinkling and buckling should be analyzed using analytical models. And the possible interfacial cracking that can occur along with film buckling should also be studied using finite element simulations of the interfacial crack growth. This study will enable the application of micro-wrinkles and micro-buckles in power sources of wearable electronics.